

UTTAC-75, 2006

# **UTTAC**

## **ANNUAL REPORT 2005**

TANDEM ACCELERATOR COMPLEX  
Research Facility Center for Science and Technology  
University of Tsukuba

<http://www.tac.tsukuba.ac.jp/>

# UTTAC

## ANNUAL REPORT 2005

April 1, 2005 – March 31, 2006

UTTAC-75 2006

---

Executive Editors: Yasuo Nagashima

Editors: Yoshihiro Yamato, Kimikazu Sasa, Tetsuro Komatsubara

---

*Cover photo:* Cherry blossom in front of UTTAC.

---

UTTAC is a series of issues, which include annual reports of Tandem Accelerator Complex, Research Facility Center for Science and Technology, University of Tsukuba.

The issues may also include irregular reports written by English.

Copyright © 2006 by Tandem Accelerator Complex, Research Facility Center for Science and Technology, University of Tsukuba and individual contributors.

All reports are written on authors' responsibility and thus the editors are not liable for the contents of the report.

---

Tandem Accelerator Complex, Research Facility Center for Science and Technology,  
University of Tsukuba

Tennodai 1-1-1, Tsukuba, Ibaraki 305-8577, Japan

<http://www.tac.tsukuba.ac.jp/>

[annual@tac.tsukuba.ac.jp](mailto:annual@tac.tsukuba.ac.jp)

## PREFACE

During the academic year 2005, from April 2005 to March 2006, efforts have been paid to the stable operation both of 12UD Pelletron and 1MV Tandetron as well as to the construction of new beam lines. The new line for a  $\mu$ -beam PIXE analysis has been constructed at the Tandetron accelerator and a new X-ray Si detector has been installed in the PIXE line. After finishing an acceptance test, the new line is going to throw into research works as a new service.

In the field of element analysis, the  $^{36}\text{Cl}$  accelerator mass spectrometry,  $^{36}\text{Cl}$ -AMS, has been intensively used as a tool for studying of the A-bomb peak in the groundwater sampled at Germany. The  $^{36}\text{Cl}$ -AMS made a contribution to assess the nuclear waste clearance level. A hydrogen analysis with p-p elastic-recoil coincidence method has been applied to the geological research. The sensitivities and stabilities of both the AMS and the Hydrogen analysis have been improved and they are going to be applied to the many research fields. The Eu concentration in Eu-doped GaN has been estimated by Rutherford backscattering spectroscopy, RBS.

In the field of nuclear physics, the study of proton total cross section of  $p+^{12}\text{C}$  and the search for the resonant state in  $p+\text{Si}$  at the (p,n) threshold energy were precisely performed. A  $^{118}\text{Sn}(d,p)$  reaction was intensively studied to look for deuteron Coulomb stripping.

In atomic and condensed matter physics, the evolution of resonant coherent excitation of hydrogen-like ions has been observed with a  $180^\circ$  electron spectroscopy. Nano-scale and high aspect ratio patterns were created on the  $\text{SiO}_2$  and  $\text{TiO}_2$  substances with accelerated fast heavy ions.

Without accelerated beams, Mössbauer studies on  $\gamma\text{-Fe}_2\text{O}_3$  thin foils and a study of 3d transition-metal oxide system were pursued.

The agreement for the exchange of students has been established with the Department of Nuclear Physics of the China Institute of Atomic Energy. According to this agreement, UTTAC is taking on a Chinese graduate student for one year.

UTTAC organized one workshop and two symposiums. The workshop entitled "Mass measurements in the isochronous rare-RI ring and nucleon-synthesis" has been held with 26 attendants and 12 contribution talks. The first East Asian AMS Symposium (EAAMS-1), and the 8th Japanese AMS Symposium (JAMS-8), have been organized by the Tsukuba AMS group and successfully concluded. It was attended by 120 peoples from 5 countries. The contributions to the symposiums, both technical and applied, clearly demonstrated that AMS has evolved into a versatile tool to study our world, especially our East Asia, via long-lived radio-nuclides. The Proceedings of both Symposiums contain 44 papers covering a large fraction of the contributions presented at the symposium



Yasuo Nagashima

Director



# CONTENTS

<b>1. ACCELERATOR AND EXPERIMENTAL FACILITIES</b>	
1.1 Accelerator operation 2005 . . . . .	1
1.2 Micro PIXE system for trace element analysis in single fluid inclusions of mineral samples	4
<b>2. NUCLEAR PHYSICS</b>	
2.1 CDCC compound process and Oppenheimer Phillips effect . . . . .	7
2.2 Resonant state search in p+Si system around (p,n) threshold . . . . .	10
2.3 $^{118}\text{Sn}(d,p)$ reaction in search for Coulomb stripping of deuteron III . . . . .	12
2.4 Proton total cross section on $^{12}\text{C}$ near (p,n) threshold energy (2) . . . . .	14
2.5 Measurement of alignment correlation term in $^{20}\text{F}$ $\beta$ decay . . . . .	16
2.6 Development of a high-efficiency method for $\alpha$ resonant scattering with the thick target method . . . . .	18
2.7 Measurement of timing resolution for plastic scintillation counters in vacuum . . . . .	20
2.8 Particle identification using pulse shape analysis . . . . .	22
<b>3. ATOMIC AND SOLID STATE PHYSICS, AND CLUSTER SCIENCE</b>	
3.1 Evolution of resonant coherent excitation of hydrogen-like fast ions . . . . .	25
3.2 Vicinage effect in the yield of convoy electrons under irradiation of fast carbon cluster ions	27
3.3 Möesbauer study on $\gamma\text{-Fe}_2\text{O}_3$ thin films . . . . .	29
3.4 The science of 3d transition-metal oxide system (2005-2006) . . . . .	31
3.5 Oxidations of cobalt clusters . . . . .	33
3.6 Estimation of Eu concentration in Eu-doped GaN by RBS measurements . . . . .	34
<b>4. ION BEAM ANALYSIS AND APPLICATION</b>	
4.1 Status of Tsukuba AMS system . . . . .	35
4.2 $^{129}\text{I}$ -AMS by the Tsukuba AMS system . . . . .	37
4.3 Test measurement of $^{36}\text{Cl}$ concentration in an ice core retrieved from the Dome Fuji station in Antarctica . . . . .	38
4.4 Bomb-produced $^{36}\text{Cl}$ in the Oderbruch aquifer, Germany: A preliminary result . . . . .	39
4.5 Improvements in sample preparation for $^{36}\text{Cl}$ -AMS . . . . .	40
4.6 Estimation of thermal neutron fluences in the concrete of verious accelerator facilities by $^{35}\text{Cl}$ AMS . . . . .	42
4.7 Low Z element analysis of the Cr target deposited by HIVIPP method using a 1.8 MeV $\text{He}^+$ beam of Tandetoron accelerator . . . . .	44
4.8 Imaging of iodinated contrast medium using proton-induced quasi-monochromatic X-ray emission . . . . .	47
4.9 Nanoscale and high aspect ratio patters on $\text{SiO}_2$ and $\text{TiO}_2$ created with fast heavy ions . . . . .	49
4.10 New detection system of ERCS hydrogen analysis . . . . .	51

<b>5. TECHNICAL REPORT</b>	
5.1 New data acquisition system using CC/7700 . . . . .	55
<b>6. RELATED TOPICS</b>	
6.1 Highly-concentrative immobilization of an enzyme only on a small sensitive area and its effect on sensor performance . . . . .	57
<b>7. LIST OF PUBLICATIONS</b>	
7.1 Journals . . . . .	59
7.2 International conferences . . . . .	62
<b>8. THESES</b>	<b>64</b>
<b>9. SEMINARS</b>	<b>64</b>
<b>10. SYMPOSIA</b>	<b>65</b>
<b>11. LIST OF PERSONEL</b>	<b>68</b>

**1.**

**ACCELERATOR AND EXPERIMENTAL FACILITIES**



## 1.1 Accelerator operation 2005

K. Sasa, S. Ishii, T. Takahashi, Y. Yamato, H. Kimura, H. Oshima, Y. Tajima, T. Komatsubara and Y. Nagashima.

### The 12UD Pelletron tandem accelerator

The total operating time and the experimental beam time were 2345.8 and 1963.1 hours, respectively. The operating time was about 131.2 % relative to that in 2004. Fig.1 shows the accelerator operation hours per month. The beam time histogram with respect to the terminal voltage is shown in Fig.2. Fig.3 represents percentage operation time of the three ion sources and ion species. Fig.4 shows the percentage of experimental beam time of the running research fields by the 12UD Pelletron tandem accelerator.

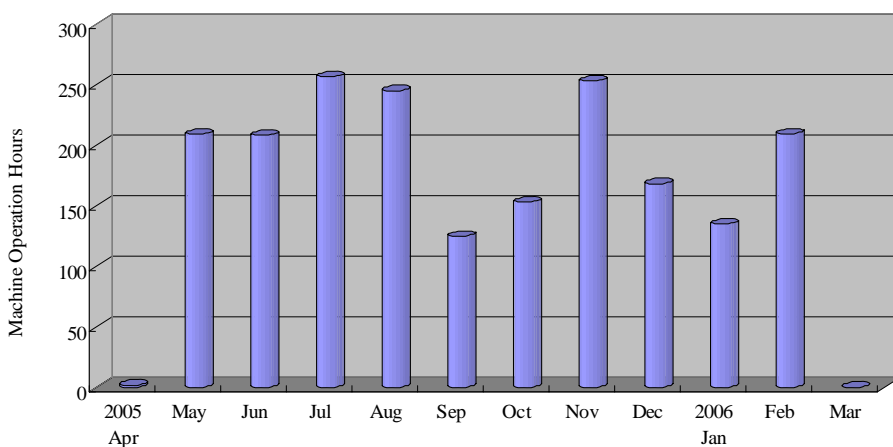


Fig.1. Accelerator operation hours per month for the fiscal year 2005.

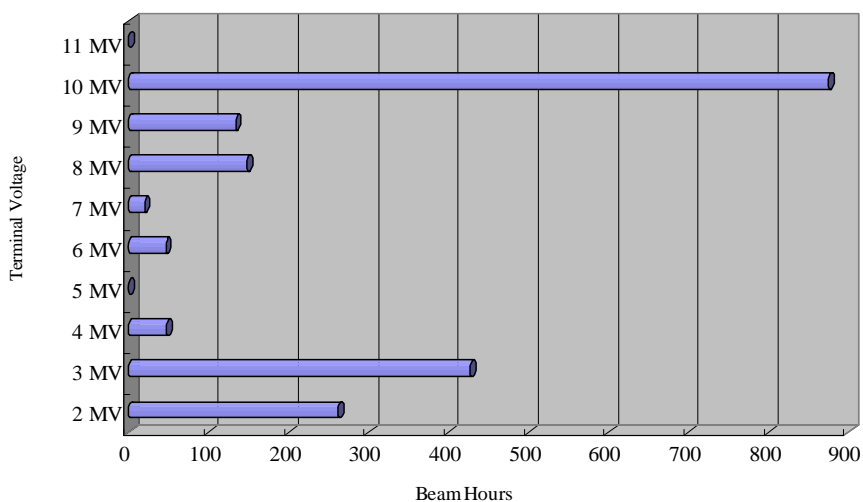


Fig.2. Beam time histogram as a function of the terminal voltage.

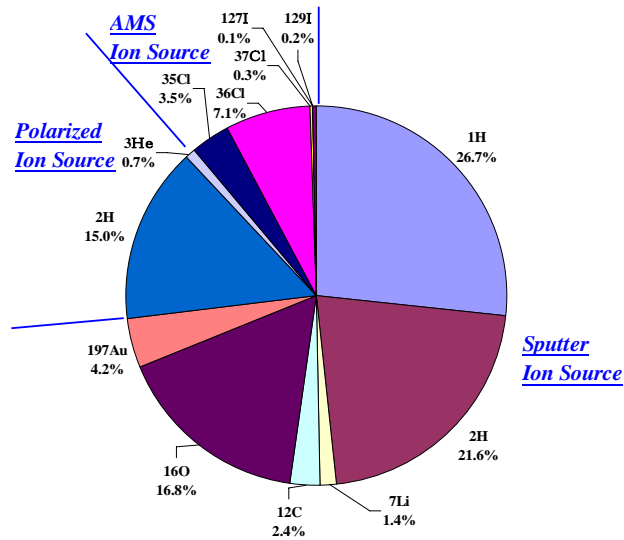


Fig.3. Percentage operation hours of the three ion sources and ion species.

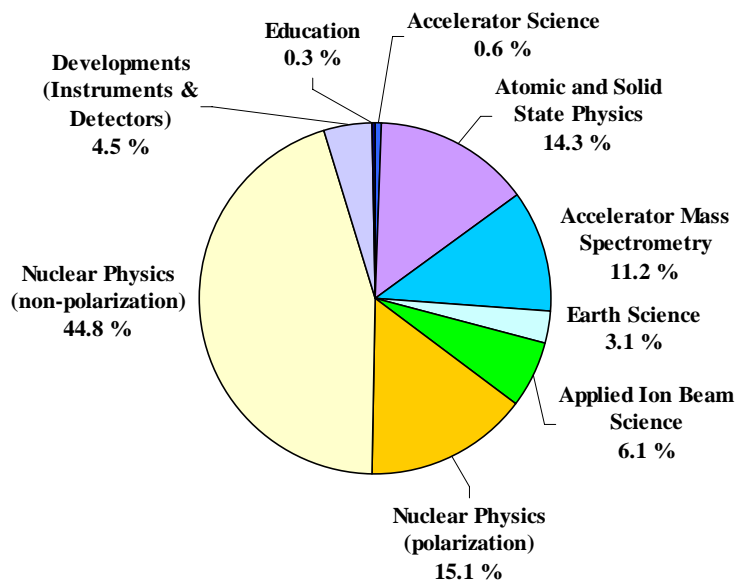


Fig.4. Percentage experimental beam time of the research fields.

The 12UD Pelletron tandem accelerator had been operated at the terminal voltage lower than 10.5 MV by reason of the instability of the terminal voltage for the fiscal year 2005. The operation time at terminal voltage of 10 MV records the largest beam time. The accelerated time of Au ion increased in the field of the material irradiation. In addition,  $^3\text{He}$  ion beam was used for the development of a thin solid state detector.

The scheduled maintenance in the spring 2006 was started on March 2 and finished on May 8. All corona points were replaced along the column and the accelerating tube. We also changed stripper foils of

the A and B foil units with new one. Especially, stripper foils with a diameter of 12 and 16 mm were set on the B foil unit for AMS study. These diameters were larger than the normal foil diameter. A beam profile monitor was set on the focal position for the accelerating tube in the accelerator tank. The beam profile monitor will be used for adjusting the beam transport to the accelerating tube.

### The 1MV Tandetron accelerator

The total operating time of the 1MV Tandetron accelerator was 348.7 hours for the fiscal year 2005. This time was about 45.1 % relative to that in 2004. Fig. 5 shows the percentage of accelerated ions with the 1MV Tandetron accelerator. Fig.6 shows the percentage of experimental beam time of the running research fields. The main research field of the 1MV Tandetron accelerator was the cluster physics. The 1MV Tandetron accelerator was also used for trace-element analysis with particle induced X-ray emission (PIXE), Rutherford backscattering spectroscopy (RBS) and the education in the field of ion beam study.

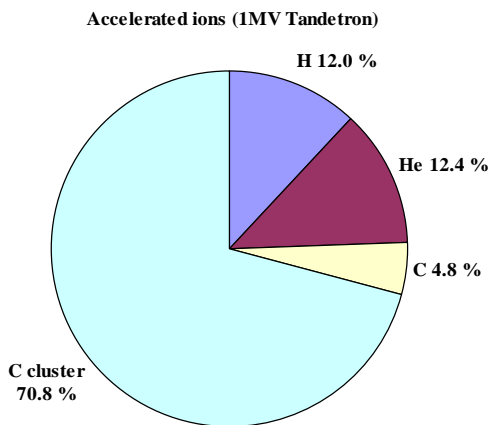


Fig.5. Percentage of accelerated ions with the 1MV Tandetron accelerator.

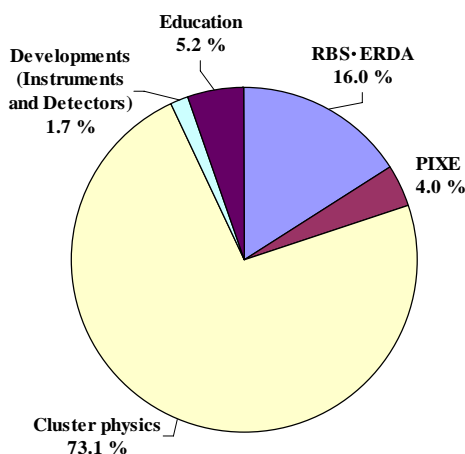


Fig.6. Percentage of experimental beam time of the running research fields with the 1MV Tandetron accelerator.

## 1.2 Micro PIXE system for trace element analysis in single fluid inclusions of mineral samples.

K. Sasa, S. Ishii, Y. Yamato and M. Kurosawa

A proton microprobe system has been developed at the 30° beam line (A-course) on the 1 MV Tandatron accelerator. This system was designed to investigate the PIXE analysis in single fluid inclusions of mineral samples. Fig.1 shows a schematic layout of the micro PIXE system. It consists of a beam defining slit (first slit), a collimating slit (second slit), a steering magnet, a quadrupole doublet lens (ISM-10DQ-05, IDX Inc.), a new Si detector (Sirius series, 50 mm<sup>2</sup> det. area, e2v scientific instruments Ltd.) and a sample chamber. The sample chamber was already reported by Ref. [1] in detail. The employed microscope (Wild M420 photomicroscope, Leica Ltd.) has a 102 mm working distance and 6 magnifications. The sample image can be observed on a monitor using a CCD camera and enlarged the magnification up to 360 by this unit. The angle of observation was 180° with respect to the incident beam using a 45° mirror with a beam through hole. The sample stage can be moved to 90 mm and 25 mm along the horizontal and vertical axes with a minimum step of 1 μm respectively. The quadrupole doublet lens was designed to form a microfocused beam. The performance of the quadrupole doublet lens is also presented in Fig.1. The incident beam angle is normal to the sample surface. The Si detector is located at 135° relative to the beam direction and has a normal resolution of 143 eV at 5.9 keV. The length of the beam line is limited within 3.5 m by the target room. The working distance is 300 mm. The beam demagnification factors are calculated to 11.2 and 3.1 in the horizontal and vertical directions respectively.

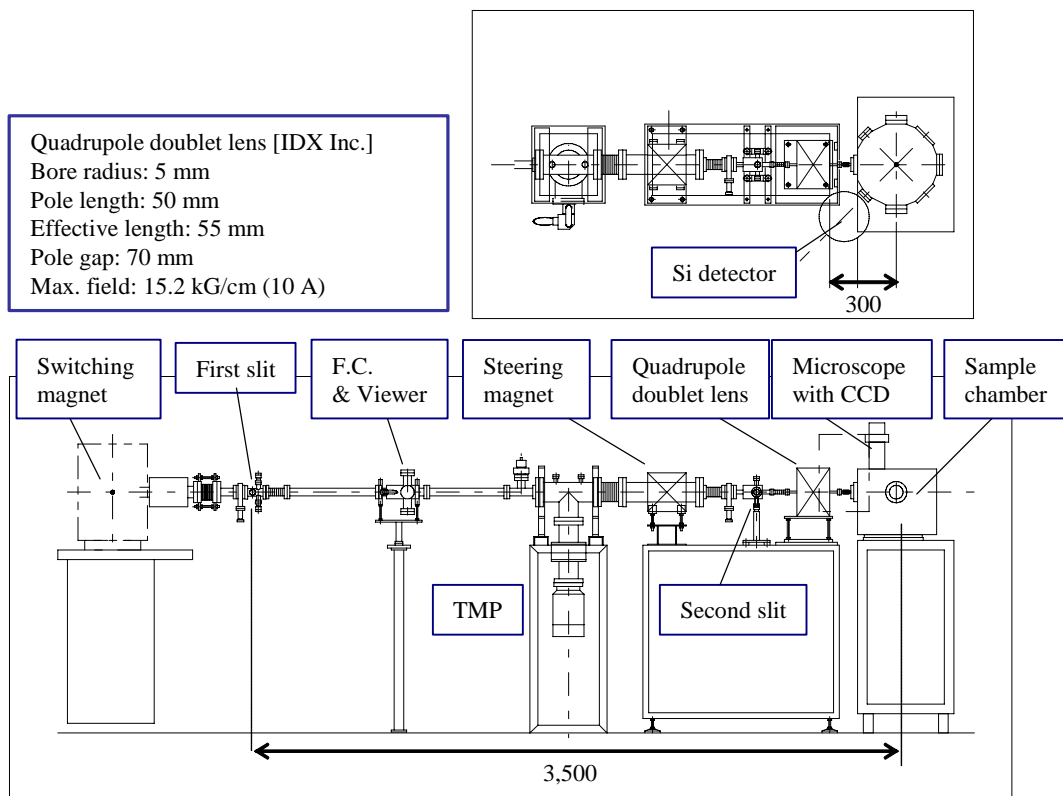


Fig.1 Schematic layout of the micro PIXE system on the 1 MV Tandatron accelerator.

The size of a beam spot on the sample is important for investigations of the micro PIXE analysis in single fluid inclusions. A preliminary test was performed with a 1.82 MeV proton beam. We observed scintillation light emitted from a ZnS plate attached to the sample stage by irradiating the focused proton beam. The beam spot size of 20  $\mu\text{m}$  was obtained with a beam current of 1 nA. The minimum beam spot size of less than 10  $\mu\text{m}$  was achieved with a beam current of 0.1 nA by adjusting the width of the first slit. Fig. 2 shows a photograph of the focused proton beam spot on the ZnS plate.

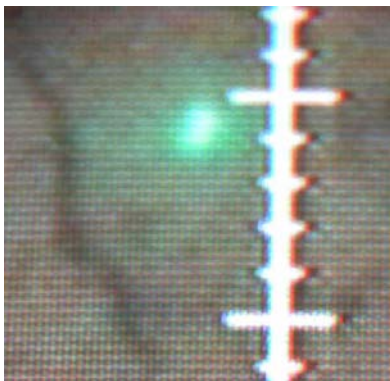


Fig. 2 A focused beam spot of the 1.82 MeV proton beam on the ZnS plate. The beam current is 0.1 nA. The minimum scale on a ruler is estimated to 12  $\mu\text{m}$ .

### References

- [1] M. Kurosawa et al., Nucl. Instr. and Meth. B142 (1998) 599.



**2.**

## **NUCLEAR PHYSICS**



## 2.1 CDCC compound process and Oppenheimer Phillips effect

Y. Aoki, M. Iijima, T. Ishikawa, and N. Okumura<sup>1</sup>

In 1935 Lawrence et al.,[1] reported energy dependence of (d,p) reactions on Na, Al, Si and Cu nuclei below  $E_d = 3.6$  MeV. They irradiated stacked targets by their ‘magnetic resonance accelerator’, whose laboratory slang was ‘cyclotron’, and measured the residual activities. They noticed, contrary to the energy dependence of proton and  $\alpha$  particles induced reaction cross sections, that of (d,p) reaction was weaker than the prediction of Gamow theory.

Oppenheimer and Phillips [2] solved this puzzle as follows. They wrote the initial wave function as

$$\Psi_i = u(x, X) \phi(X),$$

where  $u(x, X)$  is the wave function for the relative coordinate  $x$ , when the center of mass  $X$  is fixed, and  $\phi(X)$  is the wave function for the center of mass. They separated the  $u(x, X)$  and  $\phi(X)$ ,

$$\left\{ \hbar^2/M\Delta_x + \mathcal{E}(X) - V_0(x) - V_N(x, X) \right\} u = 0$$

and

$$\left\{ \hbar^2/4M\Delta_X + W - I - \mathcal{E}(X) \right\} \phi = 0.$$

In this expression  $V_0$  is the potential between neutron and proton, and  $V_N$  is the nuclear potential.  $W$  and  $I$  are total and deuteron binding energies. They took  $V_N$  the Coulomb repulsion of the proton in the deuteron and target, and neglected the specifically nuclear forces, i.e., ‘deuteron’ internal motion is distorted by Coulomb potential. They evaluated  $u(x, X)$  at  $x = 2X$  by using WKB approximation.  $x = 2X$  means  $r_n = 0$  and the neutron is located in the target nucleus. Their energy dependence of (d,p) reaction is presented as Fig. 2-5 of ref. [1].

Coulomb distortion should introduce negative parity component into the ‘deuteron’ internal wave function. N. Austern [3] studied this Coulomb polarization effect of the deuteron by using three body model and evaluated the cross section ratio of  $\sigma(d,p)/\sigma(d,n)$ . He approximated

$$T(d, p) = T^{(0)}(d, p) + T^{(1)}(d, p),$$

where

$$T^{(0)} = \langle \chi_p^{(-)}(\mathbf{k}_p, \mathbf{r}_p) \Psi_n(\mathbf{r}_n) | V(r) | \Psi_d(\mathbf{r}) F_0(\mathbf{R}) \rangle$$

is the usual DWBA amplitude and  $T^{(1)}$  stands for the deuteron breakup effect. He expected the (d,p) cross section,  $\sigma(d,p)$ , is enhanced than that of (d,n) reaction if Coulomb polarization is really meaningful. He concluded the enhancement is less than 5 % and the Oppenheimer-Phillips effect is hidden by the Coulomb effect under the proton bound state wave functions.

As is seen in the above expression, (d,p) reaction matrix element include  $V(r)\Psi_n(\mathbf{r}_n)$ , the product of short range p-n interaction and neutron bound state wave function. This expression is not the one that

---

<sup>1</sup>Nagano National College of Technology

Oppenheimer and Phillips suggested. We used the different approach from the Oppenheimer and Phillips effect.

Let us write CDCC wave function as,

$$\Psi_M(\mathbf{R}, \mathbf{r}) = \sum_{JL_0} G(L_0JM) \sum_c \Psi_{JM}^c(\mathbf{R}, \mathbf{r})$$

where

$$\Psi_{JM}^c(\mathbf{R}, \mathbf{r}) = \frac{1}{R} \sum_L [i^L Y_L(\hat{\mathbf{R}}) \phi_{I_c}^c(\mathbf{r})]_{JM} \Phi_{LL_0}^{cJ}(R)$$

have definite angular momentum and the expansion coefficient is given as

$$G(L_0JM) = \frac{\sqrt{4\pi(2L_0+1)} e^{i\sigma_{L_0}}}{K_0} (L_0 0 I_0 M | JM).$$

Vectors  $\mathbf{R}$  and  $\mathbf{r}$  define center of mass and relative coordinates of the ‘deuteron’. Wave function for the CM motion  $\Phi(R)$  satisfies the following equation,

$$-\frac{\hbar^2}{2\mu_R} \left( \frac{d^2}{dR^2} - \frac{L(L+1)}{R^2} \right) \Phi_{LL_0}^{cJ} + \sum_{c'L'} V_{cc'} \Phi_{L'L_0}^{c'J} = E_c \Phi_{LL_0}^{cJ},$$

and

$$V_{cc'} = \langle [i^L Y_L(\hat{\mathbf{R}}) \phi_{I_c}^c(\mathbf{r})]_{JM} | V | [i^{L'} Y_{L'}(\hat{\mathbf{R}}) \phi_{I_{c'}}^{c'}(\mathbf{r})]_{JM} \rangle$$

are matrix elements of sum of proton and neutron optical potentials,  $V = V_p(\mathbf{r}) + V_n(\mathbf{r}_n)$ , sandwiched by ‘deuteron’ internal wave functions.  $\Phi(R)$ ’s satisfy the usual incoming wave boundary condition, from which following relation is derived for S matrix elements of break up channels, c.

$$|S_{LL_0}^{cJ}|^2 = \frac{4\mu_R}{iK_0\hbar^2} \sum_{c'L'} \int dR \left\{ \Phi_{LL_0}^{cJ} V_{cc'} \Phi_{L'L_0}^{c'J} - \Phi_{LL_0}^{cJ} V_{c'c}^* \Phi_{L'L_0}^{c'J} \right\}$$

This expression tells how the outgoing wave in channel c is generated. Included among the sums on  $c'$ , we notice the absorption effect from diagonal element,  $\langle c | \Im \{V_{cc}\} | c \rangle$ . We can identify that the reduction of  $|S_{LL_0}^{cJ}|^2$  from neutron imaginary potential as the neutron absorption probability after incident deuteron is dissociated. It should be noticed that the matrix element  $V_{cc}$  has very long range.

Numerical calculation of CDCC compound process is made for  $^{118}\text{Sn}(d,p)$  reaction. ‘Deuteron’ internal states of  $^3S_1 - ^3D_1$ ,  $^3D_{2,3}$ ,  $^3P_{0,1}$ ,  $^3P_2 - ^3F_2$  are taken into account. Except for the  $^3D_3$  state, Reid [4] soft core potential are used. Energetically open ‘break-up’ channels are taken into account and discretized as six separate wave number bins. Global nucleon optical potential of CH89 [5] was used. Three cases of deuteron break up is considered, 1) pure Coulomb break up, 2) pure nuclear break up, and 3) both nuclear and Coulomb interactions are responsible for the deuteron break up. In case 1), nucleon optical potential is completely neglected.

Figures below shows the absorption cross section for each momentum bin. Plotted in the figure is the following quantity,

$$\Delta_k \sum_c \frac{4\pi}{(2I_0+1)K_0^3} \sum_{JL_0L} \sum_c' \int dR |\Phi_{LL_0}^{cJ}|^2 \text{Im} \left( \frac{2\mu_R}{\hbar^2} W_{cc}^n \right),$$

where  $\Delta_k$  is the wave number bin width of the p-n relative motion and the sum on c runs over same ‘deuteron’ energy.

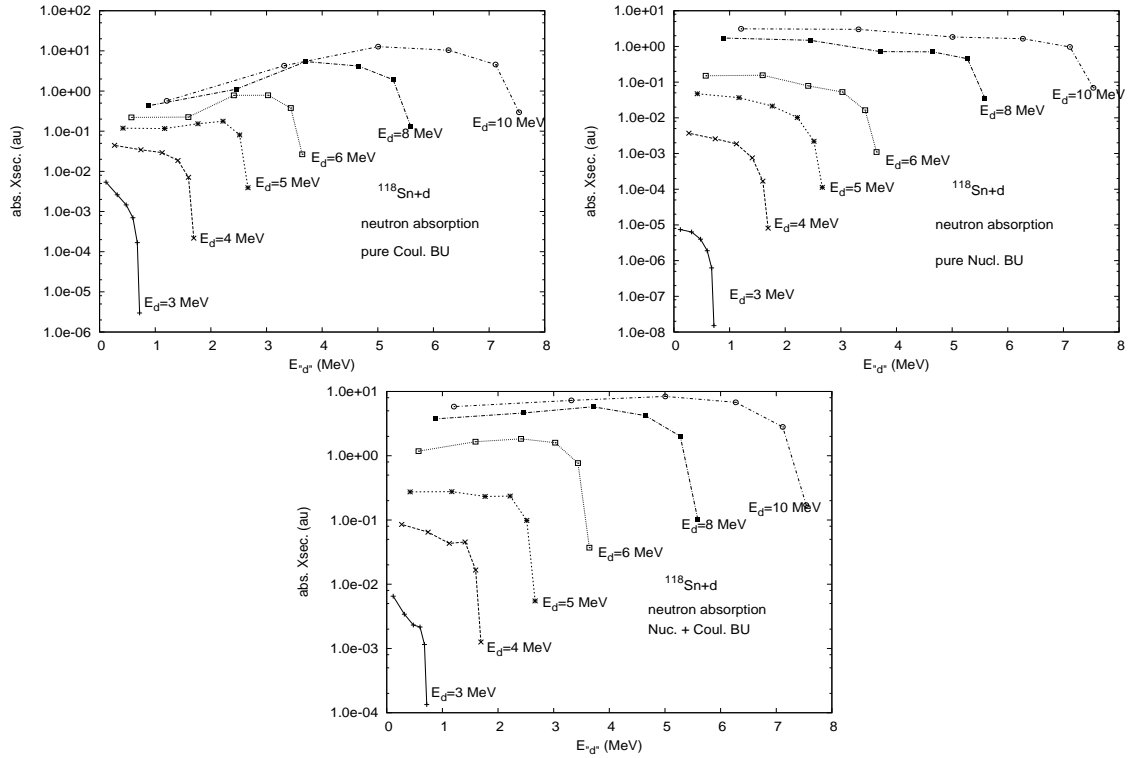


Fig. 1. Energy dependence of neutron absorption. Abscissa is the ‘deuteron’ energy, while ordinate is the absorption cross section. Upper left panel shows the case for pure Coulomb break up, upper right panel for pure nuclear break up and the lower panel for the case including nuclear and Coulomb break up.

‘Deuteron’ energy of the rightmost point of each curve is lower from the incident energy by about 2.2 MeV, the deuteron binding energy.

Coulomb break up dominates for the lower energy case.

As was predicted by Oppenheimer and Phillips, energy dependence of (d,p) cross section is moderated by including Coulomb break up process.

## References

- [1] E. O. Lawrence, E. McMillan and R. L. Thornton, Phys. Rev. **48**493(1935)
- [2] J. R. Oppenheimer and M. Phillips, Phys. Rev. **48**500(1935)
- [3] N. Austern, Phys. Rev. **C43**771(1991)
- [4] R. V. Reid, Jr, Ann. Phys **50**411(1968)
- [5] R. L. Warner, Phys. Rep. **201**59(1991)

## 2.2 Resonant state search in p+Si system around (p,n) threshold

Y. Aoki, M. Iijima, T. Ishikawa, N. Okumura<sup>1</sup>, and Y. Tagishi<sup>2</sup>

We reported the (p,n) threshold effect of total reaction cross section in p+Si system [1]. To confirm this effect in proton elastic scattering, new experiment was designed. It consists of measuring elastic scattering cross section at backward angles with relatively thick target and a magnetic spectrograph. Protons incident on the thick target will lose some kinetic energy before it is elastically scattered by the target nucleus. Energy and relative intensity of the elastically scattered protons are dependent on what depth they are scattered. Elastically scattered protons will lose their kinetic energy before they really leave the target. This energy loss after elastic scattering favors to improve the energy resolution of the resonance effect. Following is a numerical example. Protons of 15.9 MeV are allowed to hit Si target of 100  $\mu\text{m}$  thick, which is located perpendicular to the beam direction. Energy range of the elastic scattering is thus limited from 15.33 to 15.90 MeV. Energy range of protons elastically scattered to  $135^\circ$  is expanded to 12.61 to 14.05 MeV. Energy range is thus amplified by about a factor of 2.5.

Feasibility test experiment was made successfully. Natural Si of 50, 100 and 150  $\mu\text{m}$  targets are hit by protons of  $E_p = 15$  to 16.2 MeV. Elastically scattered protons are momentum analyzed by an Enge type magnetic spectrograph (ESP90) and detected by using a single wire position sensitive proportional counter. Position information is extracted by a charge ratio method. Linearity of the focal position and the momentum is confirmed by using elastic scattering of protons from thin gold target. Quadratic term is found to be negligible small.

Sample momentum spectrum is given in fig. 1, where three proton spectrum of different target thickness are superposed. Elastic scattering builds up from about 830 ch. 50  $\mu\text{m}$  spectrum spans about 600 to 830 ch, those of 100 and 150  $\mu\text{m}$  about 400 to 830 channels. Energy dependence of elastic scattering has many dips and valleys. Inelastically scattered protons span from 380 to lower channels. Triangular peak in 100  $\mu\text{m}$  data around 370 channel is due to the fall of elastic and building up of inelastic yields.

Linear portion of the high energy edge, which correspond to elastic and inelastic scattering at the front surface of the target, are used to calibrate the proton energy and are indicated by two vertical lines. Center of mass energy of these lines correspond to 14.41 and 15.35 MeV, i.e., 800 keV energy range of CM system is mapped onto 400 channels.

1) Definite change of elastic cross section near (p,n) threshold ( at around 700-725 channel) cannot be seen. 2) Resonance states of less than 100 keV widths can easily be identified by this thick target method.

## References

[1] N. Okumura, Y. Aoki, T. Joh, K. Hirota and K.S. Itoh, Nucl. Inst. Meth. **A487**565(2002)

---

<sup>1</sup>Nagano National College of Technology

<sup>2</sup>RIKEN

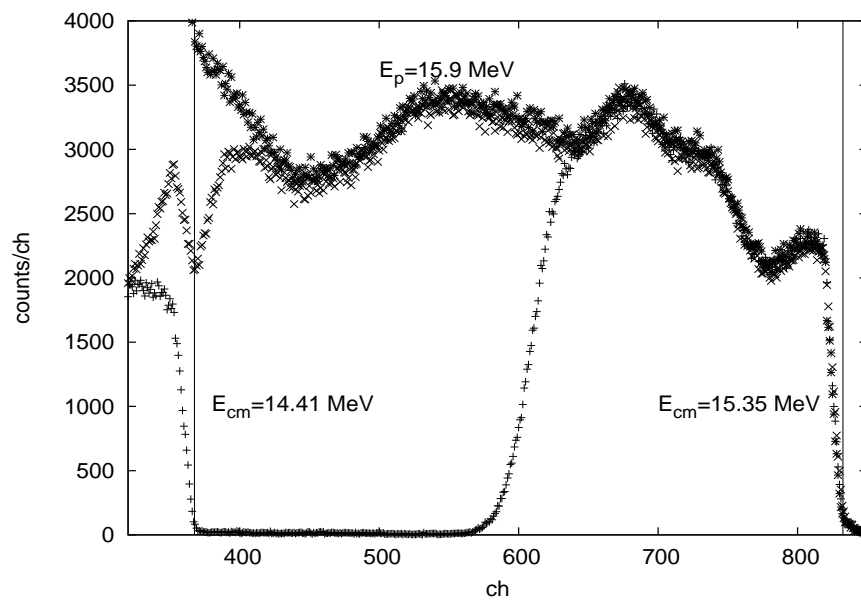


Fig. 1. Proton momentum spectrum elastically scattered from 50, 100 and 150  $\mu\text{m}$  thick target. Incident energy is 15.9 MeV and scattering angle is  $145^\circ$ . Target is placed  $45^\circ$  to the incident beam direction. For more details, see the text.

## 2.3 $^{118}\text{Sn}(d,p)$ reaction in search for Coulomb stripping of deuteron. III

M.Iijima, Y.Aoki, Y.Ito, T.Ishikawa, S.Igarashi and Y.Tagishi

Coulomb break-up of deuterons was proposed in 1930s[1] and a CDCC calculation suggested its enhancement below Coulomb barrier with targets of large atomic numbers [2].

From December 2005 to February 2006 we measured differential cross section ( $\sigma(\theta)$ ) of  $^{118}\text{Sn}(d,p_0)$  reaction at  $E_{lab} = 5.5 \sim 8\text{MeV}$ . The experiments were performed using 12 UD Pelletron at UTTAC. Targets were  $^{118}\text{Sn}$  with enrichment of 98.70 % and thickness around  $500 \sim 800\mu\text{g}/\text{cm}^2$ . Momenta of deuterons and protons were analyzed by magnetic spectrograph ESP90. We used Single Wired Proportional Chamber of 30cm long as a focal plane detector. Solid angle was approximately 3.3 msr. Beam current on target was around 100nA.

Fig.1 is a typical spectrum of protons taken by the SWPC, whereas deuterons were stopped by a  $200\mu\text{m}$  absorber in front of it. The shaded area consists presumably of three peaks, which are from  $^{118}\text{Sn}(d,p)$  reactions leading to the ground state, the first and the second excited states of  $^{119}\text{Sn}$ . Fig.2 shows the sum of differential cross sections leading to these three unresolved states. A further analysis is now in progress.

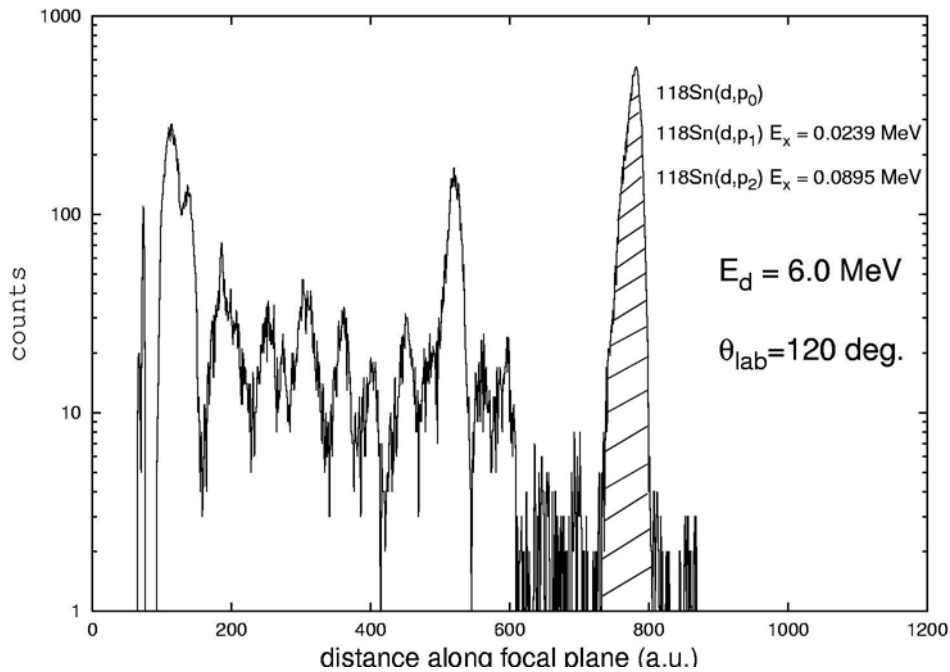


Fig. 1. A typical spectrum of protons

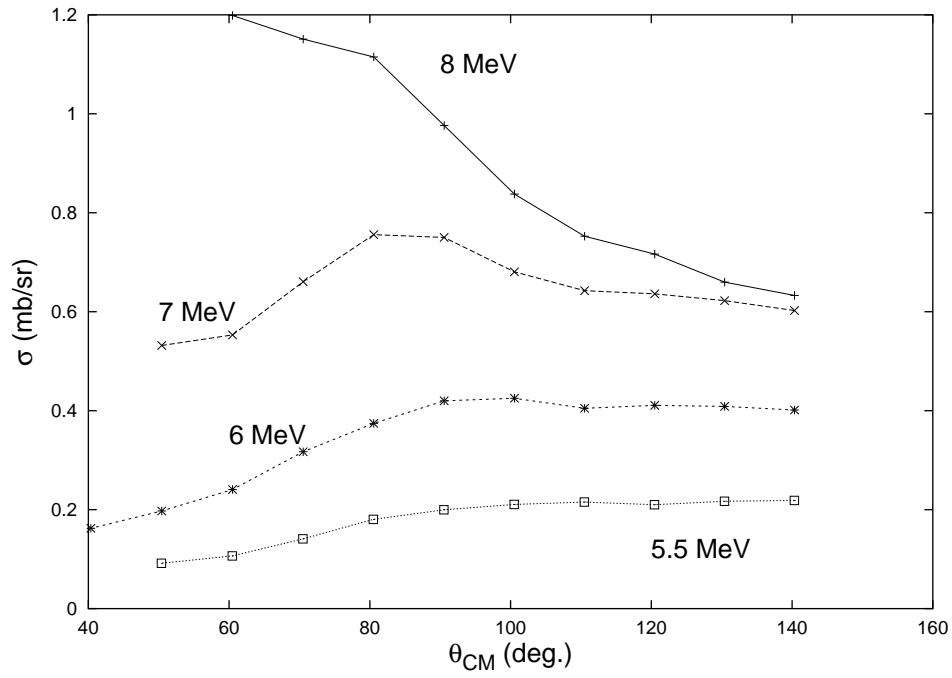


Fig. 2. Sum of the experimental differential cross sections of  $^{118}\text{Sn}(d,p_0)$ ,  $^{118}\text{Sn}(d,p_1)$  and  $^{118}\text{Sn}(d,p_2)$  reactions

## References

- [1] J.R.Oppenheimer and M.Phillips, Phys. Rev. **48**,500(1935)
- [2] Y.Aoki, N.Okumura, H.Ishiguro, UTTAC ANNUAL REPORT, 22(2002)

## 2.4 Proton total cross section on $^{12}\text{C}$ near (p,n) threshold energy (2)

T.Ishikawa, M.Iijima, Y.Ito and Y.Aoki

A resonance like behavior was predicted in nucleon-nucleus effective potential [1] at nucleon transfer reaction threshold energy. A dip in the energy dependence of total reaction cross section  $\sigma_R$  near (p,n) threshold energy was reported in  $^{28}\text{Si}+p$  system [2] to be presumed as the behavior. In order to investigate this threshold effect, another system of  $^{12}\text{C}+p$  reaction was studied. Details of our confirming experiment are given in [2] and [3].

In our previous report [4], the dip in the  $\sigma_R$  for the  $^{12}\text{C}+p$  system was not clearly observed because of the large experimental error which was 10 % as a relative error. In order to reduce the error of the measurement two improvements were performed.

For the first improvement, a beam diffuser of  $7\mu\text{m}$  thick tantalum foil was located at upstream of the switching magnet, as shown in Fig.1. Beam is strongly focused and tightly limited at the image slit (horizontal width of 0.1mm) of the analyzing magnet. Therefore, tiny drift of accelerating voltage or a magnet field of upstream device may strongly affect beam path and intensity in the downstream. The Diffuser broadens beam width in real and momentum space, and reduces the sensitivities by the upper beam properties.

In our timing logic of the counting system is studied. The second improvement is IO counter that is a pair of proportional counters, spontaneous discharges occur by some reasons. Pulse height of the discharge is sometimes larger than the true proton pulse. Spurious counts appeared in the higher energy portion of the proton spectrum. So we use discriminator in window mode, and inspected the discharge contribution. But this idea did not contribute to decrease the relative error. Using envelope mode of digital oscilloscope, we checked and modified timing of other signals.

In 2005, we have experiments on June and July. The data of this year, together with the past ones, are presented in Fig.2. June data has the smallest error in our experiments, but the expected dip can not be seen. We used thinner target in July than in June ( $8.0\text{ mg/cm}^2$ ). Horizontal error of July data is not shown because we do not have the data of precise thickness. About July data, the measured error is larger than that of June data and magnitude of the  $\sigma_R$  is getting small in low energy region. Origin of this decline in energy dependence is not understood yet.

## References

- [1] N.K.Glendenning, Direct Nuclear Reactions(1983), Academic Press
- [2] N.Okumura *et al.*, Nucl. Inst. Meth. **A487**, 565(2002)
- [3] T.J.Gooding *et al.*, Nucl. Phys. **12**, 241(1959)
- [4] T.Ishikawa, Annual Report, University of Tsukuba, 2004
- [5] M.Q.Makino *et al.*, Nucl. Phys. **68**, 378(1965)

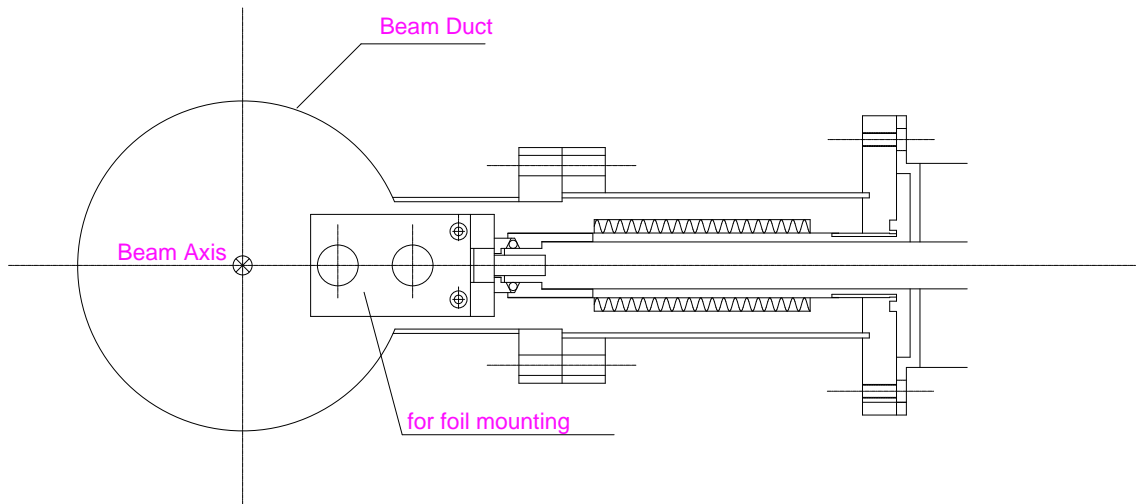


Fig. 1. Cross-sectional view of beam diffuser

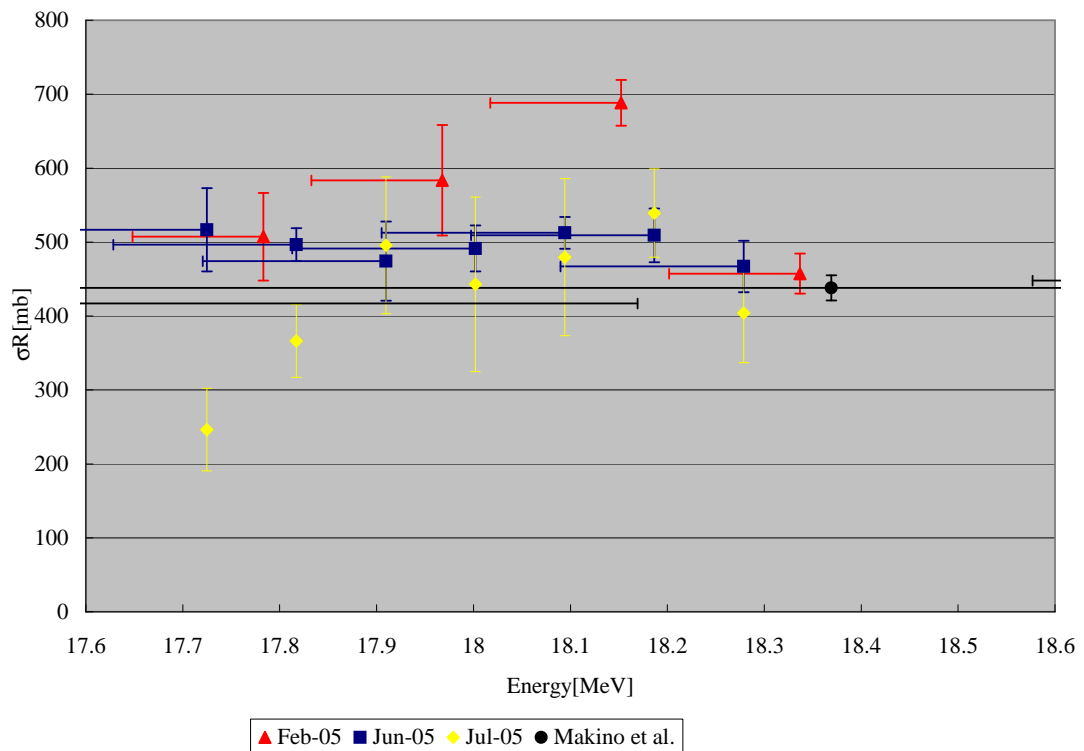


Fig. 2. Energy dependence of  $\sigma_R$  in  $^{12}\text{C}+\text{p}$  system ( $Q_{(p,n)}^{cm}=-18.12\text{MeV}$ ). Abscissa is the c.m. Energy. Black squares are the data of Makino *et al.*[5].

## 2.5 Measurement of alignment correlation term in $^{20}\text{F}$ $\beta$ decay

T.Nagatomo, A.Ozawa, Y.Tagishi<sup>1</sup>, K.Matsuta<sup>2</sup>, M.Mihara<sup>2</sup>, R.Matsumiya<sup>2</sup>, M.Yamaguchi<sup>1</sup>, T.Sumikama<sup>1</sup>, H.Ohta, T.Yasuno, Y.Hashizume, K.Minamisono<sup>3</sup>, M.Fukuda<sup>2</sup> and T.Minamisono<sup>4</sup>

The alignment correlation term in  $\beta$ -ray angular distribution is one of the good probes for the  $G$ -parity violating weak nucleon currents and the meson exchange effects inside the nucleus. The  $G$  transformation is defined as  $G \equiv C e^{i\pi T_y}$ , where  $C$  is the charge-conjugation operator and  $e^{i\pi T_y}$  is the charge-symmetry operator. For on-shell nucleons with initial and final momenta  $p_i$  and  $p_f$ , respectively, the weak nuclear axial vector current including the recoil effects, which are the operators composed of the  $\gamma$  matrices and  $q_\mu = p_f - p_i$ , is described as

$$\langle p_f | A_\mu | p_i \rangle = \bar{u}(p_f) \gamma_5 (f_A \gamma_\mu + f_T \sigma_{\mu\nu} q_\nu + i f_P q_\mu) u(p_i) \quad (1)$$

where  $u(p)$  is the proton or neutron wave function,  $f_A$ ,  $f_T$  and  $f_P$  are the main, induced tensor and pseudo-scalar term, respectively. Under the  $G$  transformation, the induced tensor term  $f_T$  has the opposite sign against the  $f_A$  and  $f_P$  terms, thus it causes the  $G$ -symmetry breaking. The angular distribution of the  $\beta$ -rays emitted from the purely aligned unstable nuclei is described as

$$W(\theta, E, \mathcal{A}) \propto 1 + \alpha(E) \mathcal{A} \frac{3 \cos^2 \theta - 1}{2} \quad (2)$$

where  $\theta$  is the  $\beta$ -ray emitting angle respect to the quantum axes,  $E$  is the total energy of the  $\beta$  ray,  $\mathcal{A}$  is the nuclear alignment and  $\alpha(E)$  is the alignment correlation coefficient. With the impulse approximation of the Hamiltonian density of the interaction of the nucleon current (Eq.1) with the lepton current, we can obtain the  $f_T$  from the difference between the linear term of the alignment coefficients  $\alpha^{(1)}$  of mirror nuclei  $^{20}\text{F}$  and  $^{20}\text{Na}$  in the mass number  $A = 20$  system as

$$\alpha^{(1)}(^{20}\text{F}; E) - \alpha^{(1)}(^{20}\text{Na}; E) = \left\{ -\frac{2}{3M} \left( \frac{b}{Ac} - \frac{d_{\parallel}}{Ac} + \sqrt{\frac{3}{14}} \frac{j_2}{Ac} \frac{\Delta E_0}{2MA} \right) \right\} E \quad (3)$$

where  $M$  is the nucleon mass,  $A$  is the mass number,  $\Delta E_0$  is the difference between the end-point energy of  $^{20}\text{F}$  and  $^{20}\text{Na}$ ,  $\frac{b}{Ac}$  is the weak magnetism and  $\frac{d_{\parallel}}{Ac} \cong \frac{g_{\parallel}}{g_A} = 2M \frac{f_T}{f_A}$ . In the present work, we have measured the alignment correlation term of  $^{20}\text{F}$  ( $I^\pi = 2^+$ ,  $T_{1/2} = 11\text{s}$ ) by observing  $\beta$ -rays emitted from the purely spin aligned nuclei by means of the  $\beta$ -NMR technique.

Experiment was performed at the University of Tsukuba Tandem Accelerator Complex (UTTAC). The 6 MeV polarized deuteron beam was employed to produced the polarized  $^{20}\text{F}$  nuclei through the polarization transfer  $^{19}\text{F}(\vec{d}, p)^{20}\vec{\text{F}}$  reaction by bombarding  $\text{MgF}_2$  single crystal plate. The typical beam current and beam polarization were 1 nA and  $\sim 80\%$ , respectively. The details of experimental procedures were shown in the previous work[1]. In the present work, the averaged polarization of  $^{20}\text{F}$  was  $\sim 8\%$  with the asymmetry parameter of  $-1/3$ , and the  $\beta$ -ray counting rate was typically 20kcps. Utilizing the combination of the depolarization (DEP) and the adiabatic fast passage method (AFP) on the four

<sup>1</sup>RIKEN, Wako, Saitama 351-0106

<sup>2</sup>Department of Physics, Osaka Univ., Toyonaka, Osaka 560-0043 Japan

<sup>3</sup>NSCL, Michigan State Univ., East Lansing, MI 48824-1321, USA

<sup>4</sup>Fukui Univ. of Technology, Fukui 910-8505 Japan

resonance frequencies, which was split by the hyperfine interaction with the electric field gradient in the  $\text{MgF}_2$  crystal. We could manipulate the spin ensemble and produce both the positive and negative alignment,  $\mathcal{A}_+$  and  $\mathcal{A}_-$ . Comparing the intensities of  $\beta$ -rays emitted from the state of  $\mathcal{A}_+$  and  $\mathcal{A}_-$ , the alignment correlation term was obtained.

We have to eliminate the background  $\beta$  rays from  $^{25}\text{Al}$  ( $T_{1/2} = 7.2\text{s}$ ,  $Q_{E.C.} = 4.3\text{MeV}$ ) and  $^{27}\text{Mg}$  ( $T_{1/2} = 9.5\text{m}$ ,  $Q_{\beta^-} = 2.6\text{MeV}$ ) that were produced through  $^{24}\text{Mg}$  (d,n) and  $^{26}\text{Mg}$  (d,p) reactions, respectively. Typical  $\beta$ -ray time spectrum was obtained as shown in Fig.1. The ratio of the production rate ( $P.R.$ ) of  $^{25}\text{Al}$  to that of  $^{20}\text{F}$  was obtained as  $\frac{P.R.(^{25}\text{Al})}{P.R.(^{20}\text{F})} = 0.165(4)$ . Typical energy spectrum was observed as shown in Fig.2. The  $\beta$ -ray-counter efficiency depends on the finite solid angle of the detector, and is affected by the  $\beta$ -ray scatterings and the magnetic fields of 0.25 Tesla. For reliable analysis, these effects are estimated for each energy with the Monte Carlo simulation code EGS4[2], and are considered in the fitting function for the energy spectrum. As shown in Fig.2, such a theoretical spectrum with the background components fixed to the obtained production rate, fits to the experimental data very well, to show that the background estimation is reliable within a few percent error for each energy. The alignment correlation term  $\alpha(E)$  was obtained as shown in Fig.3. In the figure, the  $\beta$ - $\gamma$  angular correlation term [3, 4], which is multiplied by  $-2/3$  to compare with the obtained  $\alpha(E)$ , and the theoretical prediction calculated with the impulse approximation including higher order term such as  $j_2$  and  $j_3$ [5] are also shown. To give the constraint of the existence of the  $f_T/f_A$ , the analyses on  $^{20}\text{Na}$  as well as on  $^{20}\text{F}$  are now in progress.

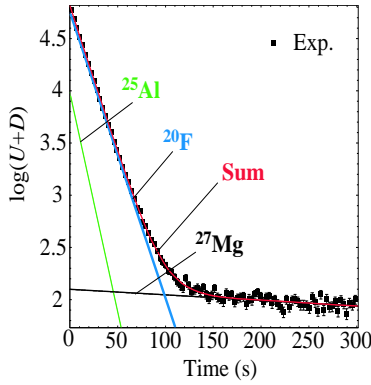


Fig. 1. Typical  $\beta$  ray time spectrum.

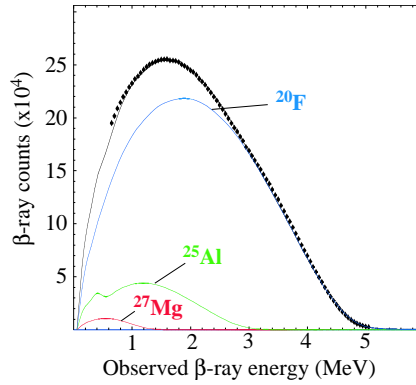


Fig. 2. Typical  $\beta$  ray energy spectrum.

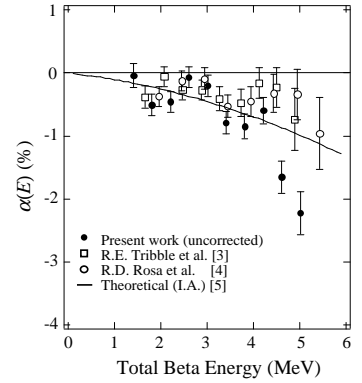


Fig. 3. uncorrected  $\alpha(E)$  of  $^{20}\text{F}$  with the  $\beta$ - $\gamma$  correlation term multiplied by  $-2/3$ .

## References

- [1] K.Matsuta et al., UTTAC Annual Report, **73**, 14(2005), Genshikaku Kenkyu **49**, (2005) 31.
- [2] H.Hirayama et al., "Lecture Notes of EGS4 Course at KEK", KEK Internal, **99-5**, (1999)
- [3] R.E. Tribble and D.P.May, Phys. Rev., **C18**, 2704(1978).
- [4] R.D.Rosa et al., Phys. Rev., **C37**, 2722(1988).
- [5] F.P.Calaprice et al., Phys. Rev., **C15**, 2187(1977).

## 2.6 Development of a high-efficiency method for $\alpha$ resonant scattering with the thick target method

H. Fujikawa<sup>1</sup>, S. Kubono<sup>1</sup>, A. Saito<sup>1</sup>, H. Yamaguchi<sup>1</sup>, G. Amadio<sup>1</sup>, J. J. He<sup>1</sup>, L. H. Khiem<sup>2</sup>, S. Nishimura<sup>3</sup>, H. Ohta, A. Ozawa, Y. Tagishi, Y. Wakabayashi<sup>4</sup>, M. Yamaguchi and T. Yasuno

We have been developing an experimental method to measure the  $\alpha$  resonant scattering and the  $(\alpha, p)$  reactions with the thick-target method [1] in inverse kinematics using a room-temperature helium gas target. This method enables us to study the  $\alpha$ -induced reactions of unstable nuclei which are only available as secondary beams. In order to establish the experimental method to measure the  $\alpha$  resonant scattering, we performed an experiment of  $\alpha+^{16}\text{O}$  elastic scattering at the University of Tsukuba Tandem Accelerator Center (UTTAC). Figure 1 shows a schematic view of the experimental setup. An  $^{16}\text{O}$  beam of 40 MeV was supplied by the 12UD Pelletron tandem accelerator. In the beam-monitoring section, the beam was collimated by a double-collimator system. A carbon foil was set after the collimators. A silicon detector was set at 12 degrees with respect to the beam direction in order to measure the beam current using the  $^{16}\text{O}+^{12}\text{C}$  elastic scattering. The setup for measuring the  $\alpha$  resonant scattering is shown in the target section in Fig. 1. Helium gas at room temperature was used as a target. The gas was confined by a Havar foil at the entrance of the target section. The pressure of helium gas was adjusted so as to stop the beam particles before the telescope in the gas. The energy of the  $^{16}\text{O}$  beam decreased down to 32.5 MeV after the Havar foil. A telescope consisting of two position sensitive silicon detectors (PSD1 and PSD2) and a pad silicon detector (SSD) was set on the rotatable table to cover a certain range of scattering angle inside the gas. The recoil  $\alpha$  particles were identified by the  $\Delta E$ - $E$  method.

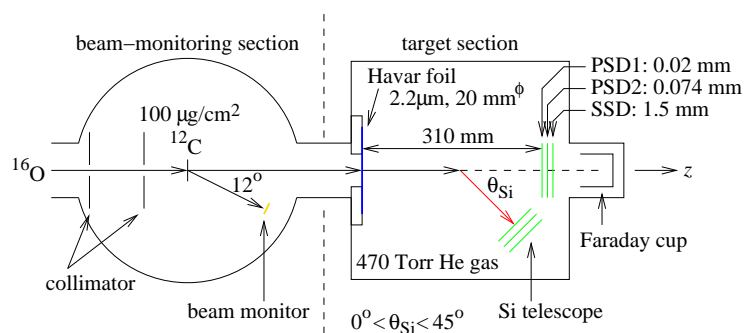


Fig. 1. Schematic view of the experimental setup.

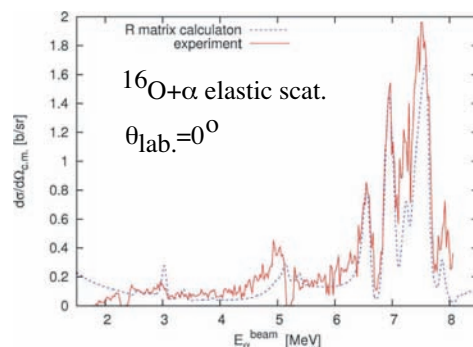


Fig. 2. The  $R$ -matrix fit to the 0 deg. data.

The  $R$ -matrix calculation was performed to the experimental data. Figure 2 shows an energy spectrum of  $\alpha$  particles measured by the strip at 0 degree. The red line shows the experimental data. The blue one corresponds to the  $R$ -matrix calculation including the experimental resolution. Several peaks were observed which correspond to known levels in  $^{20}\text{Ne}$  [3].

<sup>1</sup>Center for Nuclear Study, University of Tokyo

<sup>2</sup>Institute of Physics and Electronics, Vietnam

<sup>3</sup>RIKEN

<sup>4</sup>Department of Physics, Kyushu University

Figure 3 shows the correlation between the energy and the scattering angle of the recoil  $\alpha$  particles. The vertical axis is the energy of the recoil  $\alpha$  particles at the telescope, whereas the horizontal axis is the scattering angle in the center-of-mass system. The scattering angle was determined by taking the kinematics and the energy losses of the incident and the recoil particles into account. The dotted curves are the calculations which well reproduce the experimental data. Figure 4 shows an example of the angular distribution of the recoil  $\alpha$  particles for the 10.55 MeV  $4^+$  state in  $^{20}\text{Ne}$ . The data has a good agreement with  $|P_4(\cos\theta_\alpha^{\text{c.m.}})|^2$ .

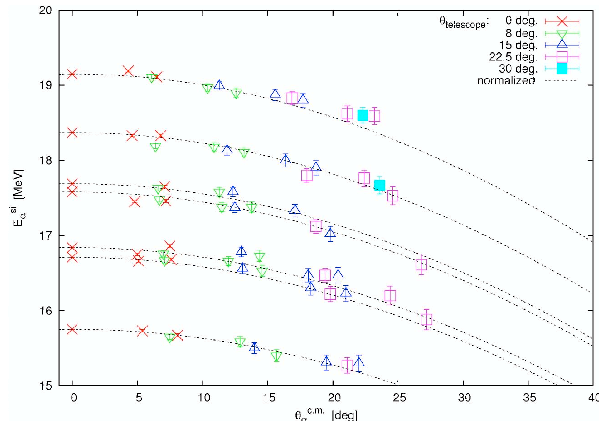


Fig. 3. Correlation between the energy and the scattering angle of the recoil  $\alpha$  particles.

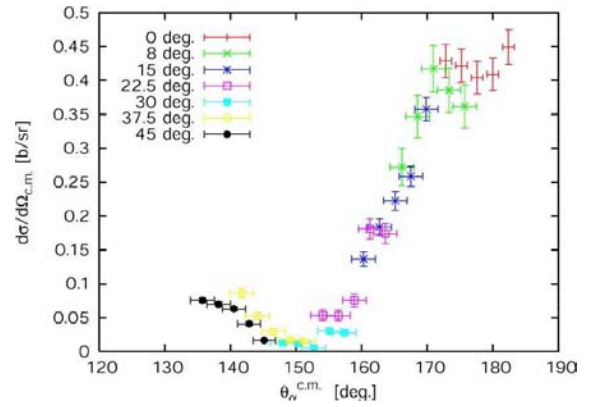


Fig. 4. Angular distribution of the 10.6 MeV  $4^+$  state in  $^{20}\text{Ne}$ .

In the present study, the experimental method for the  $\alpha$  resonant scattering was developed using the room-temperature helium gas target and the inverse kinematics. The  $R$ -matrix analysis of the data showed good agreements with the resonance parameters known for the excited states in  $^{20}\text{Ne}$ . This method will be applied to  $\alpha$  resonant scattering experiment using RI beams.

## References

- [1] S. Kubono, Nucl. Phys., **A693**, 221 (2001).
- [2] M. Notani et al., Nucl. Phys., **A738**, 411 (411).
- [3] D. R. Tilley et al., Nucl. Phys. **A636**, 249 (1998).

## 2.7 Measurement of timing resolution for plastic scintillation counters in vacuum

Y. Hashizume, A. Ozawa, T. Nagatomo<sup>1</sup>, and T. Yasuno

Measurement of time-of-flight (TOF) with good timing resolution is necessary for particle identification for radioactive isotope (RI) beam experiments. Plastic scintillation counters are widely used to measure TOF. In order to avoid energy losses of beam at vacuum windows, it is appropriate for detectors to be operated in vacuum. A commercial photomultiplier tube (PMT) assembly, Hamamatsu H6533, which has a good timing response, can not be operated in vacuum because of outgas [1].

We constructed new plastic scintillation counter assemblies to be operated in vacuum using PMT, Hamamatsu R4998. The plastic scintillator of BC408 with dimension of  $50 \times 50 \times 0.6 \text{ mm}^3$  was coupled to the PMT with a light guide. The measurement of intrinsic timing resolution of the counter was performed at 2E course (NASS chamber) in the 12UD tandem accelerator of UTTAC using 17MeV proton beam. Fig.1 shows the experimental set up. Two identical counters located inside the NASS chamber have been operated in vacuum around  $10^{-7}$  Torr for 7 hours without any change of vacuum condition or fluctuations of pulse shape from the counters. The beam intensity was typically 1nA. The proton beam was elastically scattered at  $1 \mu\text{m}$  Au foil. The counting rate of the elastically scattered ions can be changed by selecting the scattering angle. The signals from upstream and downstream counters were connected to the TDC start and stop inputs, respectively. A typical TOF spectrum is shown in Fig.2.

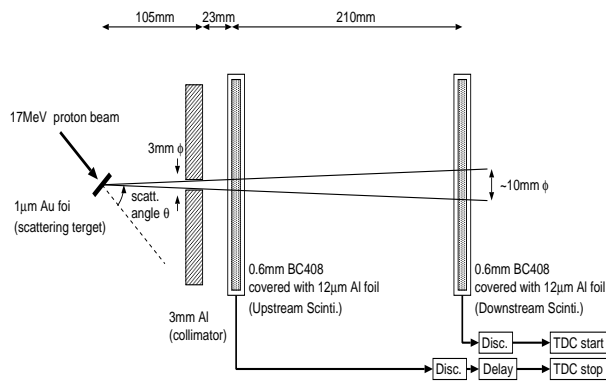


Fig. 1. The experimental set up.

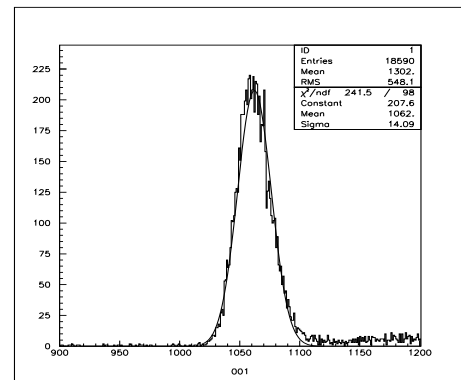


Fig. 2. A typical TOF spectrum between the upstream and downstream counter. The spectrum is fitted by a Gaussian shape.

<sup>1</sup>RIKEN (The Institute of Physical and Chemical Research), Wako, Saitama 351-0198, Japan

Intrinsic timing resolution  $\sigma_{int}$  can be estimated by  $\sigma_{TOF}$  obtained from the TOF spectra. If performance of the two counters is identical, the following equation is fulfilled;

$$\sigma_{TOF}^2 = \frac{1}{2}\sigma_{int}^2 \quad (1)$$

The typical  $\sigma_{int}$  was 130ps in sigma. High voltage (HV) and counting rate dependences of  $\sigma_{int}$  are shown in Fig.3 (a) and (b), respectively. Note that HV of downstream counter was fixed at -2000V in Fig.3 (a) and that HV of both upstream and downstream counters were fixed at -2400V in Fig.3 (b).

In the RI beam experiments,  $\sigma_{int}$  can become smaller since the atomic number of the beam is larger and more light output from the plastic scintillator is available. Thus we conclude that our counters can be used for particle identification of RI beam experiments.

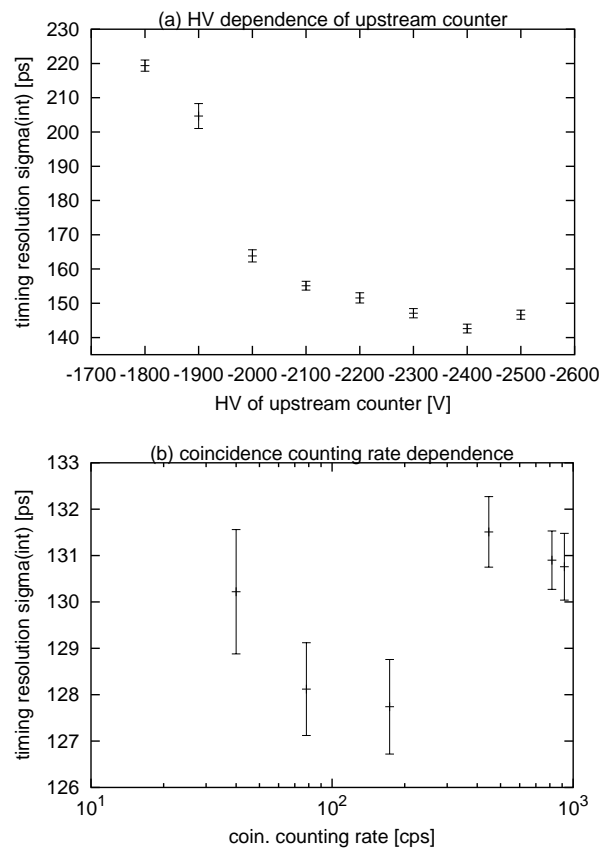


Fig. 3. HV (a) and counting rate (b) dependences of  $\sigma_{int}$ . HV of downstream counter was fixed at -2000V in (a). HV of upstream and downstream counters were fixed at -2400 in (b).

## References

- [1] R. Kanungo et al., RIKEN Accel. Prog. Rep. **35** (2002) 164

## 2.8 Particle identification using pulse shape analysis

M. Kurokawa<sup>1</sup>, H. Baba<sup>1</sup>, M. Yamaguchi<sup>1</sup>, S. Nishimura<sup>1</sup>, T. Fukuchi<sup>2</sup>, A. Ozawa, and H. Tagishi<sup>1</sup>

To identify charge and mass numbers of nuclei, pulse-shape discrimination of a signal from a Si detector was proposed more than 40 years ago. The technique is based on a monotonic increase of charge collection time with charge and mass number for nuclei with the same energy. The increase is associated with a longer distance between an electrode on the junction side and the position where an incident particle induces the ionization with the highest density. Since the idea was realized by Pausch *et al.*[?] for the first time, different analyzing methods of the pulse shapes have been examined for these ten years. In spite of these efforts, the discrimination in a low energy region is deteriorated because of an unexpected phenomenon, which is an opposite dependence of the charge collection time on the distance. The lower limit of 2.5 MeV has been reported for the discrimination between the proton and alpha particles.

To understand the reason and to improve the capabilities for the technique, beam test was performed at the TANDEM accelerator at the University of Tsukuba. Incident energy of a <sup>3</sup>He beam was 30 MeV, and the scattered particles by a Ag target were identified with the  $\Delta E$ - $E$  method consisting of two Si detectors. The  $E$  detector was mounted so that the ohmic side was irradiated and was biased as much voltage as required for total depletion. The junction side is divided into 4 strips. To record the pulse shape from a strip, the signal of the preamplifier was coded by a sampling ADC(SIS3301) with a resolution of 14 bit and 100 MSamples/s. The starting time of the recorded pulse shape is given by the  $\Delta E$  detector, which was over biased to obtain good timing information. For thus recorded pulse shape, the relation between the deposited energy in the  $E$  detector and the averaged rise time is shown in Fig. 1 for light charged particles. Here, the rise time is defined as the time when the magnitude of the pulse reaches 60% of its maximum height. The energy was obtained by the trapezoidal shaping. Larger error bars for particles with their atomic number of 2 are due to the lower statistics. As seen in the figure, the discrimination of the proton and alpha particle is possible down to an energy of 1 MeV. The more accurate determination of the starting time of signals will achieve the better performance of the particle identification.

## References

- [1] G. Pausch et al.: IEEE Trans. on Nucl. Sci. **43**, 1097 (1996).

---

<sup>1</sup>RIKEN

<sup>2</sup>Rikkyo Univ.

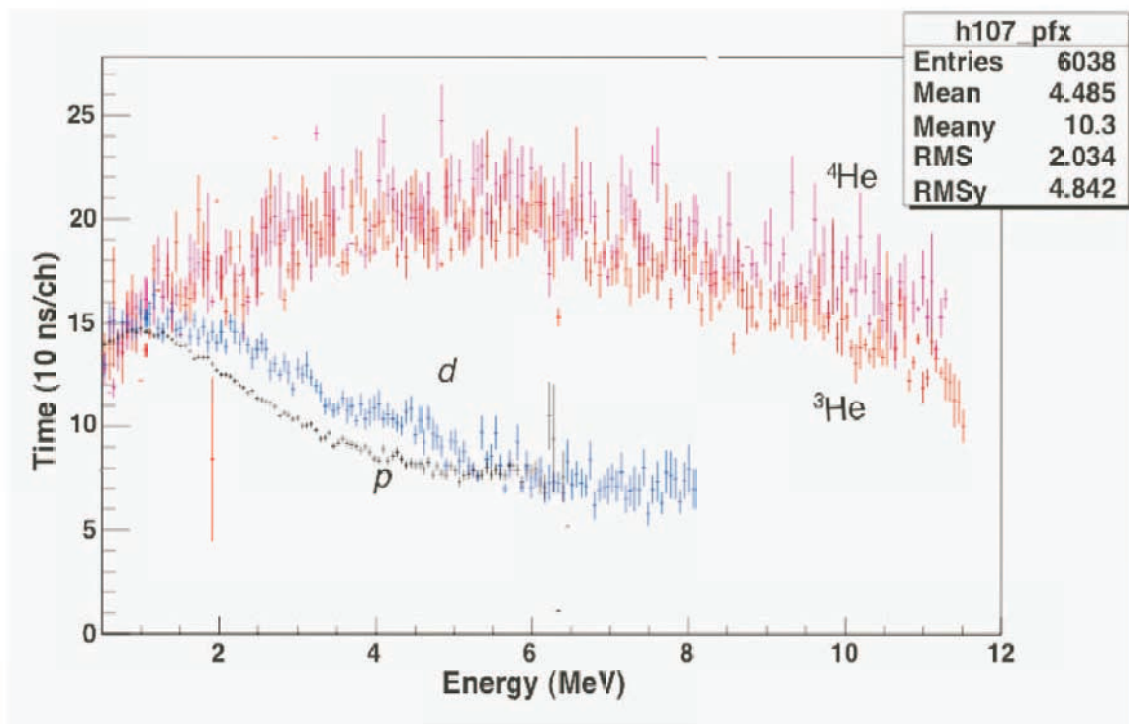


Fig. 1. The relation between the energy and the rise time (see in the text) is shown for light charged particles as indicated in the figure.



**3.**

**ATOMIC AND SOLID STATE PHYSICS,**

**AND**

**CLUSTER SCIENCE**



### 3.1 Evolution of resonant coherent excitation of hydrogen-like fast ions

H. Wakamatsu, S. Tomita, S. Kanda and H. Kudo

We have previously observed resonant coherent excitation (RCE) applying 180° electron spectroscopy for detection of K-shell electrons ionized from projectile  $C^{5+}$ , that are enhanced by RCE [1]. This observation technique allows studies of RCE at an extremely thin layer of crystal surface where RCE develops with increasing the number of encountering aligned atoms  $n$ . Furthermore, we may use bulk crystals, rather than self-supported crystal foils, so that target preparation becomes much easier. In this report, recent progress on the RCE studies is presented.

Figure 1 shows energy spectra of electrons induced by 4.84 MeV/u  $O^{7+}$  and  $O^{8+}$  incident on Si crystals under Si<110> channeling incidence conditions. The yield is shown for the same number of the incident projectiles and, accordingly, the excess electron yield for  $O^{7+}$  at energies lower than the loss-peak energy  $E_L$  and higher than the Si K-shell Auger peak at  $\sim 1.5$  keV is due to the ionized K-shell electrons from  $O^{7+}$ . The lower yield for  $O^{7+}$  below  $\sim 1.1$  keV stems from the suppressed electron emission by the screened Coulomb field of  $O^{7+}$  compared with the pure Coulomb field of  $O^{8+}$ .

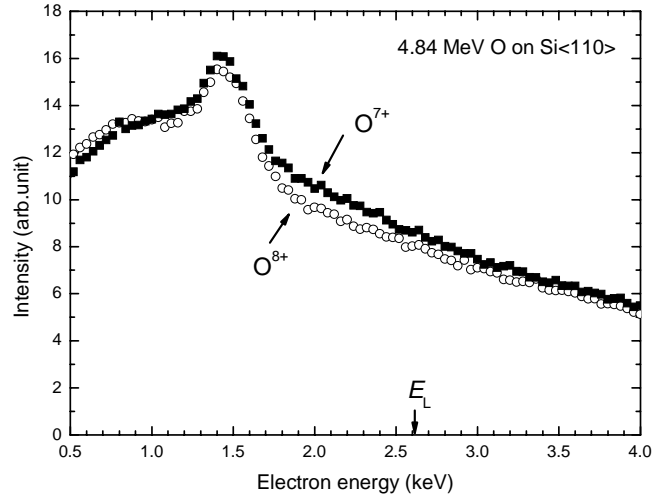


Fig. 1 Energy spectra of electrons induced by 4.84 MeV/u  $O^{7+}$  and  $O^{8+}$  under Si<110> channeling incidence conditions.

Figure 2 shows the dependence of the loss electron yield as a function of incident  $O^{7+}$  energy. We see a sharp resonance peak at the calculated resonance energy of 4.75 MeV/u. The peak results from the enhanced ionization of K-shell electrons of  $O^{7+}$  under the RCE conditions for the second harmonics.

In the first order perturbation, the transition probability of RCE is given by,

$$\begin{aligned}
 q(n, T) &= \frac{1}{\hbar^2} \left| \int_0^{nT} \langle \phi_2 | H'(\tau) | \phi_1 \rangle \exp(i\omega_0 \tau) d\tau \right|^2 \\
 &= \frac{D(n, T)}{\hbar^2} \left| \int_0^T \langle \phi_2 | H'(\tau) | \phi_1 \rangle \exp(i\omega_0 \tau) d\tau \right|^2, \quad (1)
 \end{aligned}$$

where  $T$ , the interatomic spacing divided by the ion speed, is the period of perturbation,  $\omega_0$  is the angular frequency corresponding to the excitation energy from  $\phi_1$  ( $n=1$ ) to  $\phi_2$  ( $n=2$ ) states,  $H'(\tau)$  is the screened Coulomb potential exerted from a Si atom, and  $D(n, T)$  is the diffraction function, i.e.,

$$D(n, T) = \frac{\sin^2(n\omega_0 T / 2)}{\sin^2(\omega_0 T / 2)} . \quad (2)$$

It is noted that in this treatment we have assumed straight-line trajectories of the ions in the Si crystal, which holds only for well channeled ions.

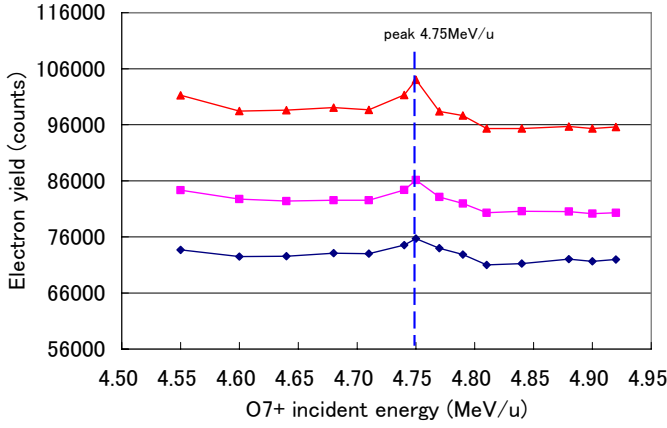


Fig. 2 Dependence of the loss electron yield as a function of incident  $O^{7+}$  energy. The RCE peak is seen at the calculated resonance energy of 4.75

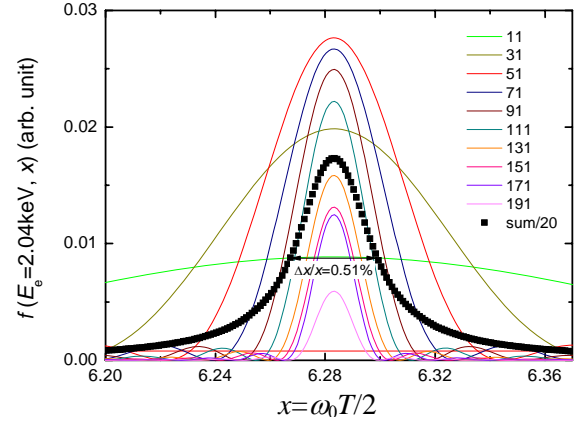


Fig. 3 Calculated resonance curve (square dots) of RCE for the second harmonics, which are constructed from eq. (2) for various  $n$  (shown in solid lines).

The loss electrons generally undergo elastic and inelastic collisions in the escape paths to the surface. Such processes can be reproduced numerically by semi-classical calculations [2]. Actually, we can calculate energy spectra of K-shell electrons emitted from the surface after suffering elastic and inelastic collisions in Si as a function of the depth where K-shell ionization occurs. In this manner, we may obtain the loss electron yield against the incident ion energy, i.e., the resonance profile of RCE. The results for 2.04-keV electron emission are shown in Fig. 3. The full width at half maximum of the RCE peak,  $\Delta x/x=0.51\%$ , corresponds to  $\Delta E/E=2(\Delta x/x)=1.02\%$  in the energy space. This value is in good agreement with the observed value of  $\Delta E/E = (0.96 \pm 0.15)\%$ . It is therefore evident that the evolution of RCE can essentially be accounted for in terms of the development of diffraction in the time space.

## References

- [1] H. Kudo, M. Nagata, H. Wakamatsu, S. Tomita, Nucl. Instrum. & Methods, B **229** (2005)227.
- [2] S. Valkealahti, R. M. Nieminen: Appl. Phys. A **32**, (1983)95.

## 3.2 Vicinage effect in the yield of convoy electrons under irradiation of fast carbon cluster ions

S. Tomita, S. Yoda, R. Uchiyama, S. Ishii, K. Sasa, and H. Kudo

When closely-spaced atoms e.g. clusters are incident on a surface, the interference in the collision-induced processes by the neighbor atoms can affect the emission of secondary particles. This is called the ‘‘vicinage effect’’, which has been observed for fast molecular or cluster ion beams [2]. We performed measurements of a vicinage effect in the yield of convoy electrons, which provides information concerning the number of primary scattered electrons under cluster irradiation.

Beams of carbon cluster ions were delivered by the 1 MV tandem accelerator at the University of Tsukuba. The cluster ions from the accelerator impinged on an amorphous carbon foil where a voltage of  $V = -50$  V was applied. About 1 cm downstream from the target, a grounded plate was placed, so that the emitted electrons in the forward direction were accelerated and detected in an electron spectrometer. The spectrometer is a  $45^\circ$  parallel-plate electrostatic spectrometer of the double deflection type. The electrons were counted by a channeltron detector whose anode potential was set to 200 V to increase the detection efficiency of low energy electrons. The energy of the carbon clusters  $C_n^+$  ( $n = 1$  to 4) was 0.5 MeV/atom, and the beam current was a few pA. The foils used were purchased from Arizona Carbon Foil, and had thicknesses of 1.8, 5.6, 11.0 and 19.3  $\mu\text{g}/\text{cm}^2$ . The vacuum pressure was  $\sim 5 \times 10^{-6}$  Pa during the beam irradiation.

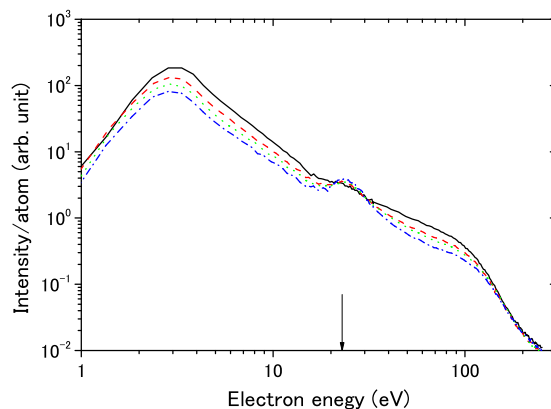


Fig. 1. Energy spectra of secondary electrons produced by irradiation of  $C^+$  (solid line),  $C_2^+$  (dash line),  $C_3^+$  (dot line), and  $C_4^+$  (dash-dot line) on a  $5.6 \mu\text{g}/\text{cm}^2$  carbon foil. Arrow indicates the energy of electrons which have same velocity as the projectile ions.

Typical energy spectra of the emitted electrons are shown in Fig.1. The spectra were normalized to the number of injected atoms instead of the number of cluster ions. The negative vicinage effect, i.e., the reduced electron yield for cluster injection, is clearly recognized at energies  $E_e < 150$  eV while the yield for cluster injection is larger around the peak located at  $E_e \sim 23$  eV. The reduction of the electron yield at low energies are also observed in backward electron emission [3]. The peak at  $E_e \sim 23$  eV corresponds

to electrons which have the same velocity as the projectile ions, i.e. convoy electrons. The position of the peak does not depend on the cluster size, but the area of the peak is enhanced for  $C_4^+$  relative to  $C_1^+$ , in contrast to the negative vicinage effect observed in the continuum yield (Fig.1).

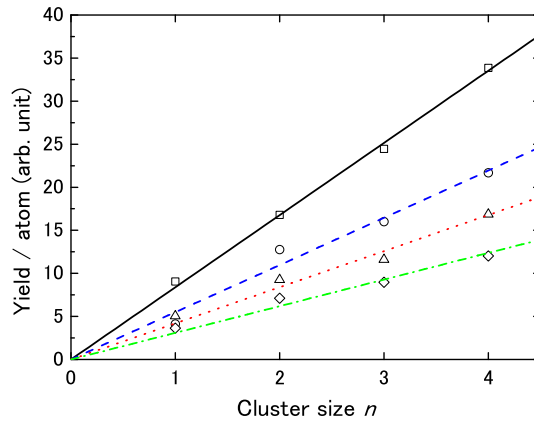


Fig. 2. Yield of convoy electrons produced by 0.5 MeV/atom  $C_n^+$  ion bombardment of 1.8 (open squares), 5.6 (open circles), 11.0 (open triangles), and 19.3  $\mu\text{g}/\text{cm}^2$  carbon foils (open diamonds). Lines are from a least square fits.

In Fig.2, the size dependence of the convoy electron yield is shown for the four different carbon foil thicknesses. It is interesting that the yield per injected atom shows a clear proportionality with  $n$ . The yield for  $C^+$  decreases for thick foils but the proportionality still remains even for the thickest foil of 19.3  $\mu\text{g}/\text{cm}^2$ . This observed proportionality can be understood if the convoy electrons stem from electron capture of primary scattered electrons to the continuum state of the projectile ion. The results obtained for the yield of the convoy electrons suggest that the number of scattered electrons is proportional to the number of projectile atoms. This leads us to conclude that the strong vicinage effect in the continuum spectra stems from either electron transport inside the foil or transmission through the surface.

## References

- [1] M. Breinig et al., Phys. Rev. A, **25**, 3015 (1982).
- [2] D. Jacquet and Y. Le Beyec, Nucl. Instr. and Meth. in Phys. Res. B **193**, 227 (2002).
- [3] H. Kudo et al., Jpn. J. Appl. Phys. (2006), in press.

### 3.3 Mössbauer study on $\gamma$ -Fe<sub>2</sub>O<sub>3</sub> thin films

M. Hasegawa, K. Shibata, H. Yanagihara, E. Kita

$\gamma$ -Fe<sub>2</sub>O<sub>3</sub>(maghemite) has been used as magnetic recording media. However, the physical properties are not well understood because this iron oxides is in a metastable state and it is hard to grow the single crystals. Crystal structure of  $\gamma$ -Fe<sub>2</sub>O<sub>3</sub> is believed to be close to Fe<sub>3</sub>O<sub>4</sub>(magnetite); an inverse spinel ferrite of which one third of the B-site irons are vacant. It is frequently written as Fe<sub>A</sub><sup>3+</sup>[Fe<sub>5/3</sub><sup>3+</sup> X<sub>1/3</sub>]<sub>B</sub>O<sub>4</sub><sup>2-</sup> (X stands for Fe vacancy). Consequently, the maghemite is expected to be an insulator and to show small magnetic anisotropy due to no orbital angular momentum. Recently, the growth techniques for  $\gamma$ -Fe<sub>2</sub>O<sub>3</sub> epitaxial films were developed by several groups[1, 2]. An x-ray diffraction analysis revealed that the unit cell of the grown film is three times larger than that of Fe<sub>3</sub>O<sub>4</sub>[2] and that the B-site vacancies are fully ordered with *c*-axis parallel to the film growth direction. Most of physical properties, however, are still unrevealed.

We report magnetic properties of  $\gamma$ -Fe<sub>2</sub>O<sub>3</sub> epitaxial films on MgO(001). The film growth method can be found in Ref.[2]. The typical thickness of the films reported here was around 100 Å. Ferromagnetic resonance (FMR) were carried out. A frequency of the microwave for FMR measurements was 9.75 GHz. The FMR experiments were performed with the static field applying parallel to the (001) plane. We performed conversion electron Mössbauer spectroscopy (CEMS).

Fig. 1 shows in-plane angle  $\theta$  dependence of the resonance field.  $\theta$  was defined as the angle between [100] and applied static field direction in (001) plane. This result indicates that the in-plane [110] and [100] directions seem to be magnetic easy and hard axes, respectively.

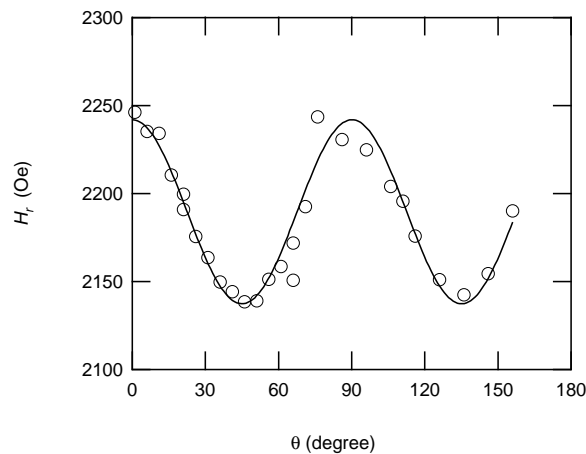


Fig. 1. The angle  $\theta$  dependence of the resonance field( $H_r$ ).  $\theta$  was defined the angle between [100] and the static field direction. The solid line stands for the fit result with equation(1). Two-fold component due to a small misalignment is subtracted from the raw data.

Moreover,  $\gamma$ -Fe<sub>2</sub>O<sub>3</sub> possibly shows uniaxial magnetic anisotropy associated with the three-fold tetragonal crystal structure[2]. Therefore in-plane four-fold symmetric anisotropy and the additional out-of-plane uniaxial anisotropy can coexist. In order to extract both constants of cubic anisotropy( $K_1$ ) and uniaxial anisotropy( $K_u$ ), we quantitatively analyzed  $\theta$ -dependent FMR data using the resonance condition

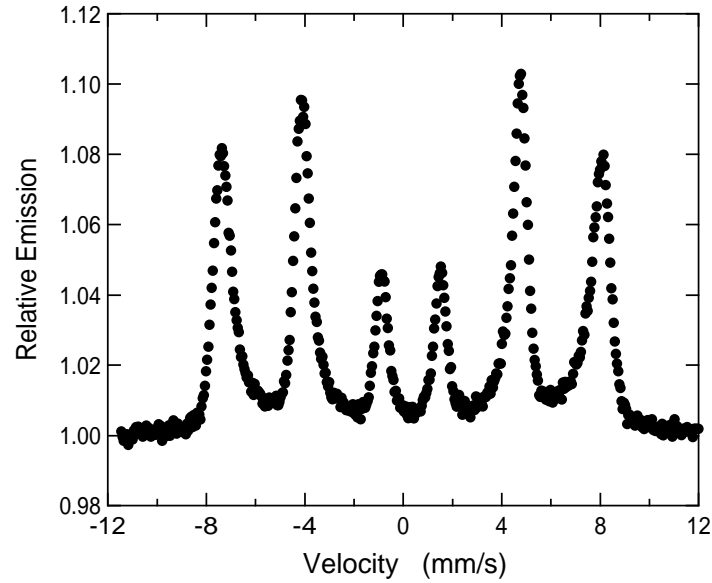


Fig. 2. Conversion Electron Mössbauer Spectrum(CEMS) of  $\gamma$ -Fe<sub>2</sub>O<sub>3</sub> films with the thickness of around 70 Å recorded at room temperature.

derived from Ref. [3].  $K_1$  and  $K_u$  were estimated to be  $-1.3 \times 10^5$  and  $3.0 \times 10^5$  erg/cm<sup>3</sup>, respectively. The sign of  $K_u$  is positive, suggesting that energetically perpendicular preferential term exists but is smaller than the demagnetization field.

In Fig. 2 the spectrum of CEMS for 70 Å thick  $\gamma$ -Fe<sub>2</sub>O<sub>3</sub> film at room temperature. The sample for this experiment was prepared with <sup>57</sup>Fe enriched source. The spectrum of the simple sextet also supports that the film is not composed of the mixture of Fe<sup>3+</sup> and Fe<sup>2.5+</sup> (Fe<sub>3</sub>O<sub>4</sub>) but of only Fe<sup>3+</sup> ( $\gamma$ -Fe<sub>2</sub>O<sub>3</sub>). Note that the relative intensity ratio of the six lines is slightly apart from an ideal thin film magnet with a magnetic preferential direction parallel to the film plane. Theoretically, the six lines relate as 3:x:1:1:x:3,  $x=4\sin^2\phi/(1+\cos^2\phi)$ .  $\phi$  means the angle between the incident  $\gamma$ -rays and the direction of the magnetic hyperfine field. The estimated angle  $\phi$  is about 60 degree, suggesting the zero-field magnetization has a finite normal component to the plane which is qualitatively in agreement with the results of Voogt *et al.*[1].

## References

- [1] F. C. Voogt, T. Fujii, P. J. M. Smulders, L. Niesen, M. A. James and T. Hibma, Phys. Rev. B **60** (1999) 11193.
- [2] H. Yanagihara, M. Hasegawa, E. Kita, Y. Wakabayashi, H. Sawa, and K. Siratori, J. Phys. Soc. Jpn. **75** (2006) 054708.
- [3] A. H. Morrish, *The physical principles of magnetism* (Wiley-IEEE Press, 2001) p542.
- [4] G. Bate *Magnetic Oxides* ed. D. J. Craik, Wiley, London, (1975) p.689.

### 3.4 The science of 3d transition-metal oxide system (2005–2006)

M. Onoda, T. Ikeda, K. Takao, Y. Kikuchi, A. Sasaki, Y. Ishitsuka, W. Onoda, T. Maekoya, Y. Mizuguchi and N. Yamazaki

The structural and electronic properties of 3d transition-metal oxides and bronzes have been explored by means of x-ray four-circle diffraction and through measurements of magnetic resonance (NMR and ESR), magnetization, and electronic transport, in order to extract characteristic properties in the **quantum spin-fluctuation system, correlated electron system, electron-phonon-coupling system, and novel materials** such as **a new type of superconductors, composite crystals and secondary ion batteries** [1-4]. At the Tandem Accelerator Center, Varian continuous-wave and Bruker pulse NMR spectrometers have been used. This report describes briefly recent progress for the secondary ion battery system [1, 3, 4].

Typical insertion electrode systems for vanadium oxides,  $\text{Li}_{1+x}\text{V}_3\text{O}_8$  and  $\text{Li}_x\text{V}_6\text{O}_{13}$ , can accommodate around three or four additional Li ions per formula unit of  $\text{LiV}_3\text{O}_8$  and eight ions per  $\text{V}_6\text{O}_{13}$ , respectively. These lithiations may supply new kind of compound series for the investigation on quantum-spin fluctuation and correlated electron systems. In order to construct this situation and to improve battery performances, the basic properties as a function of the Li concentration have been studied. The cw-NMR results for the linewidths of  $^7\text{Li}$  nuclei in  $\text{Li}_{1+x}\text{V}_3\text{O}_8$  were understood successfully as described in a report in 2004–2005. In this report, the MAS-NMR results for  $\text{Li}_{1+x}\text{V}_3\text{O}_8$  with  $x = 0, 0.25$  and  $3.2$ , the last composition being prepared electrochemically, measured at 233.23 and 116.61 MHz between 240 and 390 K are discussed.

The central spectra are decomposed to two or three Lorentzians assuming axial or isotropic contribution for the shift. Here, it should be noted that for Li1 with  $x = 0$ , the second-order quadrupole effect can be neglected. For  $x = 0$ , there exist two resonance lines named A and B. Using the relative intensity for each line, the Li concentrations normalized to the nominal value against temperature are estimated as shown in Fig. 1(a). The Li concentrations do not depend on temperature, and the A- and B-lines may be attributed to the signals from Li1 and Li2 sites, respectively, since the Li2 ion appears to exist slightly even when the nominal concentration is fixed at  $x = 0$ . Note that the slight occupation of Li2 gives rise to unpaired spins for V ions. The temperature dependences of the shifts and the spin-lattice relaxation times for  $x = 0$  are indicated in Figs. 1(b) and 1(c), respectively. The shift for Li2 is almost zero, but that for Li1 increases negatively with decreasing temperature. The latter result may correspond to a sum of the hyperfine shift via the Fermi contact interaction and temperature-independent terms. The hyperfine shift  $\delta$  depends linearly on the magnetic susceptibility,  $\delta = H_{\text{hf}}\chi/(N\mu_{\text{B}})$ , where  $H_{\text{hf}}$ ,  $\chi$ ,  $N$  and  $\mu_{\text{B}}$  are the hyperfine field, the susceptibility, the number of magnetic V ions and the Bohr magneton, respectively. The full curve in Fig. 1(b) provides  $H_{\text{hf}} = -26(3) \text{ mT } \mu_{\text{B}}^{-1}$ . The origin of the negative  $H_{\text{hf}}$  value or the spin transfer mechanism may be originated by spin polarization effects due to the exchange interactions. The  $T_1$  for Li1 with  $x = 0$  is linear in temperature, which suggests that the relaxation is of the quadrupole type for the rotational motion of Li ions. With the extreme narrowing condition and the nuclear spin  $I = 3/2$ , this is written by  $1/T_1^{\text{Q}} = 10^{-1}(1 + \eta^2/3)(e^2qQ/h)^2\tau_{\text{c}}$ , where  $\tau_{\text{c}}$  is an effective correlation time for the motion and it is proportional to the inverse of temperature. The full line in Fig. 1(c) leads to  $\tau_{\text{c}} \simeq 7.9 \times 10^{-7}/T$  s. The  $T_1$  for Li2 seems to have a temperature dependence similar to that for Li1. It is not necessary

to consider the hyperfine interaction for the main relaxation mechanism, since the relaxation rates of the A-line for the different compositions are similar to that for  $x = 0$ .

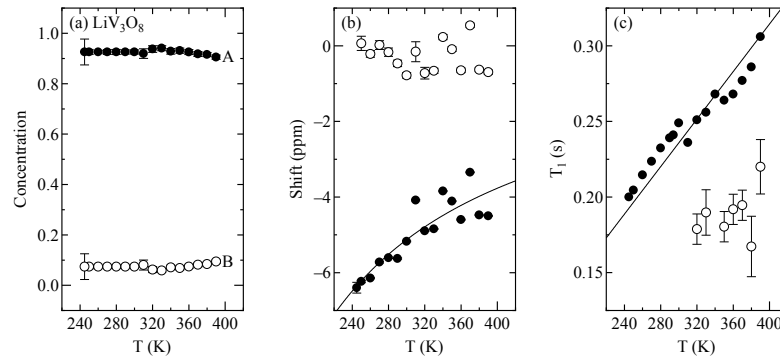


Fig. 1. The temperature dependences of (a) the Li concentrations normalized to the nominal value; (b) the shift; and (c) the spin-lattice relaxation times for  $^7\text{Li}$  nuclei in  $\text{LiV}_3\text{O}_8$ .

For  $x = 0.25$ , three resonance lines (A, B and C) exist above 270 K and at 260 K, the D-line with more negative shift appears. At the lower temperature, it is difficult to distinguish between the B- and C-line. The A- and B-lines are originated from the Li1 and Li2 sites, respectively, and the C-line may come from another tetrahedral Li site. Since the V ion is more reduced and the compound is more magnetic as compared with those for  $x = 0$ , the hyperfine shifts for the Li1 and Li2 ions increase more negatively. The  $H_{\text{hf}}$  values for Li1 and Li2 are  $-21(2)$  and  $-9(2)$  mT  $\mu_{\text{B}}^{-1}$ , respectively. Below 260 K, these shifts show opposite temperature dependences and the shift for D-line increases negatively. This result suggests the occurrence of phase transition for the local environments of Li. The  $T_1$ 's for  $x = 0.25$  are the same order with those for  $x = 0$ , but their temperature dependences are weak due to an increase of the temperature-independent contribution from the exchange coupled V ions via a transferred hyperfine interaction. There exist small anomalies above 260 K, at which the local environments of Li change. Details for  $x = 3.2$  are written in ref. 1.

In summary, MAS-NMR spectra for the  $\gamma_1$ -phase clearly reflect the site differentiation for Li. The spin-lattice relaxation for  $x = 0$  is explained with the quadrupole interaction mechanism. For  $x = 0.25$ , the phase transition for the Li local environments occurs at 260 K with VRH-type transport anomaly. The spectra for the  $\gamma_2$ -phase are significantly different from those for the  $\gamma_1$ -phase and the complicated relaxations are detected.

## References

- [1] M. Onoda, S. Miyasaka, T. Mutoh and K. Nichogi: J. Phys.: Condens. Matter **17**(26) (2005) 4057–4071.
- [2] M. Onoda and J. Hasegawa: J. Phys.: Condens. Matter **18**(7) (2006) 2109–2123.
- [3] Masashige Onoda and Mitsuko Onoda: Phys. Rev. B **73** (2006) 104108 [7 pages].
- [4] M. Onoda: Ceramics **41**(3) (2006) 167–172 [in Japanese].

### 3.5 Oxidations of cobalt clusters

M. Kubo, T. Sugaya, I. Arai and K. Sugawara<sup>1</sup>

The oxidation reactions of metal clusters have been studied for many years to understand their size-dependent chemical properties and to gain insight into their reaction mechanism on metal surface related to corrosion or catalytic processes.

With respect to reaction of nickel cluster cations with oxygen, the reaction products were observed after  $10^1$  to  $10^3$  collisions with  $O_2$  using FT-ICR mass spectrometry so far. It was found that the most abundant final products were  $Ni_{13}O_8^+$  and  $Ni_{16}O_{10}^+$  which reacted with neither  $O_2$  nor  $H_2O$  under the  $O_2$  pressure  $10^{-6}$  to  $10^{-4}$ Pa and the reaction time 1 to 20 sec at room temperature.

In order to compare nickel with cobalt, the experiments of reactions of cobalt clusters with  $O_2$  have been carried out under the  $O_2$  pressure  $10^{-6}$  to  $10^{-4}$ Pa and the reaction time 0.1 to 10 sec at room temperature. We have searched the similarities and discrepancies between cobalt clusters and nickel clusters.

The experimental set up mainly consists of a laser vaporization cluster source and an FT-ICR mass spectrometer. The cobalt cluster cations  $Co_n^+$  are produced by laser vaporization of rotating cobalt rod. They are introduced into an FT-ICR chamber and trapped by collisions with  $O_2$ , where the  $O_2$  pressure is  $10^{-6}$  to  $10^{-4}$ Pa. We have measured the mass spectra under the reaction time 0.1 to 10 sec at room temperature.

In these experiments, the most abundant final product was  $Co_{13}O_8^+$ , which was similar to the case of oxidations of nickel clusters. But, we could not find any stable  $Co_{16}O_{10}^+$ . Further examination of such similarities and discrepancies between the oxidation of  $Ni_n^+$  and that of  $Co_n^+$  is under progress now.

---

<sup>1</sup> Nanotechnology Research Institute, AIST

### 3.6 Estimation of Eu concentration in Eu-doped GaN by RBS measurements

J. Sawahata, J.W. Seo, S.Nemoto and K. Akimoto

Rare earth (RE) doped GaN thin films have attracted great interests due to their unique optical properties, that is, luminescence due to an intra 4f transition of RE ion depends very little on the host material and the temperature. Among the several RE dopants, it is well known that europium (Eu) shows a strong red emission around 622 nm. The Eu concentration in the films is a one of important parameters on the optical properties of Eu-doped GaN. Therefore, we performed Rutherford back scattering (RBS) measurements to estimate Eu concentration in Eu-doped GaN.

The Eu-doped GaN thin films were grown on GaN/Al<sub>2</sub>O<sub>3</sub> substrates by molecular beam epitaxy methods [1]. The RBS measurements were carried out using 1.5 MeV accelerated <sup>4</sup>He ions with a tandem accelerator placed at UTTAC. The geometry of incident angle, exit angle and scattering angle were 30, 0 and 150 degrees, respectively. A detector was placed at 70 mm from the sample surface.

Fig. 1 shows a RBS spectrum of Eu-doped GaN as an example. The spectrum heights of the edges corresponding to scattering from the surface atoms were used for calculation of Eu concentration. In Fig.1, the Eu concentration was estimated at 3 at.%. The red emission intensity of Eu-doped GaN increased up to an Eu concentration of 3 at.%, and then it decreased for Eu concentration of more than 3 at.%. Therefore, we found that an optimum Eu concentration on the optical properties of Eu-doped GaN is estimated around 3 at.% by RBS measurements.

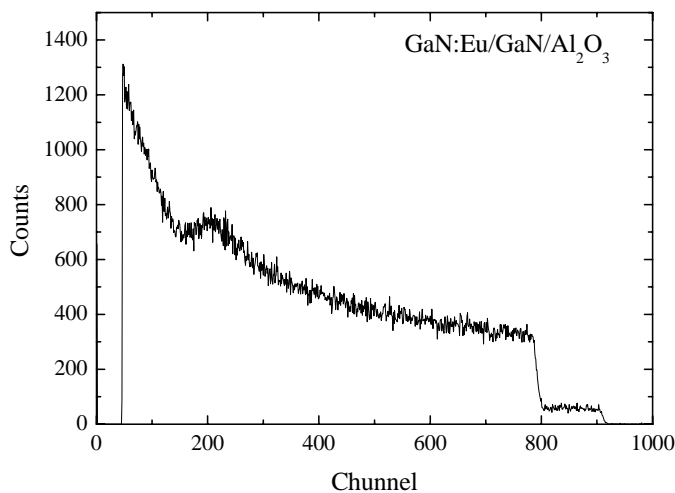


Fig. 1 RBS spectrum of Eu-doped GaN

#### References

- [1] H. Bang, S. Morishima, J. Sawahata, J. Seo, M. Takiguchi, M. Tsunemi, K. Akimoto, Appl. Phys. Lett. 85, 227 (2004)

**4.**

**ION BEAM ANALYSIS AND APPLICATION**



## 4.1 Status of Tsukuba AMS system

Y.Nagashima, K.Sasa, T.Takahashi, R.Seki, Y.Tosaki, K.Sueki, K.Bessho, H.Matsumura, T.Miura and K.Masumoto

In the last year, we lost several scheduled AMS measurements because of unexpected problems happened on the 12UD tandem. In contradistinction to the last year, we could exhaust all of scheduled AMS machine times with a successful results this year. In parallel with the AMS measurements, a performance improvement of an AMS ion source system has been done. We report, first, the improvement done in this year, and second, the experimental results are reported briefly.

The dating of ice core sampled at the Fuji dome in the Antarctica Continent as a big national project is commenced. The depth of the ice bed at the Fuji dome is about 3,000m and the core samples are collected from the surface to the 3,000m depth. It is estimated that the age of the core sample at the 3,000m depth is ~100 million years old. Therefore, it is expected that the core sample memorizes the record of not only an environmental change of the earth but also a change of a solar activities for the 100 million years. To investigate and to understand the change, the measurement of  $^{36}\text{Cl}$  element in the ice core has been commenced by mean of  $^{36}\text{Cl}$ -AMS.

A calculated fall out of the  $^{36}\text{Cl}$  on the ice bed is ~60 atoms/m<sup>2</sup>/s and the number of the  $^{36}\text{Cl}$  in the ice core is ~ $6 \times 10^3$  atoms/g. The  $^{36}\text{Cl}/\text{Cl}$  ratio is estimated to be the range from  $10^{-14}$  to  $10^{-15}$ . To accommodate lowering the  $^{36}\text{Cl}/\text{Cl}$  ratio, several improvements has been performed in the AMS ion source. A 120° ion source magnet was newly designed and replaced with an old one for improving a beam displacement. Fig. 1 shows outline of the new 120° magnet. The size of the  $^{35}\text{Cl}$  beam is decreased from ~4mm to ~2mm in diameter. The small displacement makes an efficiency and stability of a beam transmission in the accelerator tubes better.

The beam optics for the ion source has been calculated again for finding out the optimum operating condition. The best condition we got is shown in Fig. 2. As a result of the calculation, we understand that the shape of both an ionizer and an extraction electrode are not ideal. Therefore, they were replaced with newly designed ones and, consequently, the  $^{35}\text{Cl}$ - ion current increased and reached to ~40μA. The strong  $^{35}\text{Cl}$  current helps very much to realize the measurement of the samples with very small  $^{36}\text{Cl}/^{35}\text{Cl}$  ratio.

The first East Asian AMS Symposium (EAAMS-1), and the 8th Japanese AMS Symposium (JAMS-8), have been organized by the Tsukuba AMS group and successfully concluded. It was attended by 120 peoples from 4 countries which are Korea, China, USA, and Japan. The contributions to the symposiums, both technical and applied, clearly demonstrated that AMS has evolved into a versatile tool to study our world, especially our East Asia. The Proceedings of both Symposiums contain 44 papers covering a large fraction of the contributions presented at the symposium. The second East Asian AMS Symposium will be held in Korea in 2007.



## 4.2 $^{129}\text{I}$ -AMS by the Tsukuba AMS system

K. Sasa, Y. Nagashima, T. Takahashi, R. Seki, Y. Tosaki, K. Sueki, B. H. Zhou

A  $^{97}\text{Mo}^{16}\text{O}_2$  molecular pilot beam method is applied to the  $^{129}\text{I}$  measurement by the Tsukuba AMS system [1]. The ions extracted from the ion source are selected by a  $120^\circ$  mass separator. The beam current of  $^{127}\text{I}^-$  is measured by an off-set Faraday cup just set at an image of the  $120^\circ$  mass separator simultaneously with the  $^{129}\text{I}$  ions in the detector.  $^{129}\text{I}^-$  and  $^{97}\text{Mo}^{16}\text{O}_2^-$  ions are accelerated concurrently and  $^{129}\text{I}^{12+}$  and  $^{97}\text{Mo}^{9+}$  can pass through the  $90^\circ$  analyzing magnet. Once the analyzing magnet is adjusted for  $^{129}\text{I}^{12+}$ ,  $^{97}\text{Mo}^{9+}$  ions pass through about 5 mm down at an image point of the magnet and produce the slit current for the slit current feedback terminal potential stabilizer. A magnetic rigidity of  $^{97}\text{Mo}^{9+}$  is almost the same as that of  $^{129}\text{I}^{12+}$ , so that a second stripper foil is prepared in an AMS beam line in order to sweep out the  $^{97}\text{Mo}^{9+}$  ions. After passing through the second stripper foil,  $^{129}\text{I}^{26+}$  is selected as a detection particle. On the other hand, no  $^{97}\text{Mo}$  particles can enter the detector because the magnetic rigidity of  $^{97}\text{Mo}^{n+}$  is different from that of  $^{129}\text{I}^{26+}$ . Finally,  $^{129}\text{I}^{26+}$  ions are clearly detected by a silicon surface barrier detector. The terminal voltage is set to 9.68 MV in order to get most efficient yields of both  $^{129}\text{I}^{12+}$  and  $^{129}\text{I}^{26+}$ . Fig. 1 shows the one-dimensional spectrum for  $^{129}\text{I}$  measurement. A standard sample was prepared from the NIST standard.

At present, we plan to measure  $^{129}\text{I}$  concentrations in soils of the Semipalatinsk nuclear explosion test sites in Kazakhstan in collaboration with the Hiroshima University.

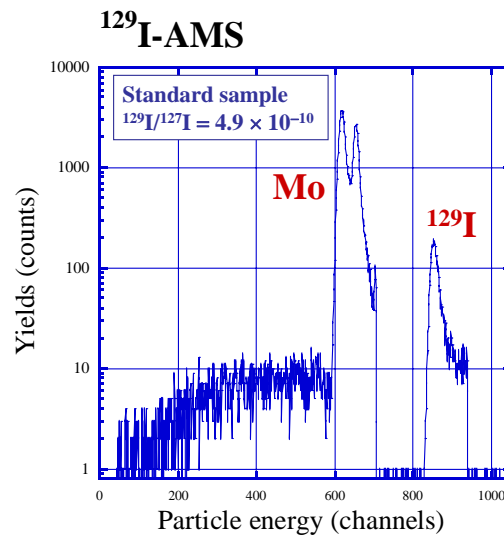


Fig. 1. One dimensional spectrum for a standard sample with a ratio of  $^{129}\text{I}/^{127}\text{I} = 4.9 \times 10^{-10}$  measured by a silicon surface barrier detector.  $^{129}\text{I}$  is clearly separated from the isobaric ions.

### References

[1] K. Sasa, Y. Nagashima, T. Takahashi, R. Seki, Y. Tosaki, K. Sueki, K. Bessho, H. Matsumura, T. Miura, S. Jiang and M. He, Proceedings of the First East Asian Symposium on Accelerator Mass Spectrometry, UTTAC-74 (2006) 69-80.

### 4.3 Test measurement of $^{36}\text{Cl}$ concentration in an ice core retrieved from the Dome Fuji station in Antarctica.

K. Sasa, Y. Tosaki, Y. Nagashima, T. Takahashi, R. Seki, K. Sueki, B. H. Zhou, K. Bessho<sup>1</sup>, H. Matsumura<sup>1</sup>, T. Miura<sup>1</sup>, Y. Shibata<sup>2</sup> and H. Motoyama<sup>3</sup>

In 2006, Japanese glaciological group succeeded in drilling the deep ice core with a depth of 3028 m at the Dome Fuji station on the one of summits of East Antarctica. AMS group of the University of Tsukuba takes part in the joint research project for analyzing the cosmogenic radioisotopes  $^{10}\text{Be}$  ( $T_{1/2} = 1.51 \times 10^6$  years),  $^{26}\text{Al}$  ( $7.16 \times 10^5$  years) and  $^{36}\text{Cl}$  ( $3.01 \times 10^5$  years) in the ice core retrieved at the Dome Fuji station in collaboration with National Institute of Polar Research, National Institute for Environmental Studies, Hirosaki University and the University of Tokyo. The concentrations of cosmogenic radioisotopes in the ice core provide useful information about the history of the cosmic ray flux in the atmosphere, the past solar activity and the past earth environment such as changes in the geomagnetic field.

We measured  $^{36}\text{Cl}$  concentration in a test sample retrieved as ice chips at around 100 m depth at the Dome Fuji station previous to the regular AMS measurement. The age of the test sample corresponds to about 2 kyr B.P.. The sample melted from ice chips with 505.9 g weight was used for this test measurement. After adding 0.92 mg of stable chlorine as carrier to the sample,  $^{36}\text{Cl}$  and the carrier were extracted together by means of anion exchange resin. The sample treatment is described elsewhere in detail [1]. The sample was formed as AgCl and pressed on the aluminum cathode. It was analyzed by using the Tsukuba AMS system [2]. The effective detection limit is reached to  $1.5 \times 10^{-14}$  for  $^{36}\text{Cl}/\text{Cl}$  ratio. The result of  $^{36}\text{Cl}$  measurement is presented in Table 1. The measured  $^{36}\text{Cl}/\text{Cl}$  ratio is  $2.49 \times 10^{-13}$ . The  $^{36}\text{Cl}$  concentration in the test sample corresponds to 7,680 atoms  $\text{g}^{-1}$ . This result means that the Tsukuba AMS system has an excellent performance to analyze the  $^{36}\text{Cl}$  concentration in the ice core with the range of the past million years.

Table 1. The result of  $^{36}\text{Cl}$  measurement in a test sample retrieved as ice chips at around 100 m depth.

$^{36}\text{Cl}/\text{Cl}$	error	Cl [mg/g]	$^{36}\text{Cl}$ [atoms/g]	error
2.49E-13	3.20E-14	0.0018	7.68E+03	9.88E+02

#### Acknowledgements

This work is supported in part by the Grants-in-Aid for Scientific Research Program of the Ministry of Education, Culture, Sports, Science and Technology, Japan.

#### References

- [1] Y. Tosaki and R. Seki, this annual report.
- [2] K. Sasa et al., Proceedings of the First East Asian Symposium on Accelerator Mass Spectrometry, UTTAC-74 (2006) 69-80.

<sup>1</sup> Radiation Science Center, High Energy Accelerator Research Organization

<sup>2</sup> National Institute for Environmental Studies

<sup>3</sup> National Institute of Polar Research

## 4.4 Bomb-produced $^{36}\text{Cl}$ in the Oderbruch aquifer, Germany: A preliminary result

Y. Tosaki, N. Tase, G. Massmann<sup>1</sup>, Y. Nagashima, R. Seki, K. Sasa, T. Takahashi, B. Zhou, K. Sueki, K. Bessho<sup>2</sup>, H. Matsumura<sup>2</sup> and T. Miura<sup>2</sup>

The potential use of bomb-produced  $^{36}\text{Cl}$  as a dating tool for modern groundwater has been investigated recently [1,2]. As a result of these studies, bomb-produced  $^{36}\text{Cl}$  was suggested to be a useful tracer in groundwater. However, previously measured groundwater samples correspond to tail part of bomb pulse period and pre- or post-bomb period [2,3]. For further investigation on bomb-produced  $^{36}\text{Cl}$  as a dating tool, measurement of groundwater of bomb peak period is necessary. In August 2005, new samples were collected from same wells and some additionally installed wells. These samples were prepared as  $\text{AgCl}$  and  $^{36}\text{Cl}/\text{Cl}$  ratios were measured by the AMS at the Tandem Accelerator Complex, University of Tsukuba. Preliminary result of  $^{36}\text{Cl}$  measurement of these samples is reported here.

The result of  $^{36}\text{Cl}$  measurement of 2005 samples is compared with that of 2003 samples in Fig. 1. These two distributions of  $^{36}\text{Cl}/\text{Cl}$  ratios along the flow path of groundwater are in fair agreement. Although higher values (near the bomb peak) had been expected at around 2500–3000 m apart from the river Oder, it was not clear from the result. There may be some influence from mixing of rainwater from the ground surface, because chloride concentration in groundwater becomes low at around 2500–3000 m. However,  $^{36}\text{Cl}/\text{Cl}$  ratio could be changed by the addition of chlorine from other sources. The  $^3\text{H}/^3\text{He}$  measurement of same groundwater samples will be conducted soon, therefore, detailed discussion will be made with  $^3\text{H}/^3\text{He}$  result.

### References

- [1] Y. Tosaki, N. Tase, Y. Nagashima, R. Seki, T. Matsuhiro, T. Takahashi, K. Sasa, M. He, K. Sueki, T. Miura, K. Bessho, H. Matsumura, UTTAC Annual Report 2003 (2004) 71.
- [2] Y. Tosaki, N. Tase, Y. Nagashima, R. Seki, T. Takahashi, K. Sasa, K. Sueki, T. Matsuhiro, M. He, T. Miura, K. Bessho, H. Matsumura, G. Massmann, UTTAC Annual Report 2004 (2005) 35.
- [3] J. Sültenfuß, G. Massmann, Grundwasser 9 (2004) 221 (in German with English abstract).

<sup>1</sup> Department of Earth Sciences, Free University of Berlin, Germany

<sup>2</sup> Radiation Science Center, High Energy Accelerator Research Organization

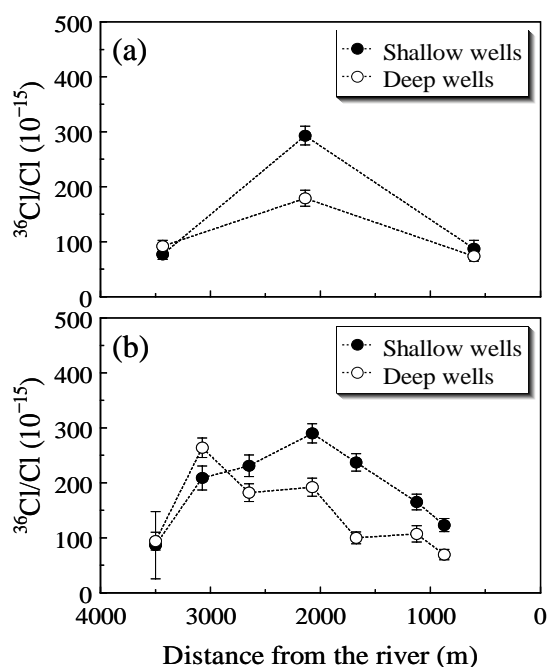


Fig. 1.  $^{36}\text{Cl}/\text{Cl}$  ratios for Oderbruch samples as a function of the distance from the Oder. a) 2003 samples. b) 2005 samples. Shallow well indicates upper part of the aquifer and deep well indicates lower part.

## 4.5 Improvements in sample preparation for $^{36}\text{Cl}$ -AMS

Y. Tosaki and R. Seki

Our previous sample preparation scheme [1,2] was basically developed referring to such as Conard et al. [3]. The scheme is very straightforward, but in case of groundwater, rainwater and ice samples, concentration of sample solution is frequently required. For these large-volume samples, evaporative concentration by heating had been employed. However, there may be a risk of sample contamination from the atmosphere during evaporation process. Additionally, sulfur reduction process included in the previous scheme (i.e. removal of sulfur as  $\text{BaSO}_4$  precipitate) is time-consuming [4], while it is not effective enough for our  $^{36}\text{Cl}$  AMS measurement of natural samples. For improving these problems, anion-exchange column method was tested because large-volume samples can be readily processed with minimum risk of contamination. Another advantage to be expected is the separation of sulfur through the elution process [5]. With this new method, total time required per sample is much less than previous method.

AG 4-4X anion-exchange resin in the free-base form (100–200 mesh; Bio-Rad Laboratories, Hercules, CA, USA) was used for our test experiment. First of all, 20 mL (wet volume) of the resin is transferred to a 60 mL Bond Elute column (Varian, Harbor City, CA, USA). Before use, the resin is cleaned by passing 4 M  $\text{HNO}_3$  through the column. After neutralization with Milli-Q water (better than 18  $\text{M}\Omega\cdot\text{cm}$ ; Millipore, Billerica, MA, USA), the resin is conditioned by 0.5 M  $\text{NH}_4\text{OH}$  and 2 M  $\text{NH}_4\text{OH}$ . The resin is neutralized again with Milli-Q water, and then it is ready to use.

Anion-exchange column method was tested for a blank sample ( $\text{NaCl}$  reagent) and an ice sample from Dome Fuji, Antarctica. As for the blank sample, about 0.91 mg of Cl (1.5 mg as  $\text{NaCl}$ ) was dissolved in 500 mL of Milli-Q water. Similarly, 0.92 mg of Cl carrier was added to 506 mL of melted ice sample. These solutions were acidified with the addition of  $\text{HNO}_3$  (pH  $\sim$ 2) and run through anion-exchange columns (Fig. 1). After finishing this process, 0.5 M  $\text{HNO}_3$  was passed through the column, and then Cl was eluted with 3 M  $\text{HNO}_3$ . From this step, procedure is similar to previous method. In order to precipitate  $\text{AgCl}$ , 0.3 M  $\text{AgNO}_3$  solution was added to the eluted solution. The  $\text{AgCl}$  precipitate was separated by centrifugation and dissolved with 3 M  $\text{NH}_4\text{OH}$ . The solution is filtered through 0.20  $\mu\text{m}$  PTFE filter (DISMIC-25HP, Advantec, Tokyo, Japan) and the filtrate was acidified by the addition of 13 M  $\text{HNO}_3$  to precipitate  $\text{AgCl}$  again. After these steps,  $\text{AgCl}$  precipitate was re-dissolved and re-precipitated in order to exclude remaining impurity. Finally,  $\text{AgCl}$  precipitate was washed three times with 0.01 M  $\text{HNO}_3$  and twice with 99.5%  $\text{C}_2\text{H}_5\text{OH}$ , and then dried in the oven at 130°C for 3 hours.

As a result, chemical yields of chlorine were 54% and 63% (Table 1), which are lower than previous method (about 80%). These two samples were measured by the AMS at the Tandem Accelerator Complex, University of Tsukuba. Against the expectation, there was no clear difference in count rate of  $^{36}\text{S}$  compared to previous method. However, the time required for chemical procedure is much reduced and the chemical yield is expected to be improved. This new sample preparation scheme is tested further and will be applied to ice core samples from Dome Fuji in the near future.

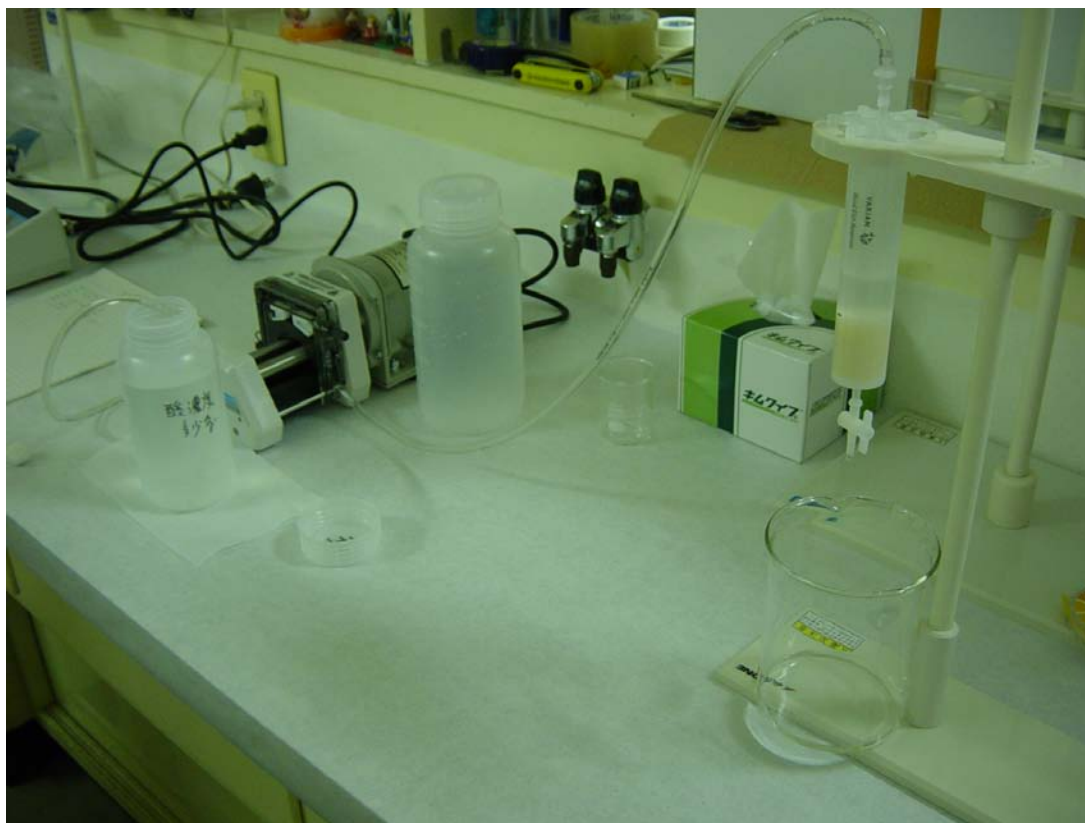


Fig. 1. A test sample is being passed through an anion-exchange column.

Table 1  
Chemical yields of chlorine for test samples

Sample	Cl carrier added (mg)	AgCl recovered (mg)	Chemical yield of Cl (%)
Blank sample	0.91	2.3	63
Ice sample	0.92	2.0	54

### Acknowledgements

We are grateful to Prof. Kunihiko Nishiizumi (Space Sciences Laboratory, University of California, Berkeley, USA) for his detailed advice on ion exchange column method.

### References

- [1] Y. Nagashima, R. Seki, T. Takahashi, D. Arai, Nucl. Instr. Meth. B 172 (2000) 129.
- [2] Y. Nagashima, R. Seki, T. Matsuhiro, T. Takahashi, K. Sasa, K. Sueki, M. Hoshi, S. Fujita, K. Shizuma, H. Hasai, Nucl. Instr. Meth. B 223–224 (2004) 782.
- [3] N.J. Conard, D. Elmore, P.W. Kubik, H.E. Gove, L.E. Tubbs, B.A. Chrunyk, M. Wahlen, Radiocarbon 28 (1986) 556.
- [4] S. Jiang, Y. Lin, H. Zhang, Nucl. Instr. Meth. B 223–224 (2004) 318.
- [5] S. Vogt and U. Herpers, Fresenius Z. Anal. Chem. 331 (1988) 186.

## 4.6 Estimation of thermal neutron fluences in the concrete of various accelerator facilities by $^{36}\text{Cl}$ AMS

K. Bessho<sup>1</sup>, H. Matsumura<sup>1</sup>, T. Miura<sup>1</sup>, K. Masumoto<sup>1</sup>, H. Hagura<sup>1</sup>, Y. Nagashima, R. Seki, T. Takahashi, K. Sasa, K. Sueki, and Y. Tosaki

At accelerator facilities, concrete components around beam lines are exposed to secondary particles during machine operation, and various radionuclides are accumulated in the concrete. Concentrations of the radionuclides induced in the concrete are important for radioactive waste management of accelerator facilities. Thermal neutron fluence irradiated during machine operation is useful information to estimate the radioactivities of the nuclides because most of the radionuclides are mainly produced by thermal neutron-capture reactions. In our previous studies, we have developed a method for AMS of  $^{36}\text{Cl}$  in concrete of accelerator buildings, and demonstrated that the measurements of isotope ratios of  $^{36}\text{Cl}$  to  $^{35}\text{Cl}$  ( $^{36}\text{Cl}/^{35}\text{Cl}$ ) is suitable for monitoring of the thermal neutron fluences [1,2]. The estimation of neutron fluences by using radioactivity generally depends on the relation between half-life of radionuclides and the operational history of accelerator, which is difficult to be exactly clarified. In case of evaluation with the results of  $^{36}\text{Cl}$  AMS, operational histories of accelerators are not indispensable because radioactive decay of  $^{36}\text{Cl}$  can be neglected. Consequently, reliable evaluations of neutron fluences without indefinite assumptions can be attained by  $^{36}\text{Cl}$  AMS.

In this year, thermal neutron fluences at various accelerator facilities was determined, and the characteristics were discussed in correlations with accelerated energy and particles.

Thermal neutron fluence ( $\Phi$ ) was determined by

$$\Phi = (^{36}\text{Cl}/^{35}\text{Cl}) / \sigma ,$$

where the cross section for the  $^{35}\text{Cl}(n, \gamma)^{36}\text{Cl}$  reaction ( $\sigma$ ) was 43.6 barn [3].

Figure 1(a) shows thermal neutron fluences at five kinds of proton accelerators. Acceleration energies of protons are ranging from 17 MeV to 12 GeV. At proton accelerators, secondary neutrons were induced by beam-loss at magnets, beam ducts and irradiated targets. Initially-emitted secondary neutrons consist of various energy neutrons ranging from thermal energy to acceleration energy of the particles, and the energies of secondary neutrons highly depend on the acceleration energies of protons and direction of neutron emissions. These neutrons had continuously irradiated on the concrete walls, floors and shieldings, and induced radionuclides in the concrete. Although contribution of high-energy neutrons is higher at the concrete surface, fast neutrons were partially slowed-down inside concrete, and they finally turns to thermal neutrons. Thermal neutron fluences in Fig.1(a) include penetration of thermal neutrons from concrete surface and formation of thermal neutrons inside concrete. As a result, the maxima in thermal neutron fluences were observed at approximately 5 to 15 cm in the depth, according to the acceleration energies.

The maximum positions in the thermal neutron fluences shift to deeper positions accompanied by

---

<sup>1</sup>High Energy Accelerator Research Organization

increasing acceleration energies in the range of 17 to 65 MeV. Further at high-energy accelerators that accelerate 400 MeV and 12 GeV protons, secondary neutrons reach deeper into the concrete and thermal neutrons populate at deep in the concrete compared to those of the several tens of MeV cyclotrons. These characteristics may reflect the differences in the energy spectra of the secondary neutrons.

At electron accelerator facilities, photo-neutrons populated at beam-loss points and thermal neutrons were found to be main source for activation of the concrete. Figure 1(b) shows thermal neutron fluences in the concrete at three kinds of electron accelerator facilities. The 45 MeV electron LINAC at Hokkaido University also had been utilized to produce pulsed cold-neutrons, and neutrons generated at the source-target were slowed-down inside the carbon moderator before arriving at the concrete walls. As contribution of fast neutrons at the concrete surface was less at this facility, the build-up in thermal neutron fluence was absent. At both of the 220 MeV electron LINAC and the 1.3 GeV electron synchrotron, build-up effects were observed at depths around 10 cm, as shown in the profiles in Fig. 1(a). Further, attenuation lengths of thermal neutrons were similar at three kinds of accelerators, and it implied the similarity in energies of photo-neutrons induced by wide energy-range electrons. Similarity in neutron energy is contrastive to highly dependence of neutron energy on acceleration energy at proton accelerators.

Further quantitative analysis on the neutron distribution in the concrete is now in progress, and it will be valuable for radioactive waste management in decommissioning of accelerator facilities.

## References

- [1] K. Bessho et al., Radiochim. Acta, accepted
- [2] K. Bessho et al., Nucl. Instr. Meth. B, accepted
- [3] R.B. Firestone, V.S. Shirley ed., Table of Isotopes, 8th ed., Wiley-Interscience, New York 1996.

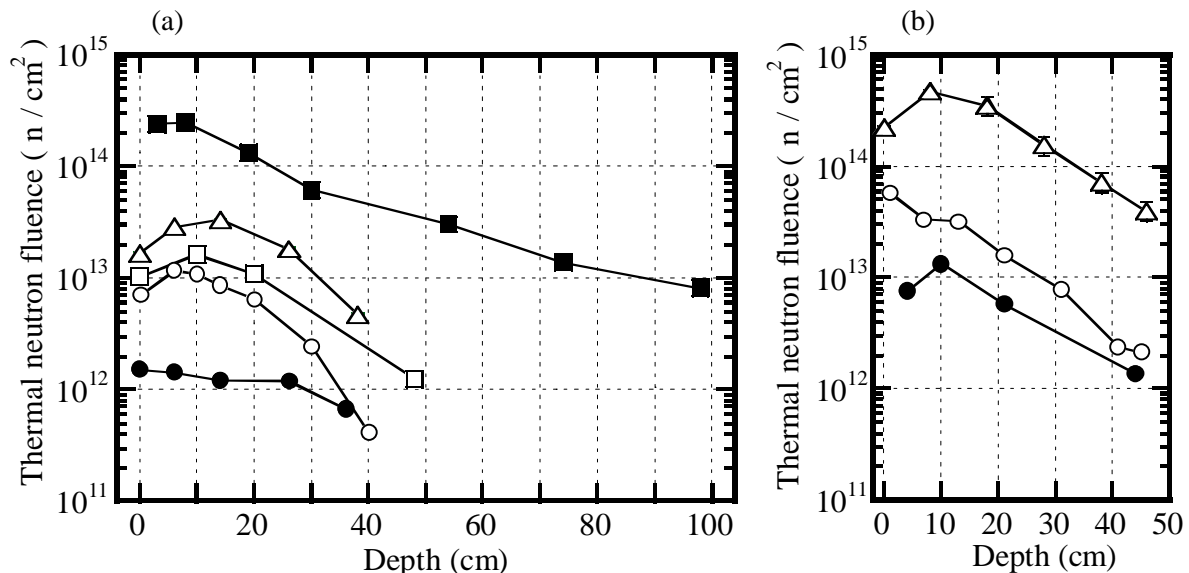


**Fig. 1** Thermal neutron fluences estimated with  $^{36}\text{Cl} / ^{35}\text{Cl}$ .

- (a) Proton accelerator facilities : 17 MeV (small cyclotron at NMCC) (○), 45 MeV (SF cyclotron at CNS, the Univ. of Tokyo) (□), 65 MeV (AVF cyclotron at RCNP, Osaka Univ.) (Δ), 400 MeV (RING cyclotron at RCNP, Osaka University) (●), 12 GeV (proton synchrotron at KEK) (■).
- (b) Electron accelerator facilities : 45 MeV (electron LINAC at Hokkaido Univ.) (○), 220 MeV (electron LINAC at LNS, Tohoku Univ.) (Δ), 1.3 GeV (electron synchrotron at Tanashi branch, KEK) (●).

## 4.7 Low Z element analysis of the Cr target deposited by HIVIPP method using a 1.8 MeV He<sup>+</sup> beam of Tandetron accelerator

I. Sugai<sup>1</sup>, Y. Takeda<sup>1</sup>, M. Oyaizu<sup>2</sup>, H. Kawakami<sup>2</sup>, K. Sasa, Ishii, and K. Shima

Recently, we have developed a new deposition method of HIVIPP (HIgh energy Vibrational Powder Plating), which is based on the high energy vibrational motion of powders in the electrostatic field between parallel electrodes [1-2]. This method has been found to be very useful as a target preparation technique in both backed and unbacked conditions. This is very simple method. The deposition process has been performed at room temperature in vacuum. The deposition process could be further simplified if it could be operated without a vacuum pumping system. The deposition is to operate at higher than one atmospheric pressure in inert or reactive gases. By this process, new materials could be synthesized when used the reactive gas. With motivation of this new material systemization, we have tried target deposition at high pressure of air gas. Elemental compositions of the deposited targets were measured using the 1.0 MV Tandetron accelerator of Tsukuba University.

The experimental apparatus for target deposition is same as that described in the paper [1-2]. The high pressure container is composing of an acryl tube of 20 mm thick. The size of the container is 25 cm in diameter and 35 cm in high. Deposition apparatus is very simple, composing of two parallel metallic disks of 2.5 cm diameter and 0.5 mm thick. The disks (substrate) play as electrodes and hold the backing plate. The distance between two electrodes is 10 mm, and the glass ring tube with 2.5 cm diameter is inserted between the disks.

High purity metallic Cr powder with about 100 μm in particle size was used as material to be deposited. Dried air was used as reactive gas. Two copper plates of 0.3 mm thick were used as backing plate. The sample of the Cr powder about 50 mg was inserted on the cathode electrode. High pressure air was inserted into the container up to  $3 \times 10^5$  Pa. The applied DC high voltage was increased very gradually, in 200 V steps every 5 min. watching the powder behavior. The powders began to vibrate at 2.5 kV. When the voltage was increased to 18 kV, the current charged suddenly from 10 to 70 μA. About 1h was required at 25 kV to obtain a deposition of 85 μg/cm<sup>2</sup> thickness. After the high voltage was switched off, the high pressure gas was ejected to one atmosphere and the electrodes could immediately be removed and handled. Deposited thicknesses were measured using an electronic ultra microbalance.

The surfaces of the Cr targets deposited onto the both copper plates showed not metallic color but deep navy blue color. In order to investigate the color change of the Cr deposited target, we performed the elemental analysis of the Cr target by taking the Rutherford Back Scattering (RBS) and Particle Induced

---

<sup>1</sup>Accelerator Research Laboratory, <sup>2</sup>Institute of Particle and Nuclear Study, High Energy Accelerator Research Organization

X-ray Emission (PIXE) spectrum using a 1.8 MeV He<sup>+</sup> tandem (Tandatron) accelerator at University of Tsukuba. The measurement was to detect the level of element carbon, nitrogen and oxygen in the deep navy blue color Cr target, which is considered to be synthesized with air. The light and other heavy elements of Si, Cr and Cu were detected with a 1.8 MeV He<sup>+</sup> beam from the accelerator and particles scattered at =160° with SSD by RBS and PIXE. For a comparison, we also analyzed a commercially available (CM) Cr foil (1.0 mg/cm<sup>2</sup>) and Cr target (~ 120 μg/cm<sup>2</sup>) made by the same HIVIPP method in vacuum. Figures 1 and 2 show the obtained spectra of RBS and PIXE. As can be seen, we can clearly see Cr peak from the 3 targets and the Si peak was also detected except for the CM Cr foil and Cr target made in high pressure. Si peak is from a diffusion pump oil of the HIVIPP deposition in the vacuum apparatus. However, we can not detect any low Z elements of the <sup>12</sup>C, <sup>14</sup>N and <sup>16</sup>O.

Although the color Cr prepared in 3 × 10<sup>5</sup> Pa high pressure of air showed deep navy blue color, the detection of these low Z of the C, N and O elements in this target at first experiment was impossible. Hence, in next experimental measurement, we will try to detect low Z elements very small amount in the targets by using an X-ray detector with a super ultra thin polymer.

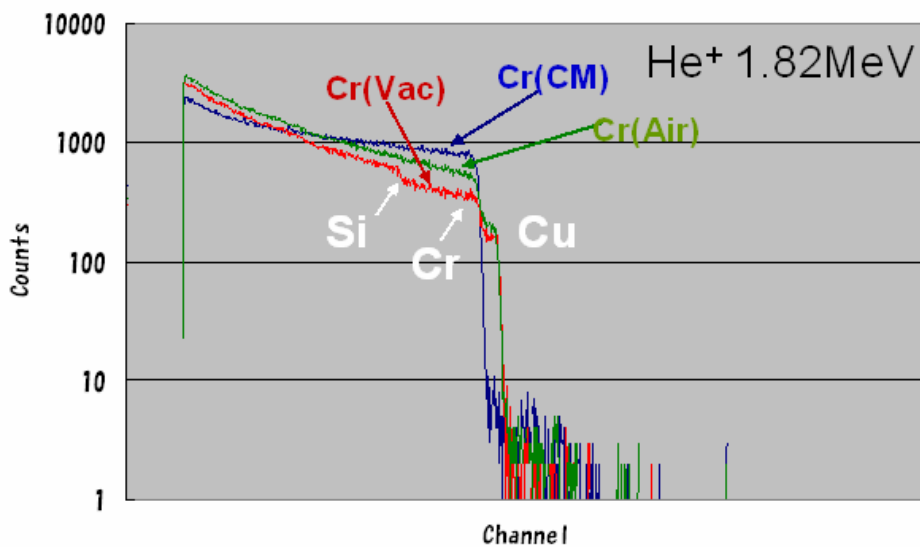


Fig.1

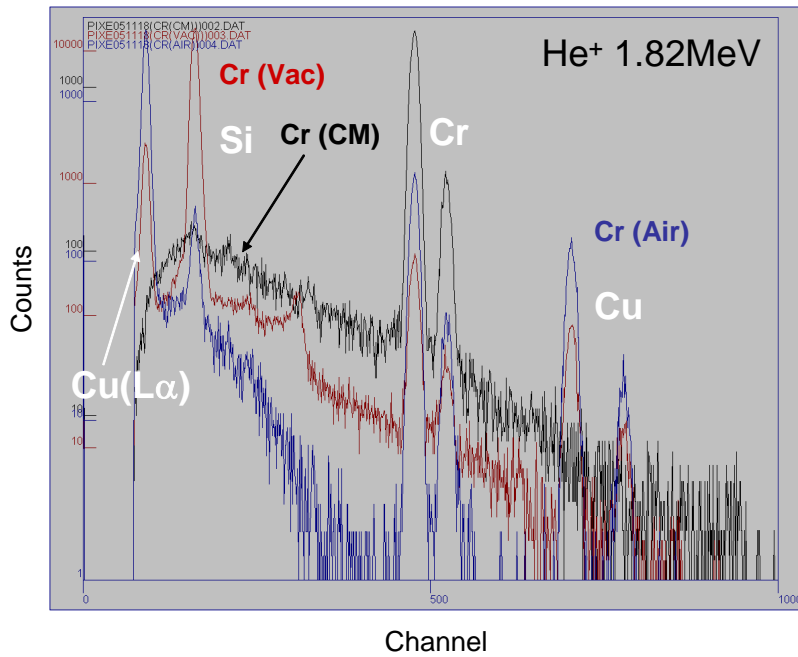


Fig.2

Fig.1 and 2 Elemental analysis of Cr targets made by HIVIP method in vacuum and in air high pressure of  $3 \times 10^5$  Pa and Cr foil of CM. The spectra were obtained by RBS and PIXE with a 1.8 MeV  $\text{He}^+$  ions from Tandetron accelerator of Tsukuba University.

#### References

- [1] I. Sugai, Nucl. Instr. and Meth. A397(1997) 81.
- [2] I.Sugai, Nucl. Instr. and Meth.A438(1999) 58.

## 4.8 Imaging of iodinated contrast medium using proton-induced quasi-monochromatic X-ray emission

J. Hasegawa<sup>1</sup>, J. Kaneko<sup>1</sup>, Y. Oguri<sup>1</sup>, and K. Sasa

Until now, many research groups have investigated high contrast angiography using monochromatic X-rays from synchrotron radiation facilities[1-3]. They obtained high contrast images of iodine contrast medium in vessels by adjusting the energy of the monochromatic X-rays to the value just above the iodine K-edge energy. On the other hand, proton-induced X-rays have the potential to be used as quasi-monochromatic X-ray sources because the characteristic X-rays are dominant in the energy spectra. In the previous experiments we applied the proton-induced X-rays to high contrast imaging of ruthenium contrast medium[4]. By choosing the target material that has the KX-ray energy just above the ruthenium K-edge energy, we successfully obtained high contrast images of the ruthenium contrast medium in a small phantom. However, because of the limitation of the maximum proton energy, imaging of iodine contrast medium, which is widely used in clinical practices, was impossible in the previous experiments. Then we carried out an experiment on high contrast imaging of the iodine contrast medium using a higher-energy proton beam supplied from 12 UD Pelletron Tandem Accelerator at UTTAC.

Figure 1 shows the experimental setup. We used thick metallic targets of tin (Sn) and lanthanum (La). A 7-MeV proton beam from the Tandem Accelerator was focused onto the target with a spot size of  $1 \times 2 \text{ mm}^2$ . The beam current was 40–80 nA. The X-rays emitted from the target were extracted through a 60- $\mu\text{m}$ -thick,  $\phi 30\text{-mm}$  Mylar window. For detection of the X-rays passing through a Lucite phantom, we used an imaging plate with a size of  $30 \times 50 \text{ mm}^2$ . An aluminum plate of 100  $\mu\text{m}$  thick was located just in front of the imaging plate to attenuate LX-rays from the targets. After an exposure of 15–30 minutes, the transmission image recorded on the imaging plate was read out by a compact digital X-ray imaging system. A CdTe detector monitored the energy spectra and the irradiation doses of X-rays in parallel with the exposure.

We used two types of Lucite phantoms for the present experiment as illustrated in Fig. 2. One of them was a rectangular solid, which has seven parallel  $\phi 1\text{-mm}$  holes and three parallel  $\phi 3\text{-mm}$  holes. The  $\phi 1\text{-mm}$  holes contained iodinated potassium solution with various iodine concentrations: 1000, 500, 200, 100, 50, 10, and 0 mg/cc (water). To imitate bone structures in the body, calcium-hydrogen-phosphate powder, which was prepared by pounding calcium tablets, was filled in one of the  $\phi 3\text{-mm}$  holes. Both the weight percentage of calcium and the mass density of the imitated bone were almost the same as those of

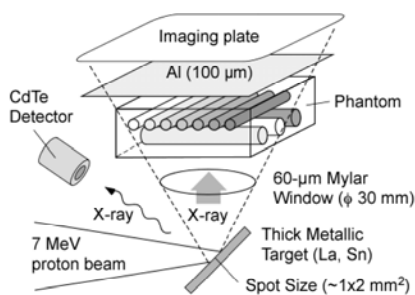


Fig. 1. Experimental setup.

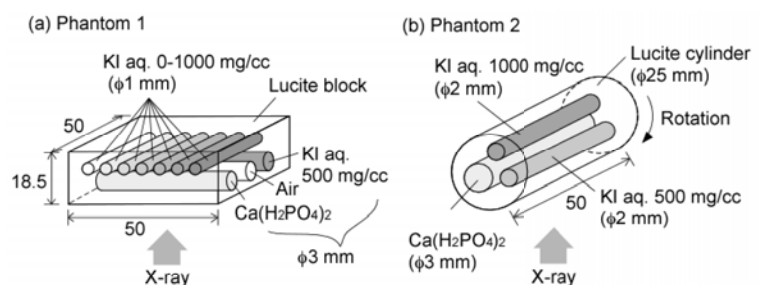


Fig. 2. Schematic illustrations of phantoms.

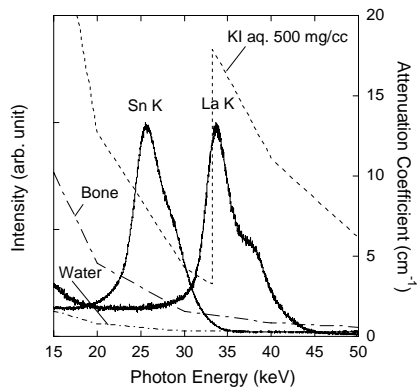
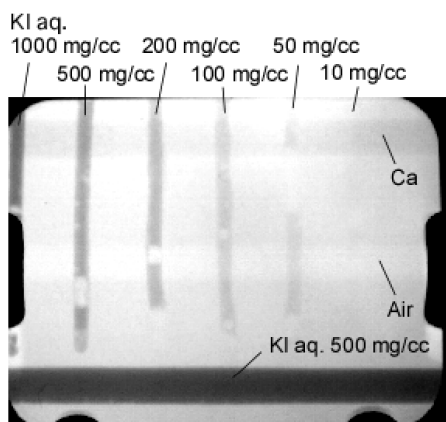
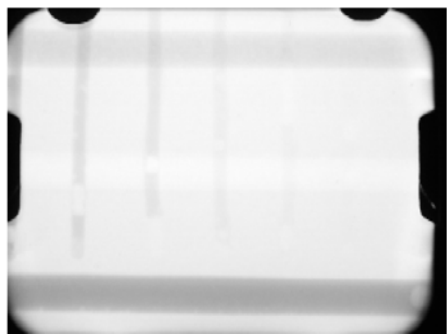


Fig. 3. X-ray energy spectra and attenuation coefficient of iodine contrast medium, bone, and water.



(a) with La target



(b) with Sn target



(c) after dual-energy subtraction

Fig. 4. Transmission images of phantom 1 with (a) La target, (b) Sn target, and (c) image after dual-energy subtraction.

bones in the human body. The other two  $\phi 3$ -mm holes contained an iodinated potassium solution (500 mg/cc) and air, respectively. Another phantom was a 50-mm-long,  $\phi 25$ -mm cylinder, aimed for computed tomography using quasi-monochromatic X-rays. This phantom had two  $\phi 2$ -mm holes containing iodinated potassium solutions with iodine concentrations of 1000 and 500 mg/cc. An imitated bone structure ( $\phi 3$  mm) was also prepared.

Figure 3 shows the energy spectra of Sn and La KX-rays and the attenuation coefficients of the iodinated potassium solution with an iodine concentration of 500 mg/cc, bone, and water. From the La target quasi-monochromatic X-rays with a peak energy of 33.2 keV were obtained, which is just above the iodine K-edge energy. Because of the low energy resolution of the CdTe detector, the peaks of  $K_{\alpha}$  and  $K_{\beta}$  X-ray emissions were convolved with each other. The X-ray emission from the Sn target was also dominated by the characteristic X-rays.

Typical transmission images of the phantom 1 are shown in Fig. 4. Thanks to the strong absorption of La KX-ray by the iodine contrast medium, the contrast of the image taken with the La target was much higher than that with the Sn target. The contrast medium even with an iodine density of 50 mg/cc, which is much lower than those in clinical practices, could be recognized in the image with the La target. In Fig. 4(a) and (b), shadows of the bone (Ca) and the void (air) structures are still visible. By using the dual-energy subtraction method, we could completely remove the shadows of the bone structures as shown in Fig. 4(c), which indicates that the proton-induced X-rays used in the present experiment were enough monochromatic to perform high-contrast imaging.

## References

- [1] R. Lewis, *Phys. Med. Biol.*, 42 (1997) 1213.
- [2] K. Umetani, *et al*, *J. Synchrotron Rad.*, 5 (1998) 1130.
- [3] H. Mori, *et al*, *Radiology*, 201 (1996) 173.
- [4] S. Iwatani, *et al*, *Sci. and Technol. of Adv. Mat.* 5 (2004) 597.

<sup>1</sup>Research Laboratory for Nuclear Reactors, Tokyo Institute of Technology.

## 4.9 Nanoscale and high aspect ratio patterns on SiO<sub>2</sub> and TiO<sub>2</sub> created with fast heavy ions

Koichi Awazu<sup>1,2</sup>, Xiaomin Wang<sup>1</sup>, Makoto Fujimaki<sup>1,3</sup>, Tetsuro Komatsubara, Hirotaka Ikeda<sup>3</sup>, Yoshimichi Ohki<sup>3</sup>

1. Center for Applied Near-Field Optics Research, National Institute of Advanced Industrial Science and Technology (AIST), 1-1-1 Higashi, Tsukuba 305-8562, Japan

2. Department of Engineering Synthesis, School of Engineering, The University of Tokyo, 7-3-1 Hongo, Bunkyo-ku, Tokyo 113-8656, Japan

3. Department of Electrical Engineering and Bioscience, Waseda University, 3-4-1 Ohkubo, Shinjuku-ku, Tokyo 169-8555, Japan

A latent track is created by the passage of an atomic particle through dielectric materials. The presence of tracks is normally revealed after etching the tracks in a suitable liquid. It has been widely examined in many fields such as nuclear physics and material science because holes with uniform diameter and high aspect ratio (i.e., length much greater than diameter) can be obtained without mask.

It is natural that many researchers would stimulate to think of practical applications of the nuclear track technique. Many fascinating topics have also been appeared. For example, nuclear pore filters widely used by microbiologist have been manufactured by irradiating a thin polycarbonate sheet with roughly collimated fission fragments and etching to the desired pore size. Nanowires can serve as field emission display. Lindeberg and Hjort have developed magneto-resistive sensors of sub-millimeter size and 3D nanowire circuits. All works were based on etched tracks in polymers such as polycarbonate. It is desired to create high aspect ratio holes in inorganic materials (e.g., silica glass). Because silica glass is thermally stable, mechanically strong, and one of the least chemically reactive materials, fine filters made from silica glass would be useful in a much broader range of environments than polycarbonate filters.

The authors have examined structure of the latent track in silica glass. Maximum of length/diameter ratio of was up to 5 with liquid hydrofluoric acid. Lately, Musket and co-workers have developed vapor etching technique.[1] Holes with diameter of ~24 to 80nm have been documented with length/diameter ratio of up to 22. Generally, the shape of the etched hole is not cylindrical, but conical with the largest diameter being near the surface. This is a consequence of the etching rate in the latent tracks  $V_T$  being comparable to the general etching rate  $V_G$  in the track-free regions. A near cylindrical hole results when the etching rate in the latent track is very high compared to the general attack. An typical example of such material is titanium dioxide of rutile single crystal. The goal of our work is to create uniform nano size holes with high ratio of length/diameter of silica and titania in order to use as nuclear pore filters to separate molecular-sized materials. Especially, titania with nuclear pore would be useful as photo-catalysis filters.

Figure 1 shows high resolution transmission electron micrograph of a sample irradiated with 50 MeV Br<sup>8+</sup> (a-1) followed by 20% hydrofluoric acid etching for 10 s (a-2). Hereafter, 1 and 2 in ([letter]-1 and [letter]-2) denote before and after etching, respectively. (b) 115 MeV Br<sup>11+</sup>, (c) 120 MeV I<sup>11+</sup>, (d) 150 MeV

$\text{Au}^{14+}$ . All scale bars indicate 2nm. In Figure 1, the first-order feature is that damaged zones of milky color assigned to amorphous and stressed lattice around amorphous part can be seen. The densities of rutile and amorphous  $\text{TiO}_2$  have been reported as being  $4.25 \text{ g/cm}^3$  and  $2.4\text{--}3.4 \text{ g/cm}^3$ , respectively.[2] It is possible that the transformation from the rutile phase to the amorphous phase caused volume expansion which led to lattice stress. In fact, swelling of the damaged zone deduced from volume expansion was observed in AFM images.

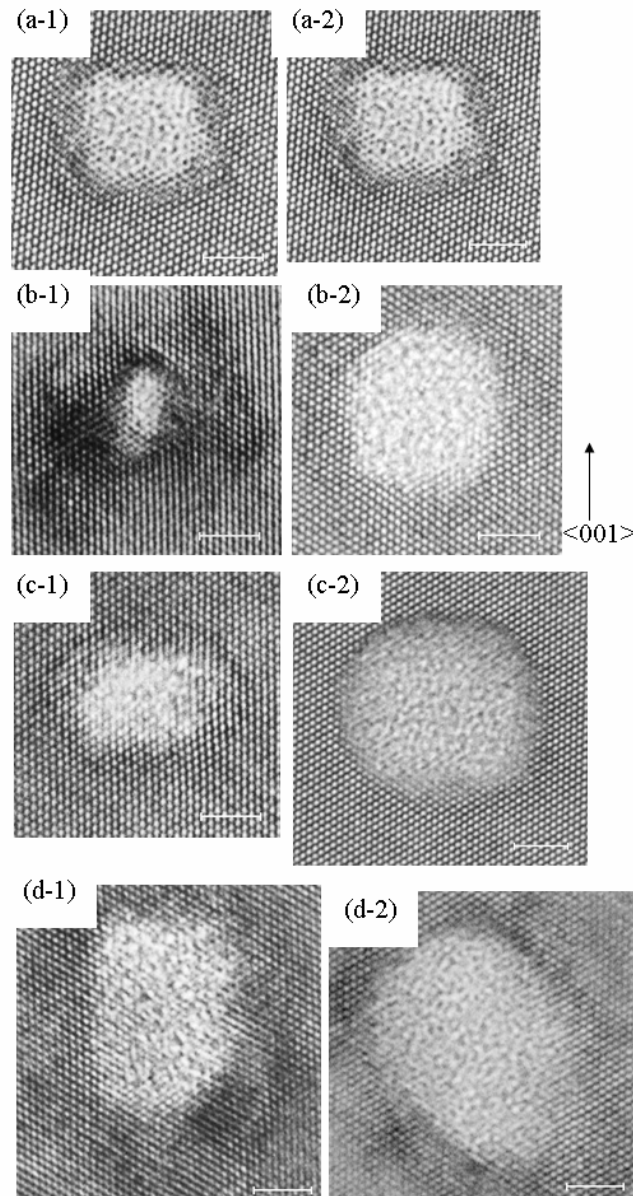


Fig.1.TEM observation of  $\text{TiO}_2$  rutile single oxide before and after acid etching

## References

- [1] R.G.Musket, J.M.Yoshiyama, R.J.Contolini, J.D.Porter, J.Appl.Phys., 91 (2002) 5760.
- [2] D. Mergel, Thin Solid Films, 397 (2001) 216.

## 4.10 New detection system of ERCS hydrogen analysis

T. Komatsubara, K. Sasa, M. Kurosawa, S. Ishii, Y. Yamato, T. Kawamata, K. Iwamura, H. Okaguchi, M. Furukawa

In our micro beam facility with 20 MeV proton ions, basic studies of hydrogen analysis using elastic recoil coincidence spectrometry (ERCS) are in progress. Developments of the detection system and an analysis method have been carried out to improve the accuracy of the hydrogen determination.

### 1) New detector system

Asymmetric detector apertures have been introduced for the sake of better stability of the coincidence yield. Diameter of the right aperture is 8 mm while the left one is 12 mm. Measured yields by changing  $z$  position are shown in Fig. 1. In this figure open squares show for the asymmetric window. The yields are stabilized using the asymmetric collimator system.

A detector folding table was newly designed so as to adjust detector position using six screws for xyz-three-directions as shown in Fig. 2. Alignment of the detectors was performed within several tens micro meters.

### 2) New analysis method

Fig. 3(a) shows a 2 dimensional spectrum using a stack target consisting of five Mylar films and four glass plates. The measured five lines correspond to the hydrogen in Mylar films. These lines appear as bended curves, since the stopping energy depends on the scattering angle. In our study of the spectra, the curves were found to be parabola;

$$X = E_1 - E_2, \quad Y = E_1 + E_2 - E_{sum}, \quad Y = -\alpha X^2. \quad (1)$$

The parameter  $\alpha$  was found to be a simple function of  $E_{sum}$  as follows where two parameters  $k_0 = 0.114 \text{ MeV}^{-1}$  and  $k_1 = -0.006 \text{ MeV}^{-2}$  are introduced;

$$\alpha = k_0 + k_1 \cdot E_{sum}. \quad (2)$$

For a measured point  $(E_1, E_2)$  corresponding  $E_{sum}$  for the symmetry scattering can be calculated as

$$E_{sum} = \frac{E_1 + E_2 + k_0 \cdot (E_1 - E_2)^2}{1 - k_1 \cdot (E_1 - E_2)^2}. \quad (3)$$

The position  $(E_1, E_2)$  in the 2-dimensional spectrum is modified to  $(E'_1, E'_2)$  as

$$E'_1 = E_1 + \frac{1}{2}(E_{sum} - E_1 - E_2), \quad E'_2 = E_2 + \frac{1}{2}(E_{sum} - E_1 - E_2). \quad (4)$$

Using these formula the 2-dimensional plot is modified as Fig. 3(b). The bending curves are corrected to straight lines.

### 3) Depth resolution

For the hydrogen depth profiling, depth resolution is one of the important parameters. Detection resolutions were measured by changing bombarding energy of proton beam as shown in Table 1. For the irradiation targets, thin layers of Formvar were prepared as coating on both surfaces of a 10  $\mu\text{m}$  anhydrous glass plate. Thickness of the Formvar was measured to be  $13 \pm 3 \mu\text{m}/\text{cm}^2$ .

As a result of the experiments, it has been turned out that the depth resolution strongly depends on the beam energy. When the beam energy decreases, the resolution becomes small. However, total thickness of the irradiation target should be thinner for the low energy measurement. Our result is consistent to the previous report[1].

### 4) Calibration

In order to determine an accuracy and a precision of the hydrogen analysis, calibration measurements were carried out using Mylar, Kapton, Polyethylene, Ti(H) and PL-01. The PL-01 film is a kind of Polyimide which was provided by NTT Advanced Technology Corporation.

Hydrogen weight densities determined using ERCS are compared with those by CHN elemental analyzer (Perkin-Elmer 2400). The certificated value by NIST[2] is also compared for Ti(H). As a result of the measurement systematic error of ERCS analysis was evaluated as 3 %. When Mylar films are used as supporting films and as standard material, deviation of hydrogen content in one Mylar film is dominant to determine the precision of the analysis. The standard deviation of hydrogen content in one Mylar film was measured to be 3 %. Total deviation of the hydrogen analysis using ERCS can be determine less than 5 %.

### Acknowledgement

NTT Advanced Technology Corporation is deeply acknowledged for their free samples of Polyimide films.

### Reference

[1] Wegden, *et al.*, NIM B231 (2005) 524-529

[2] National Institute of Standards & Technology, Certificate of Analysis, Standard Reference Material 352c, Hydrogen in Unalloyed Titanium, Hydrogen Concentration:  $49.0 \pm 0.9 \mu\text{g/g}$

Table 1 Measured results of ERCS resolutions. The Mylar target is a self-support film of 2.5  $\mu\text{m}$  thickness. The Formvar target is coating on 10  $\mu\text{m}$  anhydrous glass.

Beam energy [MeV]	FWHM [keV]	FWHM [ $\mu\text{m}$ ]	target
4	54	0.85	Formvar
6	70	1.5	Formvar
12	120	4.4	Mylar
15	140	6.0	Mylar
20	170	9.2	Mylar

Table 2 Calibration of hydrogen contents.

Material (thickness)	surface density [mg/cm <sup>2</sup> ] (relative error)	reference of hydrogen [wt.%] (relative error)	ERCS analysis [wt.%] (relative error)
Mylar (2.5μm)	0.348 ± 0.006 (1.7%)	4.49 ± 0.06 (1.3%)	4.49 (reference) (3.7%)
Kapton (7.5μm)	1.085 ± 0.027 (2.5%)	2.88 ± 0.03 (1.0%)	2.84 ± 0.10 (3.3%)
Polyethylene (30μm)	2.43 ± 0.06 (2.5%)	14.0 ± 0.2 (1.4%)	13.7 ± 0.3 (2.0%)
FL-01 (2.5μm)	3.610 ± 0.075 (2.1%)	1.81 ± 0.05 (2.7%)	1.80 ± 0.05 (2.7%)
Ti(H) (113μm)	51.5 ± 2.6 (5.0%)	0.00490 ± 0.00009 (1.8%)	0.0049 ± 0.0001 (2.0%)

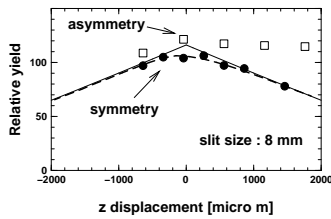


Fig. 1. Coincidence yields as functions of z position. Open squares show for the asymmetric window system, while closed circles for the symmetric window. Calculations for the symmetric cases are also shown by solid and dashed lines.

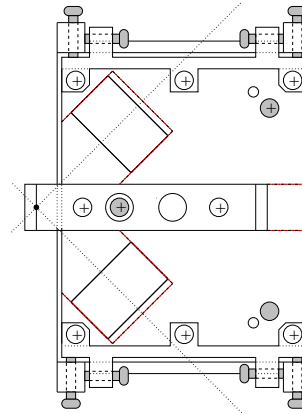


Fig. 2. Newly designed detector table. Adjusting bolts are shown by gray color for xyz-three-directions.

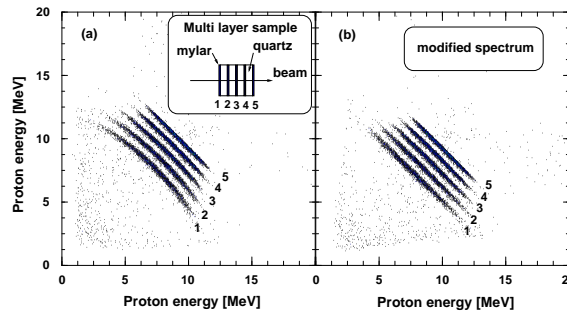


Fig. 3. ERCS 2-dimensional spectra. 3(a) shows raw data, and 3(b) is modified spectrum using the method described in text.



**5.**

**TECHNICAL REPORT**



## 5.1 New data acquisition system using CC/7700

H. Kimura, T. Komatsubara

A PC based data acquisition system has been developed by using TOYO CC/7700 parallel crate controller, where FreeBSD 6.0-RELEASE is employed as the host operating system.

Software of this system consists of device driver, main process and GUI process. Main feature of the device driver is handing interrupt generated by CC7700 and executes CAMAC command list that preloaded by user demand. User can upload a CAMAC command list for individual LAMs. If the list contains CAMAC read functions, data are buffered in the driver, and transferred to the main process.

The main process controls the system. There are no preferred acquisition routines in this system. User should write their callback routines to initialize CAMAC modules which include start and stop functions and event processor. At startup time, the main process compiles user routines and links it to itself. User may write routines in two languages, C and CAMAC. For example, Fig. 1 shows user code to read and process two channels of data from CAMAC ADC with self trigger. After loading these codes the main process executes "init:" section in the CAMAC file, then executes "init()" routine in the C file. The "LAM1:" section in the CAMAC file is the interrupt routine to read event data. That code will be compiled and uploaded to the driver.

```
/* test1.c */
#include "daqlib.h"
int ch0, ch1;

int init () {
    /* allocate histograms */
    ch0 = hist_new1("ch0", 2048);
    ch1 = hist_new1("ch1", 2048);
    return OK;
}

/* process event data */
int event (int data[], int n){
    hist_add1(ch0, data[0]&0xffff);
    hist_add1(ch1, data[1]&0xffff);
    return OK;
}

/* test1.camac */
#define ADC N1
init: /* reset ADC */
      ADC, F9, A0

run: /* enable LAM */
     ADC, F26, A0

stop: /* disable LAM */
      ADC, F24, A0

LAM1: /* read data then reset */
      ADC, F0, A0
      ADC, F0, A1
      ADC, F9, A0
```

Fig. 1. User code for CAMAC ADC

The GUI process is the user interface of this system, as shown in Fig. 2. There are four user defined buttons (button1, button2, button3, button4) and four input boxes (shown as 100,500,100,500). Each element is connected to user callback routines. For example, if the button labeled by "button1" is pressed, the main process executes the "button1:" section of a CAMAC file and "button1()" routine in a C file.

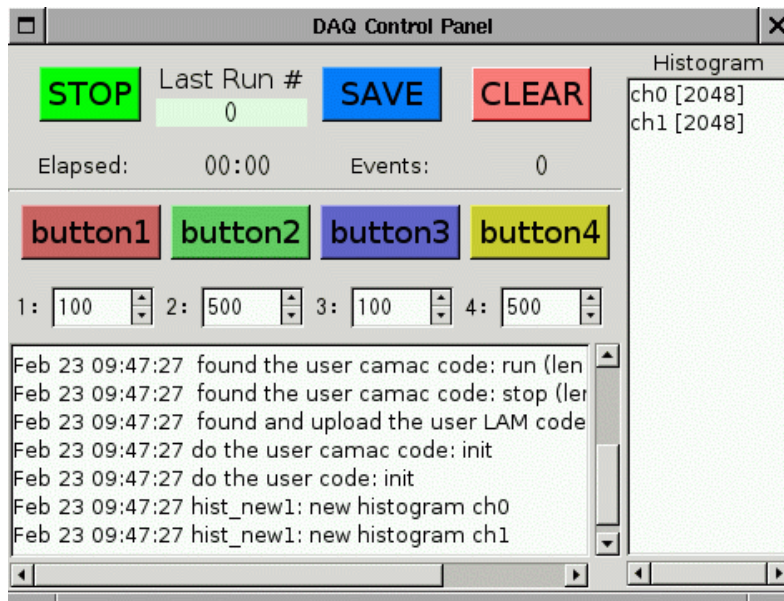


Fig.2. The GUI of the system

CC7700 is a cheap but not a fast controller. One CAMAC read/write function needs about 6 micro seconds and a control function needs about 4 micro seconds. In order to evaluate the dead time of the data acquisition, three methods have been developed as numeric calculation, timer counter and trigger counter.

**6.**

**RELATED TOPICS**



## 6.1 Highly-concentrative immobilization of an enzyme only on a small sensitive area and its effect on sensor performance

M. Hashimoto, N. Sakamoto and H. Suzuki

### 1. INTRODUCTION

Over the last decade, there has been a marked progress in the  $\mu$ TAS or Lab-on-a-Chip technology. Among various devices, electrochemical microsystems are very promising in their application to micro health-care systems. We have been focusing our attention to highly sensitive, efficient detection of a very small amount of analyte on the basis of amperometric detection in a micro flow channel. Along with structural and conditional parameters of the system [1], improvement in the performance of the sensor itself is a critical issue, which was a major theme of this study. We have already developed a method to concentrate materials in a droplet of a solution only on a sensitive area using a super-hydrophobic surface [2]. In this study, we used this technique to form a highly active enzyme layer only on the sensitive area. The details of the technique and the performance of sensors fabricated by this method in a solution in a beaker or a micro flow channel will be reported.

### 2. EXPERIMENTAL

#### Fabrication of the device

Electrodes were formed on a glass substrate. For batch-style measurements, only a working electrode was prepared, and a commercial reference electrode and a platinum auxiliary electrode were used.

In immobilizing an enzyme by evaporative concentration, a dry-film photoresist layer was additionally formed on the polyimide layer. A super-hydrophobic layer was formed in an area other than the sensitive area by depositing polytetrafluoroethylene (PTFE) beads (diameter: 1  $\mu$ m). The sensitive area was protected with a PDMS cylinder. In depositing the PTFE beads, they were floated on distilled-deionized water. The thin layer of beads was carefully transferred to the surface of the chip. After drying at room temperature, the PDMS cylinder was removed. As a result, a super-hydrophobic layer was formed in the area that surrounded the sensitive area. To immobilize the enzyme, a solution containing glucose oxidase, bovine serum albumin, and glutaraldehyde was placed on the sensitive area. The solution was repelled from the surrounding super-hydrophobic area (Fig. 1(a)). The enzyme solution was then concentrated by evaporation. The droplet finally shrank to the sensitive area and an enzyme-immobilized layer was formed only on the sensitive area (Fig. 1(b)). After the immobilization of the enzyme, the dry-film photoresist was peeled off along with the PTFE beads (Fig. 1(c)).

#### Measurement procedure

For batch-style measurements, an aliquot of a 1 mM glucose standard solution was injected into a 0.1 M phosphate buffer solution containing 0.1 M KCl (pH 7.4). The solution was stirred for 10 s and the measurements were taken in a quiescent solution. In conducting the experiments using the micro flow channel a standard solution was injected by using a micro syringe pump at a fixed flow rate. The potential of the working electrode was poised at + 0.7 V (vs. Ag/AgCl).

### 3. RESULTS

Fig. 2 compares the calibration plots obtained using sensors fabricated by the novel method and the conventional method. The amount of the enzyme was the same for both cases. When the enzyme was immobilized by the conventional method, the behavior of the output current was basically the same as that reported in numerous papers. The calibration plot was linear up to approximately 1 mM and the dependence became weaker at higher concentrations. When the enzyme was immobilized by the novel method, a significant increase in the output current was observed and the linear region extended to higher concentrations. This suggests that the diffusion of glucose and oxygen (particularly the latter) was enhanced.

The effect of the size of the electrode area was examined by changing the diameter of the electrode between 0.3 and 1 mm. Although the current increased as the size of the electrode area increased, the current density was higher with smaller electrodes.

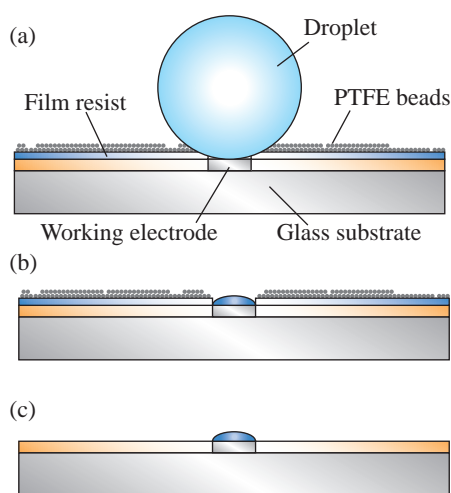


Fig. 1. Evaporative concentration using a super-hydrophobic surface. (a): Droplet placed on a hydrophilic sensitive area surrounded by a super-hydrophobic layer. (b): Droplet shrunk after evaporation. (c): Enzyme-immobilized layer after the thick-film photoresist was peeled off along with the PTFE beads.

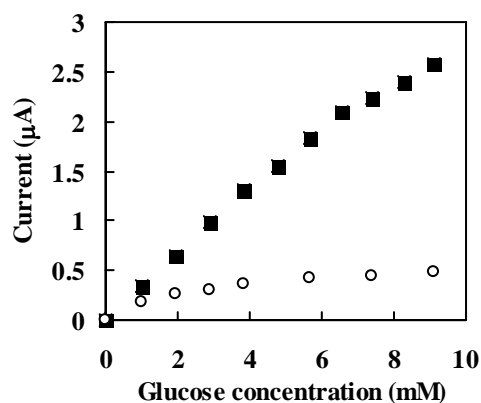


Figure 2. Comparison between the novel method and the conventional method. Working electrode diameter: 1 mm. Enzyme was immobilized by the novel method (■) and the conventional method (○).

### References

- [1] M. Hashimoto, S. Upadhyay, H. Suzuki, "Dependence of the response of an amperometric biosensor formed in a micro flow channel on structural and conditional parameters", *Biosensors and Bioelectronics*, in press.
- [2] I. Yanagimachi, N. Nashida, K. Iwasa, H. Suzuki, "Enhancement of the sensitivity of electrochemical stripping analysis by evaporative concentration using a super-hydrophobic surface", *Science and Technology of Advanced Materials*, vol. 6, pp. 671-677, 2005.

## 7. LIST OF PUBLICATIONS

The publications listed here are those released in the fiscal year 2005 by all the workers listed on §11.

### 7.1 Journals

#### NUCLEAR PHYSICS

1. C. Wu, Y.Yamaguchi, A.Ozawa, I.Tanihata, D.Jiang, H.Hua, T.Zheng, Z.Li and Y.Ye, Neutron removal reactions of  $^{17}\text{C}$ , *J. Phys. G: Nucl. Phys.* **31** 39-47 (2005).
2. Y.L.Ye, D.Y.Pang, D.X.Jiang, T.Zheng, Q.J.Wang, Z.H.Li, X.Q.Li, Y.C.Ge, C.Wu, G.L.Zhang, Q.Y.Hu, J.Wang, Z.Q.Chen, A.Ozawa, Y.Yamaguchi, R.Kanungo, and I.Tanihata, Quasielastic scattering of  $^6\text{He}$  on  $^9\text{Be}$  at 25 MeV/nucleon, *Phys. Rev. C* **71**, 014604 (2005).
3. K. Kimura, T. Izumikawa, R. Koyama, T. Ohnishi, T. Ohtsubo, A.Ozawa, W. Shinozaki, T. Suzuki, M. Takahashi, I. Tanihata, T. Yamaguchi, Y. Yamaguchi, High-rate particle identification of high-energy heavy ions using a tilted electrode gas ionization chamber, *Nucl. Instr. and Meth. A* **538**, 608-614 (2005).
4. R.Kanungo, Z.Elekes, H.Baba, Zs.Dombradi, Zs.Fulop, J.Gibelin, A.Horvath, Y.Ichikawa, E.Ideguchi, N.Iwasa, H.Iwasaki, S.Kawai, Y.Kondo, T.Motobayashi, M.Notani, T.Ohnishi, A.Ozawa, H.Sakurai, S.Shimoura, E.Takeshita, S.Takeuchi, I.Tanihata, Y.Togano, C.Wu, Y.Yamaguchi, Y.Yanagisawa, A.Yoshida, K.Yoshida, Excited states in neutron rich boron isotopes, *Phys. Let. B* **608** 206-214 (2005).
5. Z.Elekes, Zs.Dombradi, R.Kanungo, H.Baba, Zs.Fulop, J.Gibelin, A.Horvath, E.Ideguchi, Y.Ichikawa, N.Iwasa, H.Iwasaki, S.Kanno, S.Kawai, Y.Kondo, T.Motobayashi, M.Notani, T.Ohnishi, A.Ozawa, H.Sakurai, S.Shimoura, E.Takeshita, S.Takeuchi, I.Tanihata, Y.Togano, C.Wu, Y.Yamaguchi, Y.Yanagisawa, A.Yoshida, K.Yoshida, Low-lying excited states in  $^{17,19}\text{C}$ , *Phys. Let. B* **614** 174-180 (2005).
6. R.Kanungo, Z.Elekes, H.Baba, Zs.Dombradi, Zs.Fulop, J.Gibelin, A.Horvath, Y.Ichikawa, E.Ideguchi, N.Iwasa, H.Iwasaki, S.Kawai, Y.Kondo, T.Motobayashi, M.Notani, T.Ohnishi, A.Ozawa, H.Sakurai, S.Shimoura, E.Takeshita, S.Takeuchi, I.Tanihata, Y.Togano, C.Wu, Y.Yamaguchi, Y.Yanagisawa, A.Yoshida, K.Yoshida, Search for an isomeric state in  $^{19}\text{C}$ , *Nucl. Phys. A* **757** 315-328 (2005).
7. Zs.Dombradi, Z.Elekes, R.Kanungo, H.Baba, Zs.Fulop, J.Gibelin, A.Horvath, E.Ideguchi, Y.Ichikawa, N.Iwasa, H.Iwasaki, S.Kanno, S.Kawai, Y.Kondo, T.Motobayashi, M.Notani, T.Ohnishi, A.Ozawa, H.Sakurai, S.Shimoura, E.Takeshita, S.Takeuchi, I.Tanihata, Y.Togano, C.Wu, Y.Yamaguchi, Y.Yanagisawa, A.Yoshida, K.Yoshida, Decoupling of valence neutrons from the core in  $^{17}\text{B}$ , *Phys. Let. B* **621** 81-88 (2005).

8. T. Hashimoto, H. Ishiyama, T. Ishikawa, T. Kawamura, K. Nakai, Y.X. Watanabe, H. Miyatake, M.H. Tanaka, Y. Fuchi, N. Yoshikawa, S.C. Jeong, I. Katayama, T. Nomura, T. Furukawa, S. Mitsuoka, K. Nishio, M. Matsuda, H. Ikezoe, T. Fukuda, S.K. Das, P.K. Saha, Y. Mizoi, T. Komatsubara, M. Yamaguchi, Y. Tagishi, Gated multiple-sampling and tracking proportional chamber new detector system for nuclear astrophysical study with radioactive nuclear beams, *Nucl. Instr. and Meth. A* **556** (1): pp.339-349, Jan 1 (2006).
9. E. Ideguchi, M. Niikura, C. Ishida, T. Fukuchi, H. Baba, N. Hokoïwa, H. Iwasaki, T. Koike, T. Komatsubara, T. Kubo, M. Kurokawa, S. Michimasa, K. Miyakawa, K. Morimoto, T. Ohnishi, S. Ota, A. Ozawa, S. Shimoura, T. Suda, M. Tarnaki, I. Tanihata, Y. Wakabayashi, K. Yoshida, B. Cederwal, Study of high-spin states in the Ca-48 region by using secondary fusion reactions, *Eur. Phys. J. A* **25**, pp.429-430, (2005).
10. S-Y Wang, T Komatsubara, Y-J Ma, K Furuno, Y-H Zhang, Y-Z Liu, T Hayakawa, J Mukai, Y Iwata, T Morikawa, G B Hagemann, G Sletten, J Nyberg, D Jerrestam, H J Jensen, J Espino, J Gascon, N Gjorup, B Cederwall, P O Tjom, Band Structure in  $^{123}\text{I}$ , *J. Phys. G: Nucl. Phys.* **32** pp.283-294, (2006).
11. T.Nagatomo, A. Ozawa, *et al*, Magnetic moment of extremely proton-rich nucleus  $^{23}\text{Al}$ , *J. Phys.: Conf. Ser.* 20 pp.173-174 (2005).

*ATOMIC AND SOLID STATE PHYSICS, AND CLUSTER SCIENCE*

12. Olga V. Boltalina, Alexey V. Streletskii, Ilya N. Ioffe, Preben Hvelplund, Bo Liu, Steen Broendsted Nielsen, and Shigeo Tomita, "Formation of long-lived fluorofullerene trianions in collisions with Na", *J. Chem. Phys.* **122**, 021102(1-3), (2005).
13. B. Concina, S. Tomita, J.U. Andersen, and P. Hvelplund, "Delayed ionization of  $\text{C}_{70}$ ", *Eur. Phys. J.* **34**, pp.191-194 (2005).
14. H. Kudo, Iwazaki, Wakamatsu, S. Tomita, "Resonant Coherent Excitation of  $\text{C}^{5+}$  in Si Observed with Backward Electron Spectroscopy", *Nucl. Instr. and Meth. B* **229**, 227-231 (2005).
15. S. Tomita, J.U. Andersen, E. Bonderup, P. Hvelplund, B. Liu, S. Broen dsted Nielsen, U.V. Pedersen, J. Rangama, K. Hansen, O. Echt, "Dynamic Jahn-Teller Effects in Isolated C-60 studied by Near-Infrared Spectroscopy in a Storage Ring", *Phys. Rev. Lett.* **94**, 053002 (2005).
16. B. Manil, L. Maunoury, J. Jensen, H. Cederquist, H.T. Schmidt, H. Zet tergren, P. Hvelplund, S. Tomita, B.A. Huber, "Fragmentation of charged fullerene dimers: Kinetic energy release", *Nucl. Instr. and Meth. B* **235**, 419-424 (2005).
17. L. Maunoury, B. Manil, J. Rangama, H. Lebius, B.A. Huber, J.Y. Pacque t, R. Leroy, U.V. Pedersen, P. Hvelplund, J. Jensen, S. Tomita, H. Ze ttergren H.T. Schmidt, H. Cederquist, F.

- Gustavo, "Ion beams of carbon clusters and multiply charged fullerenes produced with electron cyclotron resonance ion sources", *Rev. Sci. Instr.* **76**, 053304(1-8) (2005).
18. T. Kaneko, H. Kudo, S. Tomita, and R. Uchiyama, "Secondary electron emission from graphite induced by MeV/atom carbon cluster impacts", *J. Phys. Soc. Jpn.*, **75** 034717 (2006).
  19. Masashige Onoda, Shintaro Miyasaka, Tomohiro Mutoh and Katsuhiro Nichogi, Li local environments and the dynamics in the  $\text{Li}_{1+x}\text{V}_3\text{O}_8$  insertion electrode, *J. Phys.: Condens. Matter*, **17(26)**, 4057-4071 (2005).
  20. Masashige Onoda and Junichi Hasegawa, The spin-singlet states in the double trellis-layer bronzes  $\text{Na}_{0.56}\text{V}_2\text{O}_5$  with a uniform valence and  $\text{Sr}_{0.5}\text{V}_2\text{O}_5$  with a valence order, *J. Phys.: Condens. Matter*, **18(7)**, 2109-2123 (2006).
  21. Masashige Onoda and Mitsuko Onoda, Multifunctional composite crystal  $\text{Cu}_x\text{V}_4\text{O}_{11}$  ( $x \approx 2.2$ ), *Phys. Rev. B* **73**, 104108 (2006).
  22. Masashige Onoda, The science of vanadium oxide systems, *CERAMICS JAPAN* **41(3)**, 167-172 (2006)
  23. N. Yagi, A. Ueki, H. Mizubayashi and H. Tanimoto, "Anelasticity in FCC Nanocrystalline Metals", *Journal of Metastable and Nanocrystalline Materials*, 24-25, 503-506, (2005).
  24. H. Tanimoto, S. Sakai and H. Mizubayashi, "Giant Irradiation Effects in FCC Nanocrystalline Metals", *Journal of Metastable and Nanocrystalline Materials*, 24-25, 597-600, (2005).

#### *ION BEAM ANALYSIS AND APPLICATION*

25. Yasuo Nagashima, Riki Seki, Takeshi Matsuhiro, Tsutomu Takahashi, Kimikazu Sasa, Toshihide Usui, Keisuke Sueki,  $^{36}\text{Cl}$  Measurements in Japan, "Reassessment of the Atomic Bomb Radiation Dosimetry for Hiroshima and Nagasaki-Dosimetry System 2002", Report of the Joint US-Japan Working Group, Chapter 8, Part F, pp.555-560, The Radiation Effects Research Foundation, (2005).
26. Kimikazu Sasa, Yasuo Nagashima, Tsutomu Takahashi, Riki Seki, Yuki Tosaki, Keisuke Sueki, Kotaro Bessho, Hiroshi Matsumura, Taichi Miura, Jiang Shan and Ming He, Status and future plans of the Tsukuba AMS system, 1st East Asian Symposium on Accelerator Mass Spectrometry 26-27, January 2006, University of Tsukuba, Proceedings of the 1st East Asian Symposium on Accelerator Mass Spectrometry, UTTAC-74 (2006) 69-80.
27. Ming He, Shan Jiang, Y. Nagashima, Yaoyun Yang, T. Takahashi, Kexin Liu, K. Sasa, Kejun Dong, Shayong Wu, T. Matsuhiro, H. Tosaki, Xiaotang Ren, R. Seki, K. Sueki, Measurement of the cross-section of  $^{14}\text{N}(^{16}\text{O},\alpha)^{26}\text{Al}$  with AMS, *Nucl. Instr. and Meth. B*, **240** 612-616 (2005).

28. K. Awazu, M. Fujimaki, Y. Ohki, T. Komatsubara, Photonic crystals of titanium dioxide fabricated by swift heavy ions, *Rad. Meas.* **40** (2-6): pp.722-729 Sp. Iss. SI, NOV (2005).
29. M. Kurosawa, K. Miyakawa, T. Komatsubara, K. Sato, K. Sasa, S. Ishii, Y. Yamato, Y. Kobayashi, R. Anma, Hydrogen analysis of melt inclusions in chromian-diopside megacrysts from basaltic and basaltic andesite dykes intruded in a collision zone of the Izu-Bonin arc, *Gekkan Chikyu*, Vol.27, No.7, pp.519-524, (2005).
30. T. Komatsubara, K. Sasa, S. Ishii, Y. Yamato, K. Miyakawa, K. Satou, M. Kurosawa, Hydrogen analysis for geoscience by using nuclear microbeam, *Proc. of The 5th Italy-Japan Symposium, Recent Achievements and Perspectives in Nuclear Physics*, pp.429-437, (2005).
31. T. Komatsubara, K. Sasa, H. Ohshima, H. Kimura, Y. Tajima, T. Takahashi, S. Ishii, Y. Yamato, M. Kurosawa, K. Furuno, Hydrogen Content in Granite, "Reassessment of the Atomic Bomb Radiation Dosimetry for Hiroshima and Nagasaki-Dosimetry System 2002", Report of the Joint US-Japan Working Group, Chapter 10, Part E, pp.750-754, Radiation Effects Research Foundation, (2005).

## 7.2 International conferences

1. A. Ozawa, (**Invited Talk**), Nuclear matter radii determined by interaction cross sections, Workshop on Physics with Ultra Slow Antiproton Beams, 2005, 3/14-16, Wako, Japan.
2. A. Ozawa, (**Invited Talk**), Recent experiments of interaction and reaction cross sections and the related results, Hawaii 2005 second joint meeting of the nuclear physics division of the APS and JPS, 2005, 9/18-22, Maui, Hawaii, USA.
3. A. Ozawa, Interaction cross section / mass measurement, Workshop on nuclear physics collaboration between Germany and Japan, 2005, 12/16-17, RIKEN, Wako, Japan.
4. Yasuo Nagashima, Kimikazu Sasa, Riki Seki, Tsutomu Takahashi, Takeshi Matsuihiro, Keisuke Sueki, Yuki Tosaki, A  $^{129}\text{I}$ -AMS by a  $^{97}\text{Mo}^{16}\text{O}$  molecular pilot beam method, The 10th International Conference on Accelerator Mass Spectrometry (2005), Berkeley, UCLA.
5. Riki Seki, Takeshi Matsuihiro, Yasuo Nagashima, Tsutomu Takahashi, Kimikazu Sasa, Keisuke Sueki, Yuki Tosaki, Kotaro Bessho, Hiroshi Matsumura, Taichi Miura, Isotopic ratios of  $^{36}\text{Cl}/\text{Cl}$  in Japanese surface soil, The 10th International Conference on Accelerator Mass Spectrometry, (2005), Berkeley, UCLA.
6. Kotaro Bessho, Hiroshi Matsumura, Taichi Miura, Kazuyoshi Masumoto, Qingbin Wang, Hiroyuki Hagura, Yasuo Nagashima, Riki Seki, Tsutomu Takahashi, Kimikazu Sasa, Keisuke Sueki, Takeshi Matsuihiro, Yuki Tosaki, Estimation of thermal neutron fluences in various accelerator facilities by using  $^{36}\text{Cl}$  AMS, The 10th International Conference on Accelerator Mass Spectrometry, (2005), Berkeley, UCLA.

7. Yuki Tosaki, Norio Tase, Yasuo Nagashima, Riki Seki, Tsutomu Takahashi, Kimikazu Sasa, Keisuke Sueki, Takeshi Matsuhira, Taichi Miura, Kotaro Bessho, Hiroshi Matsumura, Ming He, Gudrun Massmann, Application of  $^{36}\text{Cl}$  as a dating tool for modern groundwater, The 10th International Conference on Accelerator Mass Spectrometry (2005), Berkeley, UCLA.
8. Kimikazu Sasa, Yasuo Nagashima, Tsutomu Takahashi, Riki Seki, Yuki Tosaki, Keisuke Sueki, Taichi Miura, Kotaro Bessho, Hiroshi Matsumura, Ming He,  $^{26}\text{Al}$  and  $^{36}\text{Cl}$  AMS system at the University of Tsukuba: A progress report, The 10th International Conference on Accelerator Mass Spectrometry (2005), Berkeley, UCLA.
9. T. Nagatomo, "Magnetic Moment of Extremely Proton-rich Nucleus  $^{23}\text{Al}$ ", 2nd Joint Meeting of DNP-APS and JPS, Sep. 18-22, 2005, Ritz-Carlton, Kapalua Maui, Hawaii, USA.

## 8. THESES

### *M. Sc. Theses*

Yuji Ito	Study of $^{118}\text{Sn}(d,p)$ reaction below Coulomb barrier
Kentaro Miki	Measurement of asymmetric emission of direct photon in RICH heavy-ion experiment
Takuma Yasuno	Development of tilted electrode gas ionization chamber for a measurement of an energy loss of an unstable nucleus

## 9. SEMINARS

<u>Date</u>	<u>Title and Speaker</u>
2005	
Apr. 20	Development of the SPring-8 linac control system for stable continuous injection <i>T. Masuda (JASRI)</i>
Jun 1	Studies of resonance states in proton-rich nuclei with low-energy RI beams <i>A. Saito (CNS, The Univ. of Tokyo)</i>
2006	
Jan. 18	Study of $^{118}\text{Sn}(d,p)$ reaction below Coulomb barrier <i>Y. Ito (Univ. of Tsukuba)</i>
Jan. 25	Measurement of asymmetric emission of direct photon in RICH heavy-ion experiment <i>K. Miki (Univ. of Tsukuba)</i>
	Development of tilted electrode gas ionization chamber for a discrimination of the secondary ion beam <i>T. Yasuno (Univ. of Tsukuba)</i>
Feb. 1	Simulation of performance for a Multigap Resistive Plate Chamber <i>M. Narisawa (Univ. of Tsukuba)</i>
Feb. 9	Nucleon-nucleon momentum correlation function in light nuclei induced reactions <i>Yu-Gang Ma (Shanghai Institute of Applied Physics)</i>
Mar. 17	Dosimetry study for the residents near Semipalatinsk Nuclear Test Site and proposal of $^{129}\text{I}$ measurement <i>S. Endo (Hiroshima University)</i>

## 10. SYMPOSIA

### **Mass Measurements in the Isochronous Rare-RI Ring and Nucleosynthesis**

*29 September, 2005*

*Room C305, Tandem Accelerator Complex,*

*Research Facility Center for Science and Technology, University of Tsukuba*

1. Opening remark : *A.Ozawa (Univ. of Tsukuba)*
2. Physics opportunities with the RI Beam Factory at RIKEN : *H.Sakurai (RIKEN)*
3. Mass measurements in the isochronous rare-RI ring : *A.Ozawa (Univ. of Tsukuba)*
4. Isochronous ring and its computer simulation : *I.Arai (Univ. of Tsukuba)*
5. Injection line to the isochronous rare-RI ring : *H.Ota (Univ. of Tsukuba)*
6. Discussion of injection scheme and kicker magnet design for isochronous ring : *Y.Yamaguchi (RIKEN)*
7. Extraction of fractions of the resonant component from analyzing powers in  ${}^6\text{Li}(d,\alpha){}^4\text{He}$  and  ${}^6\text{Li}(d,p){}^7\text{Li}$  reactions at very low incident energies : *M.Yamaguchi (RIKEN)*
8. Atomic mass formula and r-process nucleosynthesis : *H.Koura (JAERI)*
9. Present status of mass measurements of unstable nuclei by a multi-reflection time-of-flight mass spectrometer : *Y.Ishida (RIKEN)*
10. Mass measurements with a CIME cyclotron at GANIL : *T.Ootsubo (Univ. of Niiigata)*
11. Studies of supernovae nucleosynthesis at UTTAC : *T.Hayakawa (JAERI)*
12. Studies of resonance states in proton-rich nuclei using low-energy RI beams : *A.Saito (CNS, The Univ. of Tokyo)*
13. Particle discrimination using pulse shape analysis in Si detector : *M.Kurokawa (RIKEN)*
14. Closing remark : *I.Arai (Univ. of Tsukuba)*

### **1st East Asian Symposium on Accelerator Mass Spectrometry, EAAMS-1**

*26-27 January, 2006*

*Room No. B0110, Laboratory of Advanced Research B*

*University of Tsukuba*

1. Opening 1 : *Sadao Aoki (Univ. of Tsukuba)*
2. Opening 2 : *Mineo Imamura (National Museum of Japanese History)*

3. Introduction of a compact AMS system for earth science in KIGAM : *Wan Hong (Korea Institute of Geoscience and Mineral Resources (KIGAM))*
4. Status and future plans of NIES-TERRA : *Minoru Yoneda (NIES)*
5. AMS facility in Xian and its application to paleoenvironment and paleoclimate study : *Weijian Zhou (Chinese Academy of Sciences)*
6. Current status of the NSF-Arizona AMS Laboratory : *Kyeong J. Kim (The University of Arizona)*
7. Current status of the compact  $^{14}\text{C}$  AMS system at Paleo Labo Co., Ltd. : *Etsuko Niu (Paleo Labo Co., Ltd.)*
8. Particle Identification Techniques in AMS Measurement : *Jiang Shan (China Institute of Atomic Energy)*
9. Dating Upper Paleolithic sites in Korea : *Jong Chan Kim (Seoul National University)*
10. The project of the "Yayoi Chronology" and user-facility relationships CSR-program collaboration "The Origin of the Farming in the Yayoi Period and East Asia" : *Mineo Imamura (National Museum of Japanese History)*
11. PKUAMS and the Project of Xia-Shang-Zhou Chro Chronology: Progress and Some Results : *Guo Zhiyu (Peking University)*
12. High precision  $^{14}\text{C}$  measurements with AMS and applications in archeology and geology at Nagoya University : *Toshio Nakamura (Nagoya University)*
13. An ideal AMS facility - a view from AMS user : *Kunihiko Nishiizumi (University of California, Berkeley)*
14. Status and future plans of the Tsukuba AMS system : *Kimikazu Sasa (Univ. of Tsukuba)*
15.  $^{99}\text{Tc}$  measurement with AMS at CIAE : *He Ming (China Institute of Atomic Energy)*
16. Status of JAEA Mutsu Tandetron AMS Facilities : *Hikaru Amano (Japan Atomic Energy Agency)*
17. Discussion & Closing of EAAMS-1 : *Mineo Imamura and Koichi Kobayashi*

### **The 8th Japanese Symposium on Accelerator Mass Spectrometry, JAMS-8**

*27-28 January, 2006*

*Room No. B0110, Laboratory of Advanced Research B*

*University of Tsukuba*

1. Current status of AMS at MALT, The University of Tokyo, in 2005 : *K.Kato (The Univ. of Tokyo)*
2. High-precision radiocarbon measurements of tree-ring-dated wood from Japan:685BC-193BC : *H.Ozaki (National Museum of Japanese History)*
3. Study of archaeological site formation process restoration using AMS radiocarbon dating : *S.Muramoto (Graduate University for Advance Studies)*

4. Radiocarbon dating of lipids in Lake Baikal surface sediments : *T.Watanabe (Nagoya Univ.)*
5. Concentrations of  $^7\text{Be}$ ,  $^{10}\text{Be}$  in the atmosphere at Tokyo and Hachijo-Island during the period 2002 to 2003 : *T.Yamagata (Nihon Univ)*
6. Distribution of  $^7\text{Be}$  and  $^{10}\text{Be}$  in Antarctic Ocean : *E.Taguma (Nihon Univ.)*
7. The  $^{10}\text{Be}$  flux record in marine sediment in the Western North Pacific : *T.Yoshida (Nihon Univ.)*
8. Radiocarbon dating of carbonaceous samples excavated at the Muramatsu-Shirane site, Ibaragi Prefecture, Japan : *H.Oda (Nagoya Univ.)*
9. Calendar age of the Early Yayoi Period in the South-west Kanto: Estimates from the remains at the Naka-yashiki site, Ooi-machi, Kanagawa : *Y.Sasaki (Paleo Labo Co., Ltd.)*
10. Calendar age of the late Middle to the early Late Jomon pottery in Fukushima prefecture : *S.Itoh (Paleo Labo Co., Ltd.)*
11. Carbon and nitrogen isotopic fractionation in bone collagen during chemical treatment : *M.Minami (Nagoya Univ.)*
12. Dating of groundwater : *N.Tase (Univ. of Tsukuba)*
13. Application of bomb-produced  $^{36}\text{Cl}$  in groundwater dating : *Y.Tosaki (Univ. of Tsukuba)*
14. AMS of  $^{36}\text{Cl}$  induced in the concrete of accelerator facilities -Thermal neutron fluences in the concrete of various accelerator facilities- : *K.Bessho (KEK)*
15. Application of microscale AMS  $^{14}\text{C}$  analyses to micro organic pollutants in the atmosphere: Fossil vs. biomass carbon contributions to atmospheric PAHs associated with PM10 and PM1.1 aerosols from residential area of suburban Tokyo : *H.Kumada (Tokyo Medicine Collage)*
16. The application of radiocarbon dating to archaeological excavation : *T.Omori (Nagoya Univ.)*
17. Sediment accumulation pattern of the incised-valley fills induced from the high-density AMS radiocarbon dates: latest Pleistocene to Holocene example from the Paleo Oku-Tokyo Bay, central Japan : *T.Nakanishi (National Institute of Advanced Industrial Science and Technology)*
18. Sedimentary facies and  $^{14}\text{C}$  dates of the latest Pleistocene to Holocene incised-valley fills from Yoroigata, Echigo Plain, central Japan : *S.Tanabe (National Institute of Advanced Industrial Science and Technology)*
19. Radiocarbon dating of the Fugusawa site in Aomori Prefecture 2005 : *D.Kunikida (The Univ. of Tokyo)*
20. Information on fiber-tempered pottery : *A.Minato (Nihon Univ.)*
21. Study on transportation of particulate organic matter in river water from Hokkaido Island during snow-melting season by C-14 : *J.Alam (Hokkaido Univ.)*
22. The establishment of the method for  $^{14}\text{C}$  distribution of dissolved organic carbon in sea water : *S.Tani (Nagoya Univ.)*
23. Development of analysis system of dissolved organic radiocarbon : *T.Tanaka (JAEA)*
24. Effect of paraloid<sup>TM</sup>, adhesive cement for fossils, to  $^{14}\text{C}$  dating for fossil : *H.Uno (NIES)*
25. Geochemical study on human bones excavated from the Yuigahama site, Kamakura, Japan : *M.Minami (Nagoya Univ.)*
26. Seasonal variation of radiocarbon in urban atmospheric aerosol : *K.Takahashi (NIES)*
27. A study on pretreatment method for iodine isotopic ratio determination in seaweed : *J.Kuwabara (JAEA)*

## 11. LIST OF PERSONNEL

### Tandem Accelerator Complex

Y. Nagashima	Director, Professor
T. Komatsubara	Assistant Professor
K. Sasa	Assistant Professor
S. Ishii	Mechanical Engineer
H. Kimura	Computer Engineer
H. Oshima	Electric Engineer
Y. Tajima	Mechanical Engineer
T. Takahashi	Electric Engineer
Y. Yamato	Electric Engineer
H. Ota	Research Fellow
R. Seki	Former Professor
M. Moro	Administrative Staff

### Research Members

#### *Inst. of Physics*

T. Aoki	Y. Aoki	I. Arai	S. Esumi	S. Katoh
T. Komatsubara	Y. Miake	T. Nagatomo	M. Onoda	H. Ota
A. Ozawa	K. Sasa	M. Yamaguchi		

#### *Inst. of Applied Physics*

E. Kita	H. Kudo	N. Tomita	A. Uedono	H. Yanagihara
---------	---------	-----------	-----------	---------------

#### *Inst. of Material Science*

T. Koyano	H. Mizubayashi	K. Takita	H. Tanimoto
-----------	----------------	-----------	-------------

#### *Inst. of Geoscience*

M. Kurosawa	N. Tase
-------------	---------

#### *Inst. of Chemistry*

K. Sueki

#### *Inst. of Basic Medical Science*

Y. Nagashima

## Scientific Guests and Fellows

K. Awazu	National Lab. Advanced Industrial Science and Technology
T. Ikeda	Waseda Univ.
T. Ohura	Tokyo Metropolitan Univ.
M. Yamazaki	Tokyo Metropolitan Univ.
T. Hayakawa	JAERI
M. Kurokawa	RIKEN
T. Fukuchi	RIKEN
H. Baba	RIKEN
S. Nishimura	RIKEN
Y. Tagishi	RIKEN
A. Saito	CNS, The Univ. of Tokyo
S. Kubono	CNS, The Univ. of Tokyo
H. Yamaguchi	CNS, The Univ. of Tokyo
He Jianjun	CNS, The Univ. of Tokyo
H. Fujikawa	CNS, The Univ. of Tokyo
A. Guilherme	CNS, The Univ. of Tokyo
Y. Wakabayashi	Kyushu Univ.
N. Okumura	Nagano College of Technology
K. Matsuta	Osaka Univ.
T. Nagatomo	Osaka Univ.
T. Mihara	Osaka Univ.
R. Matsumiya	Osaka Univ.
T. Sumikama	RIKEN
I. Sugai	KEK
Y. Takeda	KEK
M. Oyaizu	KEK
H. Kawakami	KEK
T. Miura	KEK
K. Bessho	KEK
H. Matsumura	KEK
K. Masumoto	KEK
H. Oguri	Tokyo Institute of Technology
J. Hasegawa	Tokyo Institute of Technology
J. Kaneko	Tokyo Institute of Technology

## Graduate Students

### *Doctoral Degree Programs of Pure and Applied Science*

Jo Ben Ho	S. Igarashi	M. Iijima	So Jong Wong	M. Konno
H. Masui	K. Miyakawa	Y. Nagata	M. Nakazumi	M. Narisawa
M. Oka	S. Sakai	J. Sawahata	M. Shimomura	H. Tokano

N. Yagi

### *Master's Degree Programs of Pure and Applied Science*

H. Arai	T. Ebisawa	Y. Fujii	K. Fujiwara	D. Fukuhara
M. Furutani	M. Hasegawa	Y. Ikeda	T. Ishikawa	T. Isobe
Y. Ito	H. Kasai	Y. Kikuchi	A. Kondo	K. Miki
H. Mishiba	K. Nakamoto	T. Niida	T. Nishimura	A. Rikukawa
A. Sasaki	T. Sato	K. Shibata	T. Sugaya	T. Takahashi
K. Takao	R. Tanabe	Y. Tomita	Y. Toyota	R. Uchiyama
N. Umada	H. Wakamatsu	K. Yamagishi	T. Yasuno	S. Yoda

### *Master's Degree Programs of Education*

K. Yamaguchi

### *Master's Degree Programs of Environmental Science*

Y. Tosaki

## Undergraduates

M. Furukawa	J. Hagiwara	Y. Hashizume	K. Iwamura	S. Kanda
T. Kawamata	M. Minakawa	H. Nagami	Y. Odajima	H. Okaguchi
R. Sawai	D. Yoshioka			